Ministry of Education and Science of Ukraine
Vasyl Stefanyk Precarpathian National University

ISSN 2311-0155

Journal of Vasyl Stefanyk Precarpathian National University

SCIENTIFIC EDITION

Series of Natural and Mathematical Sciences

PHYSICS

Vol. 3, No. 1, 2016

Ivano-Frankivsk
2016

Journal of Vasyl Stefanyk Precarpathian National University

SCIENTIFIC EDITION Vol. 3, No. 1, 2016

Recommended for publication by Scientific Council of Vasyl Stefanyk Precarpathian National University
Certificate of State Registration KB No 20385-10185P

Korobeynikov Georgiy, *National University of Physical Education and Sport, Ukraine* (Physiology of Man and Zoons),
Kosarevych Rostyslav, *Karpenko Physical-Mechanical Institute of the National Academy of Sciences of Ukraine, Ukraine* (Automated Systems, Advanced Information Technology),
Kosiewicz Jerzy, *Józef Piłsudski University of Physical Education in Warsaw, Poland* (Philosophy),
Kotyk Tetyana, *Vasyl Stefanyk Precarpathian National University, Ukraine* (Theory and Methodology of teaching),
Kozak Ihor, *Vasyl Stefanyk Precarpathian National University, Ukraine; The John Paul II Catholic University of Lublin, Poland* (Ecology, Landscape Ecology and Modeling),
Kozak Stefan, *Warsaw University, Poland* (Philological Sciences),
Kozlenko Mykola, *Vasyl Stefanyk Precarpathian National University, Ukraine* (Computer Systems and Components),
Krul Petro, *Vasyl Stefanyk Precarpathian National University, Ukraine* (Theory and History of Culture),
Kugutiak Mykola, *Vasyl Stefanyk Precarpathian National University, Ukraine* (Ethnology),
Kulyk Oleksii, *Ukrainian National Academy of Sciences, Ukraine* (Probability Theory, Mathematical Statistics),
Kurta Sergiy, *Vasyl Stefanyk Precarpathian National University, Ukraine* (Chemical Technology),
Kyiak Sviatoslav, *Vasyl Stefanyk Precarpathian National University, Ukraine* (Philosophy of Science, Philosophy of Education, Religious studies, Ukrainian studies),
Lazarovych Mykola, *Vasyl Stefanyk Precarpathian National University, Ukraine* (Elements and Devices of Computer Facilities and Control Systems),
Łebkowski Piotr, *«AGH» University of Science and Technology, Poland* (Automation and Robotics, Operational Researches, Information Technologies),
Lopushansky Oleh, *Rzeszow University, Poland* (Mathematical Analysis),
Lytovchenko Volodymyr, *V. Lashkaryov Institute of Semiconductor Physics of NAS of Ukraine, Ukraine* (Physics of Semiconductors and Dielectrics),
Makarewicz Edwin, *University of Technology and Life Sciences, Poland* (Chemical Technology),
Makcymenko Sergii, *Institute of Psychology of G.S. Kostyuka NAPN of Ukraine, Ukraine* (Philological Sciences),
Malashkevich Georgii, *National Academy of Sciences of Belarus, Belarus* (Optics, Laser Physics),
Marchuk Vasyl, *Vasyl Stefanyk Precarpathian National University, Ukraine* (Political Science),
Mykhailenko Valerii, *Bukovyna State University of Finance and Economics, Ukraine* (German Language),
Myronyuk Ivan, *Vasyl Stefanyk Precarpathian National University, Ukraine* (Physics and Chemistry of Surfaces),
Novosyadly Stepan, *Vasyl Stefanyk Precarpathian National University, Ukraine* (Solid State Electronics),
Nykyforchyn Oleh, *Vasyl Stefanyk Precarpathian National University, Ukraine* (Geometry and Topology),
Nykyruy Lyubomyr, *Vasyl Stefanyk Precarpathian National University, Ukraine (*Physics of Semiconductors and Dielectrics*),*
Ostafiychuk Bohdan, *Vasyl Stefanyk Precarpathian National University, Ukraine* (Solid State Physics, Physics and Chemistry of Surface),
Ostapovych Oleh, *Vasyl Stefanyk Precarpathian National University, Ukraine* (German Language),
Osypchuk Mykhailo, *Vasyl Stefanyk Precarpathian National University, Ukraine* (Probability Theory, Mathematical Statistics),
Panchuk May, *I.F. Kuras Institute of Political and Ethnic Studies at NAS of Ukraine, Ukraine* (Ethnology),
Parpan Vasyl, *Vasyl Stefanyk Precarpathian National University, Ukraine* (Forestry, Ecology),
Petryshyn Lubomyr, *Vasyl Stefanyk Precarpathian National University, Ukraine; «AGH» University of Science and Technology, Poland* (Computer Systems and Components),
Plichko Anatolij, *Cracow University of Technology, Poland* (Mathematical Analysis),
Pylypenko Andrii, *Ukrainian National Academy of Sciences, Ukraine* (Probability Theory, Mathematical Statistics),
Pylypiv Volodymyr, *Vasyl Stefanyk Precarpathian National University, Ukraine* (Solid State Physics, Physics and Chemistry of Surface),
Reient Oleksandr, *Vasyl Stefanyk Precarpathian National University, Ukraine* (History of Ukraine),
Rudenko Svitlana, *Yuriy Fedkovych Chernivtsi National University, Ukraine* (Ecology),
Rudnytzkyi Leonid, *La Salle University, USA* (Philological Sciences),
Salii Yaroslav, *Vasyl Stefanyk Precarpathian National University, Ukraine* (Physics and Chemistry of Surface),
Salyha Taras, *Ivan Franko Lviv National University, Ukraine* (Theory of Literature),

---

Editorial address:
Vasyl Stefanyk Precarpathian National University,
57, Shevchenko Str.,
76018, Ivano-Frankivsk, Ukraine
Tel.: +380 (342) 59-60-50
E-mail: jpnu@pu.if.ua
http://jpnu.pu.if.ua/

ISSN 2311-0155

Journal of Vasyl Stefanyk
Precarpathian National University

CONTENTS

Journal of Vasyl Stefanyk Precarpathian National University
http://jpnu.pu.if.ua
Vol. 3, No. 1 (2016), 9-14

UDC 546.81
PACS numbers: 73.50 Lw; 73/50Pz
doi: 10.15330/jpnu.3.1.9-14

THE THERMOELECTRIC SOLAR PANELS

R. AHISKA, L.I. NYKYRUY, G. OMER, G.D. MATEIK

Abstract. In this study, load characteristics of thermoelectric and photovoltaic solar panels are investigated and compared with each other with experiments. Thermoelectric solar panels converts the heat generated by sun directly to electricity; while, photovoltaic solar pales converts photonic energy from sun to electricity. In both types, maximum power can be obtained when the load resistance is equal to internal resistance. According to experimental results, power generated from unit surface with thermoelectric panel is 30 times greater than the power generated by photovoltaic panel. From a panel surface of 1 m^2, thermoelectric solar panel has generated 4 kW electric power, while from the same surface, photovoltaic panel has generated 132 W only.

Keywords: thermoelectric, photovoltaics, solar panel, renewable energy.

1. INTRODUCTION

Today, fossil fuels such as coal and oil are used as sources of energy to obtain electrical power. These fossil fuels are limited sources and continuously omit greenhouse gases to environment. Efforts towards research use new and renewable energy sources increase due to greenhouse gas emission and increase in global warming. The world's population increases constantly and need for energy increases accordingly. In future, mankind needs to make maximum use of renewable energy resources such as solar, wind, biomass, geothermal and hydrogen to minimize the threats posed by energy sources and meet the energy requirement [1]. Solar energy, which is a renewable energy source, is infinite, clean and renewable. Solar energy emits as rays and heat. Photovoltaic panels (PV) and thermoelectric panels (TE) have been widely used especially in areas far from electric network due to their advantages such as converting the sun rays or thermal energy emitted from the sun directly into electrical energy. However, PV panels are more widely used compared to TE panels. Studies on thermoelectric panels show that TE panels could compete with PV panels and would even replace them. The cost per kW of the electrical energy obtained from PV and TE systems are higher compared to sources such as water, coal or oil. This unit cost is usually constituted by PV and TE panels and the battery group used in these systems. Recently, PV and TE systems directly connected to the network and reduced battery use have been developed in order to reduce the unit cost and make maximum use of solar energy. Today, PV systems work with approximately 20% efficiency. Thanks to the newly developed optical concentrators, this level of efficiency has been increased up to about 30% [2, 3]. TE panels have no moving parts, their structure is simple, they require no maintenance, they are long lasting, they allow

temperature control, directly convert the electrical energy and work quietly, reliably and decidedly. Along with these advantages, the biggest drawback is that the efficiency drops to (5 -10) % when the temperature difference between thermoelectric modules used in panels is 100°C. However, even when the temperature difference increases slightly, the efficiency of TE panels can go up to (30-40) % [4]. Commercially, the unit cost of the electric power produced by a PV panel is 1.5 W/€, while it is 1.5 W/$ for a TE panel. Therefore, TE panels are more advantageous compared to PV panels in terms of electric energy production. They are also more advantageous given the space they take [5].

2. THE BASIC STRUCTURES OF PV AND TE PANELS

2.1. PVS AND THEIR CHARACTERISTICS

PV technologies, which are very common today, are semiconductor devices consisting of single crystal and polycrystalline silicon modules. PV cells consist of two n- and p-type semiconductor materials. Photons hit PV cells due to radiation effect and cause electrons to move and pass through load. The work efficiency of PV cells increases as the radiation intensity increases. PV cells work like a current source [6]. A PV cell can be modeled as in Figure 1a. PV cell model is made up of the current source, diode, parallel resistance Rp and serial resistance Rs. The PV cell completes its circuit through the diode when it is open circuit and through the external load when it is shorted. Although the value of parallel resistor is very high, the value of serial resistor is very low. The maximum power (MPP) is obtained when the resistance of the load connected is equal to the internal resistance of the PV cell. In order to capture the maximum power from the PV cell, solar inverter's maximum power point tracker (MPPT) control loops are used. As shown in Figure 1b, the PV cell shows different behaviours depending on the size of the PV panel or the type of the load connected and intensity of sunlight. The PV cell's characteristic is described as voltage and current change when different loads are connected. The maximum voltage VOC is measured on its ends when the PV cell is in the sunlight with open ends. This voltage is the open circuit voltage. When two ends of the PV cell is shorted, the maximum current ISC passes through, and in this case, the voltage is zero. This current is called the short circuit current. Temperature and light intensity affects the output characteristics of the PV cell. The current is directly proportional to the intensity of the light. Voltage varies depending on the level of light emitted, but this variation is very small. MPP is the point where the highest power is transmitted from the system to the receivers. PVs work in a wide range of voltage and current. Therefore, the power output changes constantly [7].

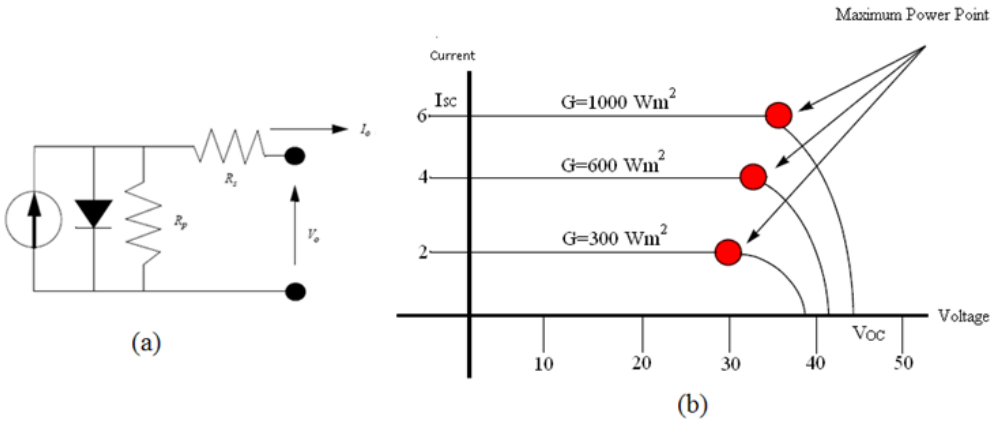

Fig. 1. (a) PV cells' electrical model, (b) V-I against illumination (36 cells set).

2.2. TEs and Their Characteristics

The basic structure of a thermoelectric module is made up of thermoelements. Thermoelements result from the combination of p- and n-type semiconductor and conductor. Thermoelements are connected electrically in series, and thermally in parallel. The modules operate with Seebeck effect. Seebeck effect was found by Thomas Seebeck in 1821. The electrical circuit model of the thermoelectric module is given in Fig. 2 (a). TE's electrical circuit model is similar to PV battery's electrical circuit model. The increase in the electric current causes an increase in the power spent in the internal resistance. If a temperature difference is created between the surfaces of the thermoelectric module and a load is connected to both ends, electrical current passes through the load and electric power is obtained [1].

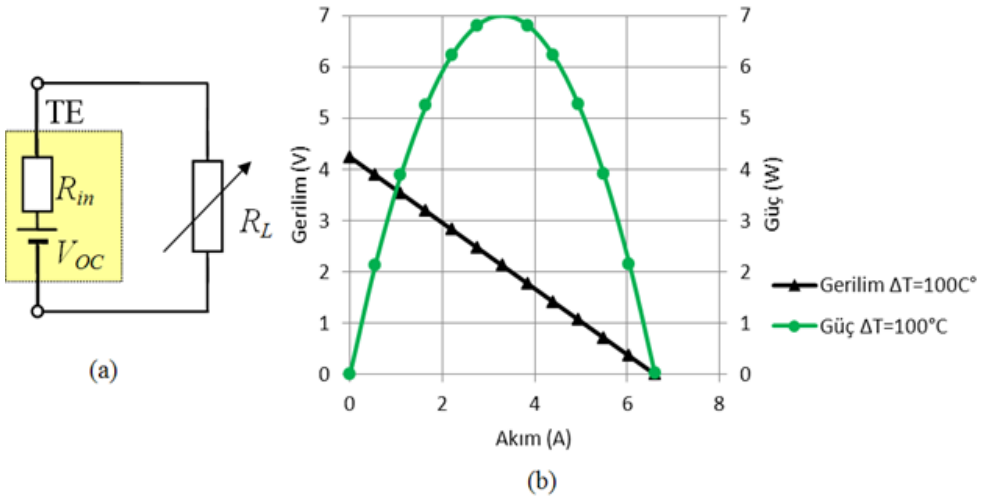

Fig. 2. (a) The electrical circuit model of the thermoelectric module, (b) TE V-I graph.

The open circuit voltage obtained from the thermoelectric module varies parabolically depending on the temperature difference between the surfaces ($\Delta T = T_H - T_C$). The maximum power is obtained from a TE when the resistance of the load connected is equal to the internal resistance of TE. The TE output characteristic is given in Fig. 2 (b). The power obtained changes when the temperature difference between the surfaces of TE is maintained at a constant value and the value of the load connected to the ends is changed. The maximum current is obtained when the load value is zero. The maximum voltage value is obtained when the load value is infinite. The maximum power is obtained when the resistance of the load connected is equal to the internal resistance of TE. If the temperature difference between the TE's surfaces is increased, the power value also increases parabolically [1].

3. Experimental Installation

3.1. Experimental PV Installation

The experimental PV installation as in Fig. 3 was carried out in Ankara on July 21st, 2014 at 12:00. The experimental installation involved solar panel, solar gauge, and electronic load.

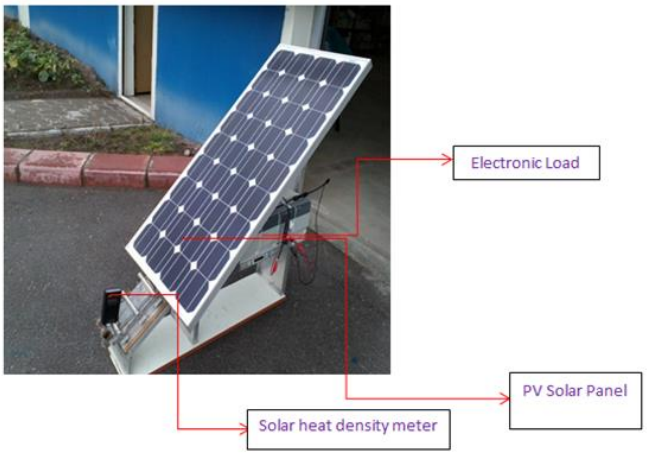

Fig. 3. PV system installation.

As the solar panel, a LCS Solar Strom AG type solar panel consisting of 40 PV cells and with the dimensions of 900x676x35 mm was used. The PV panel area was 0.61 m^2 and the maximum power was indicated to be 80 W on the label. Electronic load was used in order to obtain PV panel's characteristics. The intensity of the heat from the sun was measured with heat density solar meter, and the resistors were measured with the electronic load Mainframe device.

3.2. Experimental TE Installation

The experimental TE installation is given in Figure 4. This TE system was designed to be portable. It can be used anywhere. The TE system consists of four parts: TE panel, solar gauge, temperature gauge and electronic load. The temperatures were measured with CE 307 digital thermometer, the intensity of the heat from the sun was measured with heat density solar meter, and the resistors were measured with the electronic load Mainframe device.

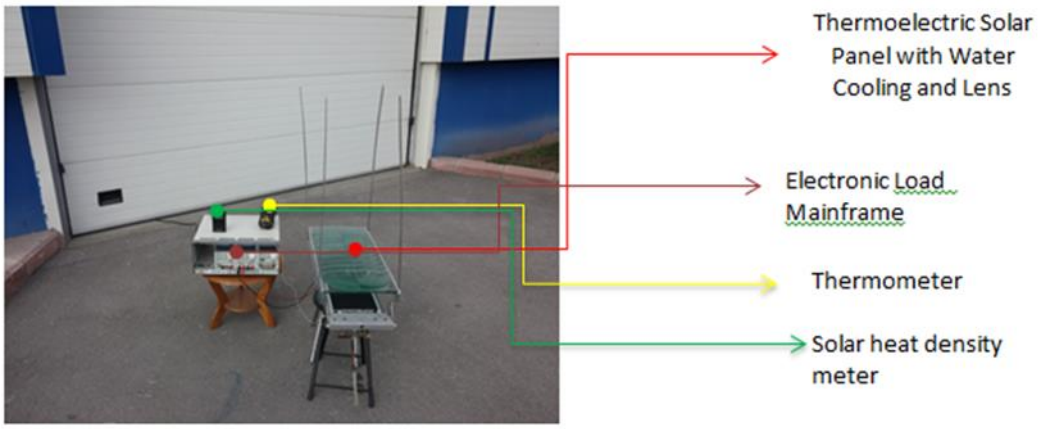

Fig. 4. The experimental portable TE installation.

For TE system, 10 thermoelectric modules 5x5x0.4 cm in size, which were custom produced by TES Ltd. company, were used and the surface area of the TE panel was 0.025 m^2. These were mounted on a flat surface using silicone gel between the module surface and mounted surface to increase the thermal transmittance. All modules were connected in series to increase output voltage. Since the electrical energy obtained from TEs depends on the temperature difference between the surfaces, two T-type point-tipped thermocouples were used to measure the temperature of the surfaces. Running water was used to cool the cold surface of TE and the water discharge was maintained at 30 ml/sec. The upper surface of the panel was painted black with a special paint to absorb the heat from the sun maximally

and a special lens was used to increase the temperature of the surface. The height of the lens on the panes was kept constant at 20 cm, which is the focal length of the lens.

4. Evaluation of Experiment Results

The data obtained in PV and TE system experiments are given in Table 1. The experiments were conducted for 30°C environmental temperature value. The density of the power from the sun was measured to be 2 kW/m². It was measured as $\Delta T = T_H - T_C = 140°C – 40°C = 100°C$ on the TE panel with lens. For PV panel, the maximum power value was approximately 80.55 W, when the load resistance was 10 Ω, the current value was 4.5 A and the voltage was 17.9 V. The amount of electrical power obtained from unit area was 132 W/m².

R_L,Ω	U_{TE},V	I_{TE},A	P_{TE},W	U_{PV},V	I_{PV},A	P_{PV},W
∞	45	0	0	22,1	0	0
50	45	0	0	21	0.8	16.8
25	30	2	60	20.2	1.1	22.22
20	27	3	81	20	1.97	39.4
15	25	4	100	19.6	2.7	52.92
10	20	3,5	70	17.9	4.5	80.55
5	15	3	45	10.4	4.4	45.76
0	0	10	0	0	5.1	0

Tab. 1. Experiment data of PV and TE systems.

For TE panel, the maximum power value was 100 W, when the load resistance was 15 Ω, the current value was 4 A and the voltage was 25 V. The amount of electrical power obtained from unit area was 4000 W/m².

5. Conclusion

The characteristic behaviors of TEs' and PV panels in energy production were investigated. TEs produce electrical power from the heat generated by the sun, while PV systems produce electrical power from sun rays. According to the results obtained, the amount of electric power produced from the unit surface of thermoelectric panel was about 30 times more compared to photovoltaic panel. The amount of electric power produced from one square-meter of thermoelectric panel surface was 4 kW, while it was only 132 W for a photovoltaic panel with the same surface area. Since the cost of electrical energy produced by PV panel is more than 1.5 – 2 times of TE panel on average, TE panels are more advantageous compared to PV panels in terms of electric energy production. They are also more advantageous given the space they take. But both technologies are environment-friendly and renewable.

Acknowledgment

This research is sponsored by NATO's Public Diplomacy Division in the framework of "Science for Peace" (NATO SPS G4536).

REFERENCES

[1] Ahıska R., Mamur H., Uliş M. Modeling and experimental study of thermoelectric module as generator. *J. Fac. Eng. Archit. Gaz*., **26** (4) (2011), 889–896.
[2] Sefa İ., Özdemir Ş. Experimental study of interleaved MPPT converter for PV system, Proc. "35th Annual Conference of IEEE on Industrial Electronics", Porto, Turkey, 3-5 Kasım 2009.
[3] Ahıska R., Dişlitaş S., Ömer G. A new method and computer-controlled system for measuring the time constant of real thermoelectric modules. *Energ. Convers. Manage*, **53** (1) (2012), 314–321.
[4] Ahıska R., Dişlitaş S. Microcontroller based thermoelectric generator application. *J. Fac. Eng. Archit. Gaz*., **19** (2) (2006), 135–141.
[5] Kajikawa T. Present status of research and development on thermoelectric power generation technology in Japan. *J. Thermoelectricity*, **45** (1) (2009), 18-29.
[6] Houssamo I., Locment F., Sechilariu M. Maximum power tracking for photovoltaic power system: Development and experimental comparison of two algorithms. *Renew. Energ*., **35** (10) (2010), 2381-2387.
[7] Chowdhury S.R., Saha H. Maximum power point tracking of partially shaded solar photovoltaic arrays. *Sol. Energ. Mat. Sol. C*., **94** (9) (2010), 1441-1447.

Address: R. Ahiska, Gazi University, 06500, Ankara, Turkey;
L.I. Nykyruy, Vasyl Stefanyk Precarpathian National University, 57, Shevchenko Str., Ivano-Frankivsk, 76018, Ukraine;
G. Omer, TES Ltd Co., 06500, Ankara, Turkey;
G.D. Mateik, Ivano-Frankivsk National Technical University of Oil and Gas, 15, Karpatska Str., Ivano-Frankivsk, 76000, Ukraine.
E-mail: ahiska@gazi.edu.tr; liubomyr.nykyrui@pu.if.ua.
Received: 18.01.2016; **revised:** 20.03.2016.

———————————

Ахіска Р., Никируй Л.І., Омер Г., Матеїк Г.Д. Термоелектричні сонячні панелі. *Журнал Прикарпатського університету імені Василя Стефаника*, **3** (1) (2016), 9–14.

У статті виконано порівняння експериментальних робочих характеристик термоелектричних та фотоелектричних сонячних панелей. Термоелектричні сонячні панелі перетворюють тепло, яке виділяється сонцем безпосередньо в електрику; у той час як сонячні фотоелектричні панелі перетворюють енергію фотонів від сонця в електрику. В обох типах може бути отримана максимальна потужність, коли опір навантаження рівні внутрішньому опору. Відповідно до результатів експериментальних досліджень, потужність, яка генерується із одиниці поверхні термоелектричної панелі у 30 разів вища, ніж потужність, яка генерується фотоелектричною панеллю. З поверхні термоелектричної сонячної панелі площею 1м² згенеровано 4 кВт електроенергії, у той час як з такої ж самої площі поверхні фотоелектричні панелі згенеровано лише 132 Вт.

Ключові слова: термоелектрика, фотоелектрика, сонячні панелі, відновлювальна енергетика.

Journal of Vasyl Stefanyk Precarpathian National University
http://jpnu.pu.if.ua
Vol. 3, No. 1 (2016), 15-22

UDC 546.48'24:544.022.384.2
PACS numbers: 71.15 Mb
doi: 10.15330/jpnu.3.1.15-22

THERMODYNAMIC PARAMETERS OF LEAD SULFIDE CRYSTALS IN THE CUBIC PHASE

T.O. PARASHCHUK, A.V. ZAGORODNYUK, L.I. NYKYRUY, B.P. VOLOCHANSKA,

T.M. MAZUR

Abstract. Geometric and thermodynamic parameters of cubic PbS crystals were obtained using the computer calculations of the thermodynamic parameters within density functional theory method DFT. Cluster models for the calculation based on the analysis of the crystal and electronic structure. Temperature dependence of energy ΔE and enthalpy ΔH, Gibbs free energy ΔG, heat capacity at constant pressure CP and constant volume CV, entropy ΔS were determined on the basis of *ab initio* calculations of the crystal structure of molecular clusters. Analytical expressions of temperature dependences of thermodynamic parameters which were approximated with quantum-chemical calculation points have been presented. Experimental results compared with theoretically calculated data.

Keywords: DFT, cluster models, quantum-chemical calculations, thermodynamic properties, IV-VI semiconductor materials, Lead Sulfide.

1. INTRODUCTION

About the unique properties of lead sulfide was known long ago. Striking evidence of this can serve its first use in thermoelectric generators.

Effective use of this compound due to its low thermal conductivity at high temperatures [1], a lot ellipsoidal character of energy spectrum (N=4), low lattice thermal conductivity (~2.092 J/m·K) at relatively high carrier mobility (~0.1 m^2/V s), high values of permittivity, low values of the band gap (0.41 eV [2]) [3] and their positive change with temperature [4], which are factors that contribute the efficient use of the material in thermoelectricity. Also, it is important to note that the band gap of lead sulfide is the highest among other lead chalcogenide compounds. Widespread industrial use of this material contributes to its low cost and availability of natural compound (mineral of galena). The combination of lead chalcogenides in solid solutions allows to achieving of higher performance thermoelectric efficiency.

Actually this compound is used in thermoelectricity, optoelectronics and spintronic devices, especially in the long-wavelength range, for manufacturing of infrared diode lasers and thermophotovoltaic power converters [3]. Such wide range of materials application requires in-depth

study of their properties at different conditions and dependence of these crystals properties with changing of external factors. Interest in such studies is due to the fact that often data are ambiguous or completely absent.

First principle calculations are convenient and quite accurate approaches for modelling of structure and finding of thermodynamic properties of crystals which are widely used in modern research [1], [5], [6]. They permit to obtain reliable data about the properties of crystalline solids and implement their theoretical interpretation using a relatively minor cost of machine time and minimum set of input parameters.

Use of the computer quantum chemistry calculations caused by the possibility of investigations of short-range order of the atoms in real crystals and analysing of the properties caused by them. It is also important, that intensive research of atomic clusters as components of new nanostructured materials is caused by the perspective application in nanotechnology.

2. METHOD OF CALCULATION

Within the rigid molecule approximation [7] the enthalpy H of crystals is defined as:

$$H \approx H_{elec} + H_{vib}^{0} + H_{vib}(T) + H_{rot}(T) + H_{trans}(T) + RT, \quad (1)$$

there H_{elec} is the electronic component of enthalpy, H_{vib} is the vibration component of enthalpy, H_{vib}^{0} is the enthalpy of the main state vibrations, H_{rot} is the rotational component of enthalpy, H_{trans} is the progressive component of enthalpy, R is the universal gas constant, T is the temperature. The energy E was calculated similarly.

Entropy of crystal generally determined as the sum of components:

$$\Delta S = S_{trans} + S_{rot} + S_{vib} + S_{elec} - nR[\ln(nN_0) - 1], \quad (2)$$

there N_0 is the the Avogadro constant, n is the number of moles in molecules.

It is possible to calculate the Gibbs free energy of the crystal at a given temperature T using contributions of zero-point energy and entropy of individual members of molecules reagents *A (Pb)* and *B (S)*.

$$\Delta G = H_A - H_B + \frac{1}{2}\sum_{i\in A} h\nu_i - \frac{1}{2}\sum_{j\in B} h\nu_j - T\left(S_{vibr}^{A} - S_{vibr}^{B} + S_{rot}^{A} - S_{rot}^{B} + S_{trans}^{A} - S_{trans}^{B}\right) \quad (3)$$

At calculations of ΔE, ΔH, ΔS and ΔG we used the following method of the initial conditions consideration as shown at the calculations of energy ΔE. Initially, the energy ΔE_A of cluster *A* (fig. 1, A) was calculated according to [8] using formula:

$$\Delta E_A = E - \sum E_{el} + \sum E_{at}\,, \quad (4)$$

there E is the total energy of system; $E_{el}$is the energy of electrons in atoms that constitute the system (in atomic state); E_{at} is the atomization energy. Total energy and electron energy of system were taken from the calculation results, all other values were from reference [9]. The energies ΔE_B, ΔE_C and ΔE_D of clusters *B*, *C* and *D* accordingly (Fig. 3, B, C, D) have been calculated similarly.

On the base of calculations of the vibrational spectra was calculated thermodynamic properties in PbTe crystals at different temperatures (Fig.2-4).

As a result of quantum - chemical calculations we obtained the system of equations, which is as follows:

$$\begin{cases} 8x_3 + 24x_4 + 24x_6 = A, \\ 24x_3 + 24x_5 + 8x_6 = B, \\ 8x_3 + 12x_4 + 6x_5 + x_6 = C, \\ 8x_3 = D; \end{cases} \quad (5)$$

there $x_3,\ x_4,\ x_5,\ x_6$ are the values of the quantities for two -, four-, five- and six coordinated atoms respectively.

The solution of this system relatively to x_6 was obtained by the following ratio:

$$x_6 = \frac{2A-B}{4} + \frac{5D}{4} - C, \tag{6}$$

there A, B, C, D are the thermodynamic values for the respective clusters.

Heat capacity at constant volume C_V (similarly for C_p), according to these approximations determined by the following formula:

$$C_V = C_{V(trans)} + C_{V(rot)} + C_{V(rib)}. \tag{7}$$

Contributions of translational degrees of freedom calculated without data of quantum-chemical calculations because they depend on external factors (T, P) and mass of the molecule m.

Symmetrical relative equilibrium displacement of nuclei leads to a symmetric potential energy changes according to the contribution of vibrational component in the harmonic approximation and defined by the equation:

$$C_{V(vibr)} = R\left(\frac{hc}{kT}\right)^2 \sum_i \frac{g_i v_i^2 e^{-\frac{hcv_i}{kT}}}{\left[1-e^{-\frac{hcv_i}{kT}}\right]^2}\ , \tag{8}$$

there g_i is the the degeneration degree of i^{th} vibration.

According to [10] the temperature dependence of the specific heat capacity of crystal structures determined by the following function:

$$C = a + b \cdot 10^{-3}T - c \cdot 10^{5}T^{-2}, \tag{9}$$

there a, b, c are the constants depend on the lattice type of crystal and type of chemical compound.

To comparison the obtained results the proposed models [1], [3], [10] and experimental data [11] were discussed. Theoretical calculation of heat capacity in [1] realized by direct force-constant method. Calculations of heats in [3] was performed using WIEN2K program developed by Blaha [12]. This program uses the full potential linearized associated plane waves (FP-LAPW) based on density functional theory. Calculations in [10] carried out within density functional theory too. Molar heat capacity measurement in [11] carried out on 0.034 kg samples of PbS in calorimeter at a high vacuum under the hood, the temperature was maintained constant. Calorimeter is a 0.03 m length and 0.03 m diameter cylinder soldered with a domed bottom. The upper part was sealed by Wood's metal with a thin-walled copper-nickel tube with 0.001 m outer diameter and 0.2 m length attached. Constantan wire was used as heaters and thermometer is a platinum wire. Temperature drift recorded before and after the establishment of internal equilibrium. Measurements carried out in the temperature range from 20 to 260 K. In paper [13] values of isobaric molar heat capacity measured on analysing of thermal installation (Dupont 1090B, USA) were listed. Which are also in good agreement with values obtained by us.

3. CLUSTER MODELS

High level of modern scientific and technological progress is largely due to the development of theoretical research methods. However, these achievements would be impossible without the latest computer technology advances. First of all, they contribute to the improvement of model studies and are extremely convenient for expansion and deepening of information about the structure and properties of matter.

Rock salt structure was selected for modelling studies because lead chalcogenides crystallize in the face-centred cubic lattice NaCl (structural type B1) with the lattice parameter a=5,936 Å [13] for PbS compound, space group was $Fm3m-O_h^5$. These atom locations can be explained by the fact that lead chalcogenides belonging to polar semiconductors, characterized by ion-covalent type of bond.

This structure allows to build clusters without additional atoms that are introduced for compensation of dangling bonds. Crystal structures of lead sulfide were investigated using four models with 64, 56, 27 and 8 atoms accordingly. In constructing of clusters the most attention was paying to symmetry and electric charge of clusters for elimination of the structure distortion due to the action of surface forces. This approach has been successfully used for the construction of cluster models in II-VI compounds [14], [15].

The first cluster model (with general formula $Pb_{32}S_{32}$, Fig. 1, a) is basic for calculation of the spatial and electronic structure and thermodynamic quantities. This model consists of 64 atoms and contain 4 pairs of six coordinated atoms, 12 pairs of five coordinated, 12 pairs of four coordinated and 4 pairs of three coordinated atoms.

The second cluster has a general formula $Pb_{28}S_{28}$ (Fig. 1, b) and consists of 56 atoms. It includes 4 pairs of six coordinated atoms, 12 pairs of five coordinated and 12 pairs of three coordinated atoms.

The third cluster model constructed of 27 atoms and has the chemical formula $Pb_{14}S_{13}$ (Fig. 1, c). This structure includes one six coordinated atom, 6 pairs of five coordinated, 12 pairs of four coordinated and 8 pairs of three coordinated atoms.

The fourth cluster with the Pb_4S_4 formula (Fig. 1, d) composed of 8 three coordinated atoms.

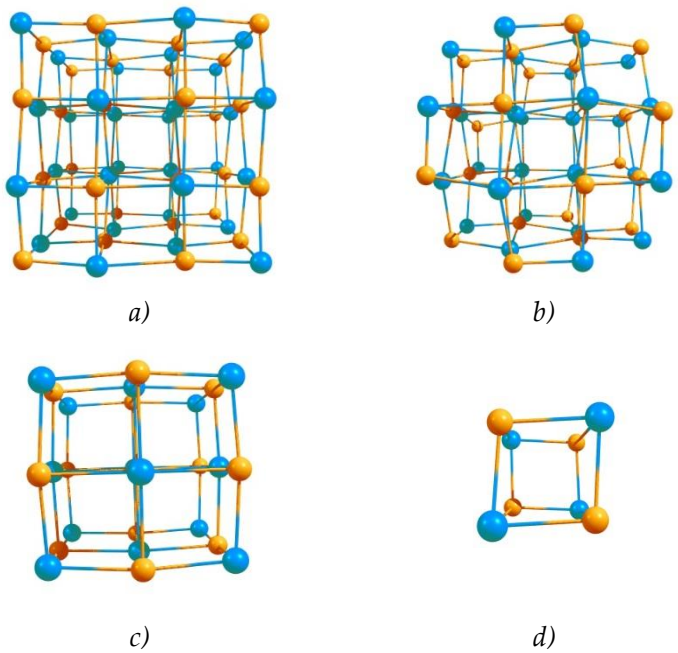

Fig. 1. Theoretical cluster models for PbS crystals with general formula $Pb_{32}S_{32}$: (a), $Pb_{28}S_{28}$: (b), $Pb_{14}S_{13}$: (c), Pb_4S_4: (d).

The first step for the quantum-chemical calculation of the cluster properties was the determination of the lowest energy configuration. All calculations started with SCF convergence and geometry optimization; after obtaining a stable minimum, the frequencies were calculated. The calculations were carried out using density functional theory, on the basis of the Stevens–Basch–Krauss–Jasien–Cundari (SBKJC) [16] parameterization. In this basic set only the valence electrons which are directly involved in chemical bonding are considered. This basic set was chosen due to our previous experience with it in several vibrational studies carried out by group II-VI [17], [18]. DFT calculations were performed by using Becke's three parameter hybrid method [19] with the Lee, Yang, and Parr (B3LYP) gradient corrected correlation functional [20] using the PC Gamess program packages [21]. The visualization of the spatial structures was carried out using Chemcraft.

This approach makes possible to create the equations system (5) for the thermodynamic variables of selected clusters. Solving it, we got the values of these parameters for six coordinated atoms that made up NaCl structure.

Comparing of calculated by us lattice constant value of a=5,92 Å is extremely close to obtained in paper [22] data a=5,938 Å calculated using the PBEsol exchange-correlation functional and presented there experimental result a=5,933 Å. Seeing the deviations within ~1% indicate that DFT calculations reproduce the absolute values of the lattice constants reasonably well. Our results may be a good addition to the temperature dependences of lattice constants, volumetric expansion coefficients and bulk models were carried out using the Phonopy package, with VASP using the PBEsol exchange-correlation functional [22]. Small shifting of Pb atoms is associated with the softening of phonons at high temperatures within the quasi-harmonic approximation based on phonon-phonon interactions in many-body perturbation theory.

4. Results and Discussion

The dependences of energy ΔE, enthalpy ΔH, Gibbs free energy ΔG, entropy ΔS and heats capacities at constant volume C_V and constant pressure C_p for PbS crystals at temperatures from 20 K to 1000 K are presented on fig. 2-4. Their analytical expressions can be introduced by the next dependencies:

$$\Delta S(T) = 13.001 \cdot lnT - 10.5 \quad (10)$$

$$\Delta G(T) = 100.17 + 0.0382 \cdot T \quad (11)$$

$$\Delta E(T) = 0.0158 \cdot T + 100.05 \quad (12)$$

$$\Delta H(T) = 0{,}0158 \cdot T + 100{,}05 \quad (13)$$

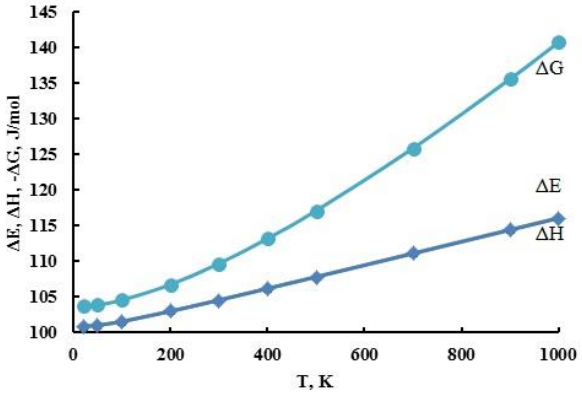

Fig. 2. The temperature dependence of energy ΔE and enthalpy ΔH, Gibbs free energy ΔG for cubic PbS crystals.

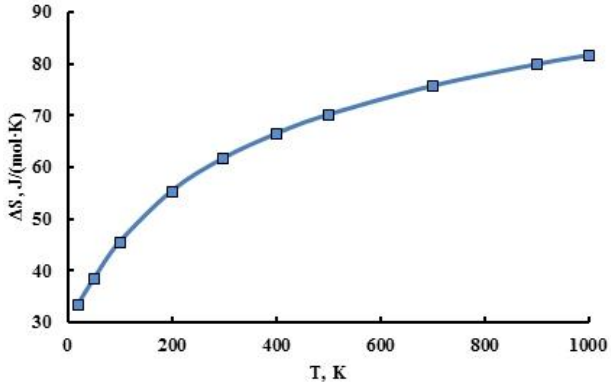

Fig. 3. The temperature dependence of entropy ΔS for cubic PbS crystals.

Obtained by us, the analytical expressions of the temperature dependences of heat capacity at constant volume CV and constant pressure CP, which were approximated by quantum-chemical calculation points using the mathematical package Maple14, are shown by the following equations:

$$C_V = 39{,}38 + 13{,}661 \cdot 10^{-3}T - 0{,}1312 \cdot 10^{5}T^{-2}\,, \quad (14)$$

$$C_p = 41{,}315 + 13{,}910 \cdot 10^{-3}T - 0{,}1382 \cdot 10^{5}T^{-2}. \quad (15)$$

As for crystal structure, the minor deviation from the perpendicular relative position of sides was observed also in structure modelling lead selenide by authors [23], who used calculation program GAUSSIAN 03 and SBKJC base set. These results do not contradict to experimental data given in [2],

and to data of structural cards given in [24], where among compounds of lead chalcogenides are on the side of PbS cubic structure near the boundary between the cubic and orthorhombic modifications.

Received dependences are consistent with the theory of solid state physics. The increase of entropy with the increasing of temperature is reasonable, because of system energy increase and hardness of test material decrease. Since all thermodynamic parameters can be defined using other thermal characteristics, their direct dependence on the temperature increase can be totally explained by classical theory of solid state physics.

Also it is important that during calculation the temperature dependence of heat capacities were adjusted to 0 K. At calculations we use models that include the phonon contribution at the heat capacity which is a combination of Debye and Einstein functions, and the electronic component. The received values of heat capacity at constant volume C_V and constant pressure C_p at different temperatures are shown in Fig. 4. A good coincidence with theoretical data can be considered by obtained calculation data approach to the classic Dulong and Petit law. In low-temperature range the values are proportional to T^3, which corresponds to Debye theory. We also carried out the comparison of our results with the calculation results [1], [3], [10] and measured experimental values [11], [13]. During analysis of received data is observed coincidence of our results with previously obtained results within 2% error.

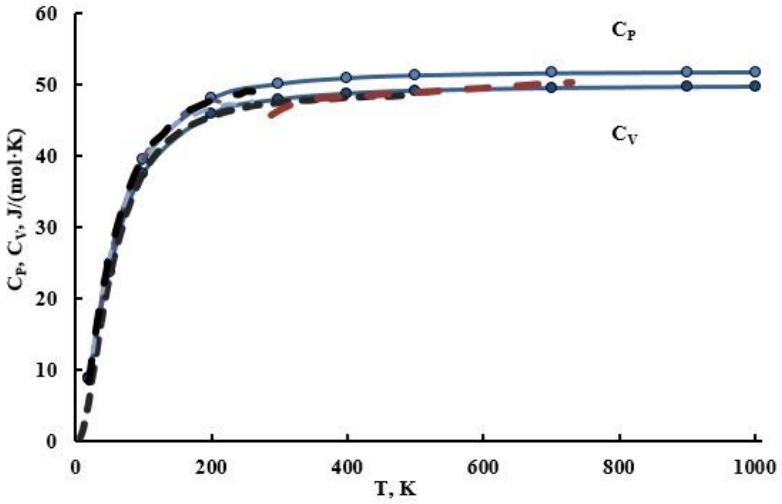

Fig. 4. Temperature dependence of isochoric C_V and isobaric C_P heat capacities: ○- quantum-chemical calculation; line - approximation of analytical functions (14, 15); intermittent lines - results of calculations [1], [3], [10].

The deviations of theoretically calculated equilibrium structure from values which are typical for rock salt lattice type can be explained by a significant deviation of the lattice spectrum from Debye theory [25]. Ionisity is an important factor that constrains phase transitions. Spin-orbital interaction is characterized by similar effect because it violates the congruence of the Fermi surface. The values for lead chalcogenides are large, which explains by the absence of transitions for these compounds [26].

5. CONCLUSION

Based on the crystal and electronic structures of cubic PbS and paying attention to their physical and chemical properties, cluster models for calculating the thermodynamic parameters of cadmium telluride have been proposed. A method of consideration of the boundary conditions for cluster models of a PbS crystal at the cubic phase has been shown.

Temperature dependences of the thermodynamic parameters of the PbS crystals have been defined: energy ΔE, enthalpy ΔH, entropy ΔS and Gibbs free energy ΔG. These results can be used to predict properties of PbS crystals during annealing.

From the first principles' calculations we have been received the analytical expressions for the temperature dependences of the specific heat capacity of the PbS crystals in cubic phases at constant volume CV and constant pressure CP.

A good coincidence of the results with similar calculations and experimental data was received.

ACKNOWLEDGMENT

This research is sponsored by by NATO's Public Diplomacy Division in the framework of "Science for Peace" (NATO SPS G4536).

REFERENCES

[1] Zhang Y., Ke X., Chen C., Yang J., Kent P.R.C. Thermodynamic properties of PbTe, PbSe, and PbS: First-principles study. *Physical Review B,* **80** (024304) (2009).

[2] Sun Q., Wang Y., Yuan X., Han J., Ma Q., Li F., Jin H., Liu Z. Preparation of PbS nano-microcrystals with different morphologies and their optical properties. *Cryst. Res. Technol*., **48** (9) (2013), 627-631. doi: 10.1002/crat.201300189

[3] Boukhris N., Meradji H., Amara Korba S., Drablia S., Ghemid S., El Haj Hassan F. First principles calculations of structural, electronic and thermal properties of lead chalcogenides PbS, PbSe and PbTe compounds. *Bull. Mater. Sci*., **37** (5) (2014), 1159-1166.

[4] Ravindra N.M., Srivastava V.K. Properties of PbS, PbSe, and PbTe. *Phys. Stat. Sol. (a),* **58** (1980), 311-316.

[5] De Leon A., Ramírez-Bon R., Castillo S.J. Theoretical study of starch as a novel substrate for PbS. *Chalcogenide Letters,* **11** (5) (2014), 209-217.

[6] Yu Y., Fang D., Zhao G.D., Zheng X.L. Ab initio calculation of the thermodynamic properties of wurtzite ZnS: performance of the LDA and GGA. *Chalcogenide Letters,* **11** (12) (2014), 619-628.

[7] Medvedev S. A. *Physics and chemistry of compounds AII BVI*. Moscow, 1970.

[8] Haynes W.M. *CRC handbook of chemistry and physics: a ready-reference book of chemical and physical data*. CRC Press, Boca Raton, Fla, 2010.

[9] Ravdel A.A., Ponomareva A.M. (Eds.) *Short Guide of physical and chemical quantities*, *9th Edition*. Special literature, St. Petersburg, 1998.

[10] Bencherif Y., Boukra A., Zaoui A., Ferhat M. Lattice dynamics study of lead chalcogenides. *Infrared Physics & Technology,* **54** (2011), 39-43. doi:10.1016/j.infrared.2010.11.001

[11] Parkinson D.H., Quarrington J.E. The molar heats of lead sulfide, selenide and telluride in the temperature range 20 K to 260 K. *Proc. Phys. Soc. A,* **67** (1954), 569.

[12] Laskowski R., Blaha P., Schwarz K. Bonding of hexagonal BN to transition metal surfaces: An ab initio density-functional theory study. *Physical Review B,* **78** (045409) (2008). doi:10.1103/PhysRevB.78.045409

[13] Pei Y.-L., Liu Y. Electrical and thermal transport properties of Pb-based chalcogenides: PbTe, PbSe, and PbS. *Journal of Alloys and Compounds,* **514** (2012), 40-44. doi:10.1016/j.jallcom.2011.10.036

[14] Freik D.M., Parashchuk T.O., Volochans'ka B.P. Heat Capacity and Debye Temperature of CdTe, CdSe Crystals. *Physics and Chemistry of Solid State,* **15** (2) (2014), 282-287.

[15] Freik D., Parashchuk T., Volochanska B. Thermodynamic parameters of CdTe crystals in the cubic phase. *Journal of Crystal Growth,* **402** (2014), 90-93. doi:10.1016/j.jcrysgro.2014.05.005

[16] Stevens W.J., Basch H., Krauss M. *J. Chem. Phys*., **81** (6026) (1984).

[17] Ahiska R., Freik D., Parashchuk T., Gorichok I. Quantum chemical calculations of the polymorphic phase transition temperatures of ZnS, ZnSe, and ZnTe crystals. *Turk. J. Phys*., **38** (2014), 125-129. doi:10.3906/fiz-1301-7

[18] Parashchuk T.O., Freik N.D., Fochuk P.M. DFT-Calculations of Thermodynamic Parameters of ZnTe, ZnSe, ZnS Crystals. *Phys. Mater. Chem*., **2** (1) (2014), 14-19.

[19] Becke A.D. Density-functional thermochemistry. III. The role of exact exchange. *J. Chem. Phys.,* **98** (7) (1993), 5648-5652. doi:10.1063/1.464913

[20] Lee C., Yang W., Parr R. G. Development of the Colle-Salvetti correlation-energy formula into a functional of the electron density. *Phys. Rev. B*, **37** (2) (1988), 785. doi:10.1103/PhysRevB.37.785

[21] Granovsky Alex A. PC GAMESS version 7.0. Available at: http://classic.chem.msu.su/gran/gamess/index.html.

[22] Skelton J.M., Parker S.C., Togo A., Tanaka I., Walsh A. Thermal physics of the lead chalcogenides PbS, PbSe, and PbTe from first principles. *Physical Review B,* **89** (205203) (2014). doi:10.1103/PhysRevB.89.205203

[23] Kiran B., Kandalam Anil K., Rallabandi R., Koirala P., Li X., Tang X., Wang Y., Fairbrother H., Gantefoer G., Bowen K. (PbS)32: A baby crystal. *The Journal of Chemical Physics,* **136** (024317) (2012). doi:10.1063/1.3672166

[24] Littlewood P.B. Physics of Narrow Gap Semiconductors. Proceedings of the 4th International Conference on Physics of Narrow Gap Semiconductors. Linz, Austria, 1981.

[25] Shelymova L.Ye. *Inorganic Materials*, **24** (10) (1988), 1597.

[26] Volkov B.A., Pankratov O.A. Crystal structures and symmetry of the electron spectrum of IV-VI semiconductors. *Journal of Experimental and Theoretical Physics*, **48** (4) (1978), 687-696.

Address: T.O. Parashchuk, Ivano-Frankivsk National Medical University, 2, Halytska Str., Ivano-Frankivsk, 76018, Ukraine;
A.V. Zagorodnyuk, L.I. Nykyruy, B.P. Volochanska, Vasyl Stefanyk Precarpathian National University, 57, Shevchenko Str., Ivano-Frankivsk, 76018, Ukraine;
T.M. Mazur, Ivano-Frankivsk National Technical University of Oil and Gas, 15, Karpatska Str., Ivano-Frankivsk, 76000, Ukraine.
E-mail: liubomyr.nykyrui@pu.if.ua; azagorodn@gmail.com.
Received: 25.01.2016; **revised:** 29.03.2016.

———————————

Паращук Т.О., Загороднюк А.В., Никируй Л.І., Волочанська Б.П., Мазур Т.М. Термодинамічні параметри кристалів PbS у кубічній фазі. *Журнал Прикарпатського університету імені Василя Стефаника*, **3** (1) (2016), 15–22.

Отримано геометричні та термодинамічні параметри кубічних кристалів PbS на основі комп'ютерних розрахунків термодинамічних параметрів у рамках теорії функціоналу густини. (DFT). Кластерні моделі для розрахунку базувалися на аналізі кристалічної та електронної структури. Температурна залежність енергії ΔE та ентальпії ΔH, вільна енергія Гіббса ΔG, теплоємності при сталому тиску Cp і сталому об'ємі CV, а також ентропія ΔS визначено на основі розрахунків кристалічної структури молекулярних кластерів із перших принципів. Отримано аналітичні вирази температурних залежностей термодинамічних параметрів, які апроксимовано з даними квантово-хімічних розрахунків. Експериментальні результати порівняно із теоретично розрахованими даними.

Ключові слова: теорія функціоналу густини, кластерні моделі, квантово-хімічні розрахунки, термодинамічні параметри, напівпровідники IV-VI, сульфід свинцю.

Journal of Vasyl Stefanyk Precarpathian National University
http://jpnu.pu.if.ua
Vol. 3, No. 1 (2016), 23-28

UDC 541.1, 5367, 621.794
PACS numbers: 75.75.Cd, 76.80.+y
doi: 10.15330/jpnu.3.1.23-28

THE STRUCTURE OF THE ELECTRODE MATERIAL BASED ON $Ni(OH)_2$/C COMPOSITE FOR ENERGY STORAGE DEVICES

O.M. KHEMIY, L.S. YABLON, I.M. BUDZULYAK, O.V. MORUSHKO

Abstract. The paper presents the results of studies of the structure β-$Ni(OH)_2$/C composite. It is shown that the XRD-pattern of heated composite β-$Ni(OH)_2$/C has a broad diffraction peak at 23°, which can be attributed to the activated carbon in addition to peaks characteristic for NiO.

Keywords: nickel hydroxide, activated carbon, thermogravimetry, X-ray analysis, galvanostatic and potentsiodynamic methods, the accumulation of charge.

1. INTRODUCTION

The specific capacitance of electrochemical capacitors (ECs) is one of the basic characteristics that define the area of their use. Therefore, the main efforts of researchers are focused at finding new methods and materials that facilitate the achievement of this goal. The idea of using hybrid systems and materials for electrodes that provide fast reversible Faradaic reactions is the most promising. It can be used in EC with pseudocapacitance accumulation of energy [1]. Currently ECs are formed from such oxides as ruthenium and iridium, but they are not used commercially due to the high cost.

Among the cheap and available electrode materials, nickel hydroxide ($Ni(OH)_2$) is of particular interest. There are two polymorphs of the nickel hydroxides [2], which are denoted as α-$Ni(OH)_2$ and β-$Ni(OH)_2$, respectively. β-phase $Ni(OH)_2$ is isostructural with brucite $Mg(OH)_2$. Since this material has trigonal symmetry, it should be noted that the a- and b-axis in Fig. 1 is not orthogonal, and the angle between them is 120°.Although α - phase has a higher theoretical capacitance, but it is unstable in alkaline and fast becomes more stable β-$Ni(OH)_2$ [3].

In addition to the two fundamental phases of nickel hydroxide there are several possible types of structural disorder, including the incorporation of foreign ions, defects in the crystal lattice and others [4]. The effects of structural disorder can have very important practical implications, particularly, well-crystallized β-$Ni(OH)_2$ has a lower electrochemical activity than disordered β-$Ni(OH)_2$ [5]. Nowadays these materials are widely used, particularly in supercapacitors [6], photocatalysis [7] and electrochemical sensors [8].

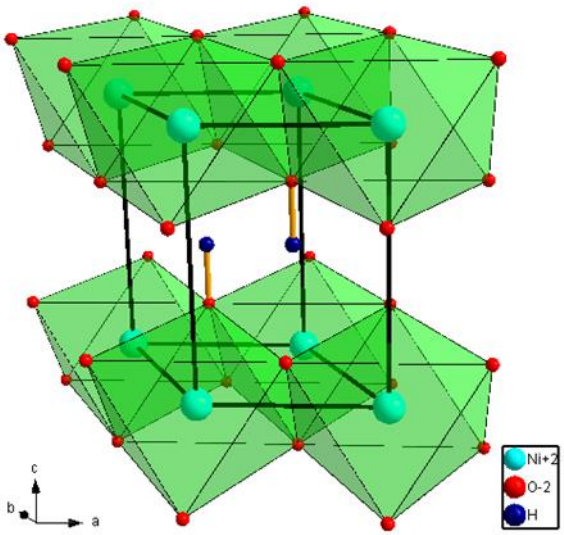

Fig. 1. The crystal structure of β-Ni(OH)₂.

2. METHODS AND MATERIALS

Nickel hydroxide and its composite with nanoporous carbon as electrode material of energy storage devices are studied. In this composite activated carbon reduces specific resistance and increases the power density. Activated carbon and β-Ni(OH)₂ was thoroughly mixed and then was heated at 50°C / min. in air to a temperature of 325°C, which was kept for 30 minutes. The choice of the temperature was determined that at this temperature the decomposition of β-Ni(OH)₂ to nickel oxide and water occurs [9]. Cooling of composite was carried out in mode excluded oven. The crystal structure of nickel hydroxide and Ni(OH)₂/C composite was studied using X-ray diffraction analysis (CuKα - radiation) in the range of angles $10° < 2\theta < 90°$. The method of thermogravimetry was used for the above given samples during their heated in the temperature range 20 - 800°C in air with a heating rate of 10°C / min. This method was used to understand the change of mass and heat, and, accordingly, the optimum temperature of forming the composite. Researches were conducted simultaneous thermal analyzer STA 449 F3 Jupiter. Empty crucible of Al_2O_3 was used as a comparative standard. The sample was heated with a reference sample and current temperature of the sample and difference of the temperature between the sample and standard were recorded. This allows to fix processes associated with absorption or release of energy.

3. RESULTS AND DISCUSSION

Fig. 2 shows XRD pattern of the initial Ni(OH)₂ and Ni(OH)₂/C composite. It can be seen from Fig. 2 that all of the diffraction peaks can be indexed to a pure hexagonal structure of β-Ni(OH)₂ ($P\bar{3}m1$), no diffraction peaks from impurities are found in the sample. According to the Debye-Scherrer formula, the calculated grain sizes are 14.9 nm, which is in accordance with the reported values [10]. In the case of composite, diffraction peaks are wider and have lower intensity, which indicates the presence of amorphous activated carbon.

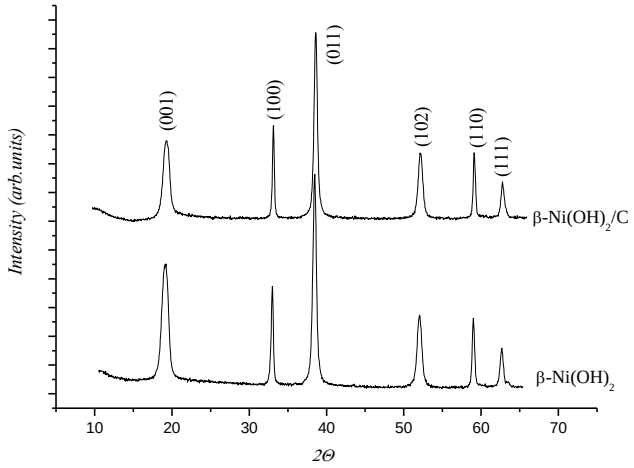

Fig. 2. XRD pattern of the initial $Ni(OH)_2$ and $Ni(OH)_2$/C composite.

Thermal behavior of β-$Ni(OH)_2$ was investigated using thermogravimetric (TG) and differential thermal analysis (DTA). As shown in Fig. 3 (curve TG) weight of β-$Ni(OH)_2$ decreases rapidly at temperatures of 285 - 325°C, with a 22% weight loss. It is known [9] that the decomposition of β-$Ni(OH)_2$ to NiO and water occurs in the range of temperature 298 - 340°C. As a result, residue can reasonably be ascribed to NiO. The DTA curve (Fig. 3) showed endothermic peak with a maximum located at 320°C, which is consistent with the weight loss of the material.

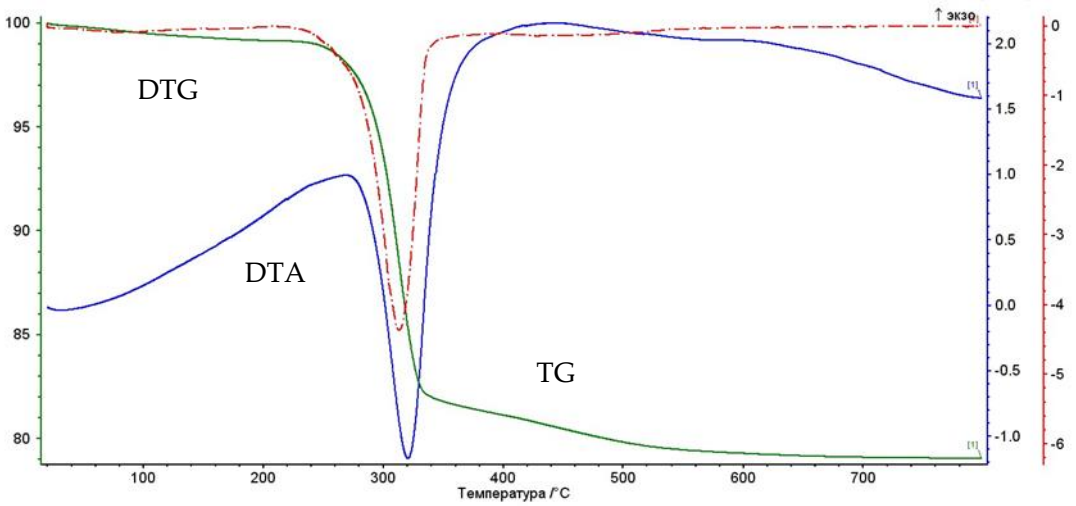

Fig. 3. Differential thermal analysis (DTA) and thermogravimetric analysis (TG) curves of β-$Ni(OH)_2$.

The composition and phase purity of β-$Ni(OH)_2$, heated at 325°C was investigated using X-ray diffraction analysis (Fig. 4). According to XRD pattern, after heating only face-centered cubic structure NiO was formed ($Fm\bar{3}m$). Thus β-$Ni(OH)_2$ is completely converted to NiO after heating to 325°C.

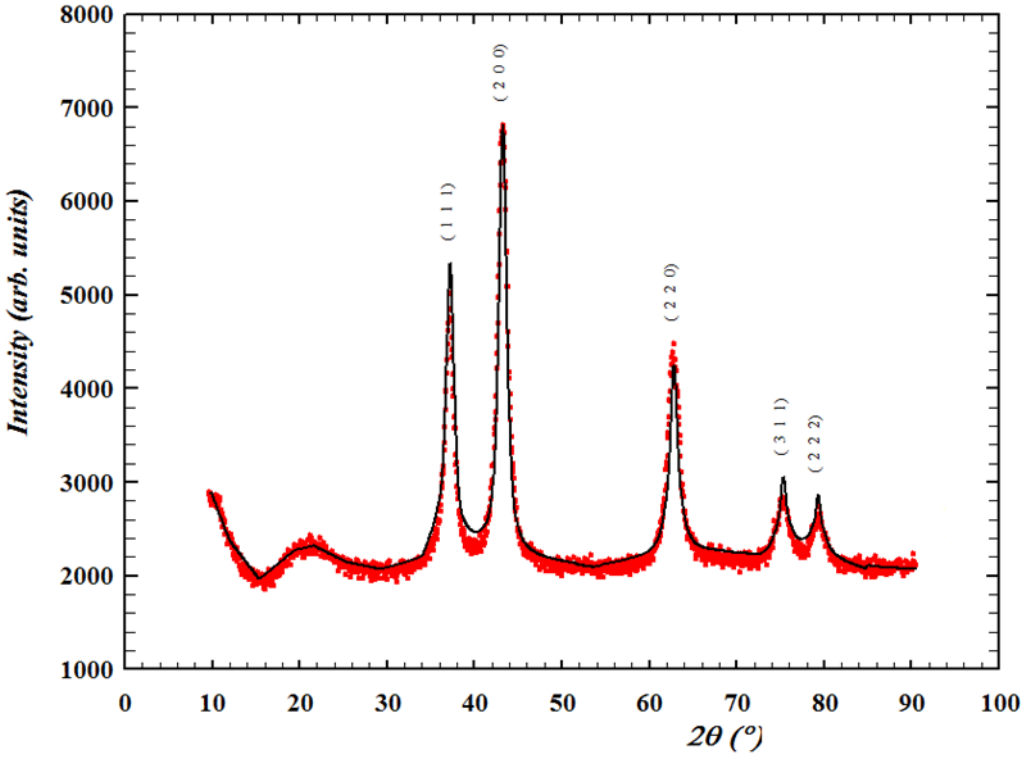

Fig. 4. XRD pattern of the β-Ni(OH)₂ heated to a temperature of 325°C (phase NiO).

β-Ni(OH)₂/C composite underwent a two-step weight loss due to dehydration and decomposition (Fig. 5). The two endothermic peaks at 130 and 325°C on the DTA curve are indicative of two successive stages of these physical-chemical changes during the heat treatment. The initial weight loss to 140°C is attributed to the loss of surface adsorbed water. The weight loss in the range of 140 - 280°C is due to the removal of the crystalline water molecules.

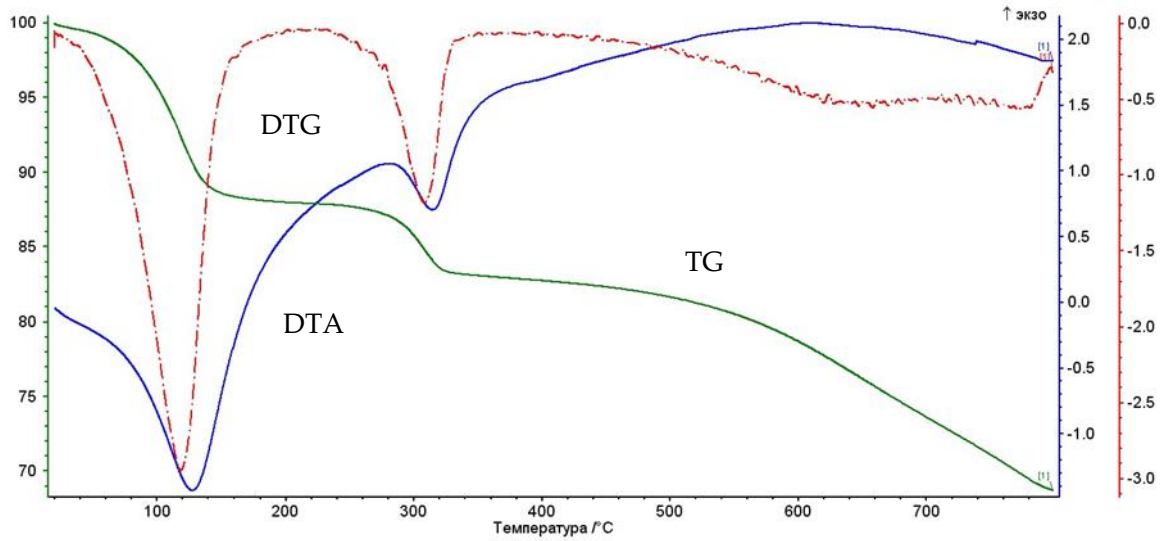

Fig. 5. Differential thermal analysis (DTA) and thermogravimetric analysis (TG) curves of β-Ni(OH)₂/C composite.

There is a broad diffraction peak at 23° (Fig. 6) in XRD-pattern of heated composite, which can be attributed to activated carbon.

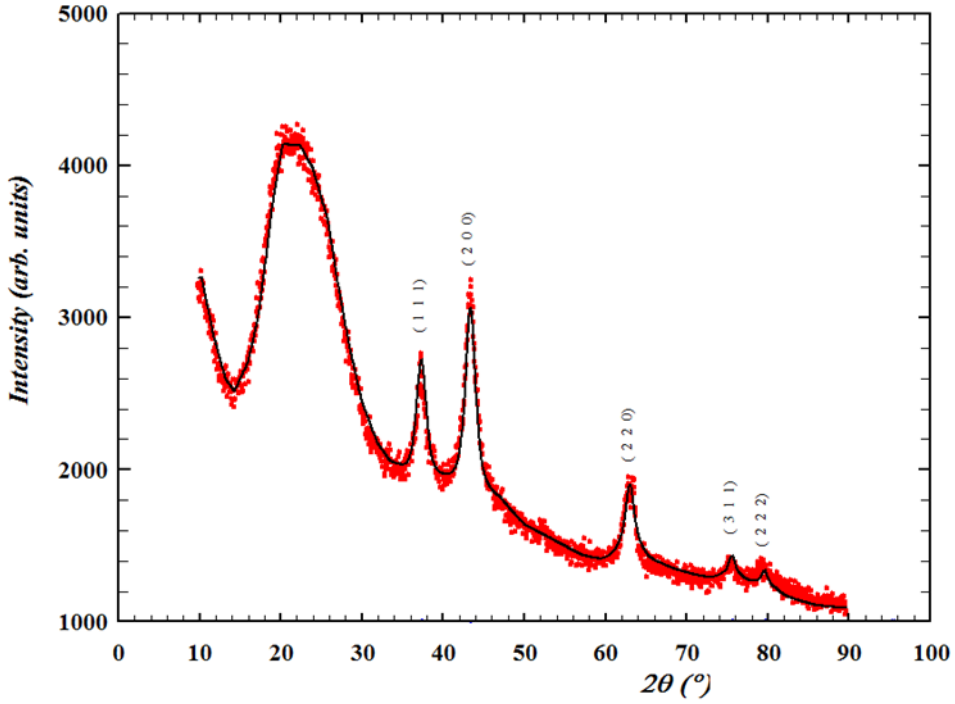

Fig. 6. XRD pattern of the β-Ni(OH)₂ / C composite heated to a temperature of 325 ° C.

Based on DTA and TG curves was found that the original weight of β-Ni(OH)₂ and the composite material decreases rapidly in the temperature range 285 - 325°C, which is associated with the formation of a stable residue of NiO. This is confirmed by X-ray diffraction analysis. XRD pattern heated Ni(OH)₂/C composite shows that there is a broad diffraction peak at 23°, which can be attributed to the activated carbon, besides the peaks characteristic of NiO.

4. CONCLUSIONS

It is assumed that the weight loss of nickel hydroxide and composite β-Ni(OH)₂/C decreases rapidly in the temperature range 285-325°C, due to the decomposition β-Ni(OH)₂ and the formation of a stable nickel oxide. It is shown that the XRD-pattern of heated composite β-Ni(OH)₂/C has a broad diffraction peak at 23°, which can be attributed to the activated carbon in addition to peaks characteristic for NiO.

REFERENCES

[1] Khomenko V., Raymundo-Piñero E., Frackowiak E., Béguin F. High-voltage asymmetric supercapacitors operating in aqueous electrolyte. *Applied Physics A.*, **82** (4) (2006), 567-573. doi: 10.1007/s00339-005-3397-8

[2] McEwen R.S. Crystallographic studies on nickel hydroxide and the higher nickel oxides. *Journal of Physical Chemistry*, **75** (12) (1971), 1782–1789. doi: 10.1021/j100681a004

[3] Oliva P., Leonardi J., Laurent J.F., Delmas C., Braconnier J.J., Figlarz M., et al. Review of the structure and the electrochemistry of nickel hydroxides and oxy-hydroxides. *Journal of Power Sources*, **8** (2) (1982), 229-255. doi: 10.1016/0378-7753(82)80057-8

[4] Hall D.S., Lockwood D.J., Poirier S., Bock C., MacDougall B.R. Raman and Infrared spectroscopy of α and β phases of thin nickel hydroxide films electrochemically formed on nickel. *Journal of Physical Chemistry*, **116** (25) (2012), 6771–6784. doi: 10.1021/jp303546r

[5] McBreen J. *Nickel hydroxides*. In: Daniel C., Besenhard J.O. (Eds.) Handbook of battery materials. 2011, 149–168. doi: 10.1002/9783527637188.ch5

[6] Aghazadeh M., Ghaemi M., Sabour B., Dalvand S. Electrochemical preparation of α-$Ni(OH)_2$ ultrafine nanoparticles for high-performance supercapacitors. *Journal of Solid State Electrochemistry*, **18** (6) (2014), 1569–1584. doi: 10.1007/s10008-014-2381-7

[7] Ran J., Yu J., Jaroniec M. $Ni(OH)_2$ modified CdS nanorods for highly efficient visible-light-driven photocatalytic H2 generation. *Green Chemistry*, **13** (10) (2011), 2708–2713. doi: 10.1039/C1GC15465F

[8] Fan Y., Yang Z., Cao X., Liu P., Chen S., Cao Z. Hierarchical macro-mesoporous $Ni(OH)_2$ for nonenzymatic electrochemical sensing of glucose. *Journal of. Electrochemical Society*, **161** (10) (2014), B201–B206. doi: 10.1149/2.0251410jes

[9] Shangguan E., Chang Z., Tang H., Yuan X.Z., Wang H. Synthesis and characterization of high-density non-spherical $Ni(OH)_2$ cathode material for Ni-MH batteries. *International Journal of Hydrogen Energy*, **35** (18) (2010), 9716-9724. doi:10.1016/j.ijhydene.2010.06.096

[10] Rifaya Nowsath M., Theivasanthi T., Alagar M. Chemical Capping Synthesis of Nickel Oxide Nanoparticles and their Characterizations Studies. *Nanoscience and Nanotechnology*, **2** (5) (2012), 134-138. doi: 10.5923/j.nn.20120205.01

Address: O.M. Khemiy, L.S. Yablon, I.M. Budzulyak, O.V. Morushko, Vasyl Stefanyk Precarpathian National University, 57, Shevchenko Str., Ivano- Frankivsk, 76018, Ukraine.
E-mail: olchuk1991@mail.ru; yablon_lyubov@ukr.net; ivan-budzulyak@ukr.net; morushko@rambler.ru.
Received: 12.02.2016; **revised:** 10.04.2016.

Хемій О.М., Яблонь Л.С., Будзуляк І.М., Морушко О.В. Структура електродного матеріалу на основі композиту гідроксид нікелю / вуглець для пристроїв накопичення заряду. *Журнал Прикарпатського університету імені Василя Стефаника*, **3** (1) (2016), 23–28.

У роботі представлено результати досліджень структури композиту β-$Ni(OH)_2$/C. Показано, що на дифрактограмах спеченого композиту β-$Ni(OH)_2$/C крім піків характерних для NiO, спостерігається широкий дифракційний пік на 23°, який може бути віднесений до активованого вугілля.

Ключові слова: гідроксид нікелю, активований вуглець, термогравіметрія, Х-променевий аналіз, гальваностатичний та потенціодинамічний методи, накопичення заряду.

Journal of Vasyl Stefanyk Precarpathian National University
http://jpnu.pu.if.ua
Vol. 3, No. 1 (2016), 29-37

UDC 541.1, 5367, 621.794
PACS numbers: 75.75.Cd, 76.80.+y
doi: 10.15330/jpnu.3.1.29-37

THE EFFECT OF SO_4^{2-} SULPHATE ANIONS ON THE ULTRAFINE TITANIA NUCLEATION

V.O. KOTSYUBYNSKY, I.F. MYRONYUK, B.K. OSTAFIYCHUK, V.L. CHELYADYN,

A.B. HRUBIAK, I.I. HRYHORUK

Abstract. We have proposed and experimentally tested a phenomenological model of SO_4^{2-} sulphate anions effect on the titania nucleation during hydrolysis of titanium tetrachloride. Sulphate anions form the chelating bidentate complexes with primary $[Ti(OH)_h(OH_2)_{6-h}]^{(4-h)+}$ with the influence on the next olation process and promotion of anatase phase nucleation.

Keywords: hydrolysis, polycondensation, nucleation, anatase, sulphate anions.

1. INTRODUCTION

Ultrafine TiO_2 has wide range of highly promising applications in many different fields – from environmental oriented photocatalytic system (degradation of hazardous organic compound [1], waste water cleaning [2], direct decomposition of NO_x , SO_x and air purification [3] to novel fields of industry (sensor materials [4] , solar energy cells [5]. For all cases phase composition, particles size and state of surface are the most important characteristics which will determine catalytic reactivity, photosensitivity and adsorption properties of TiO_2. For example the decrease of particle size of titania leads to the catalytic activity rapidly increasing [6]. At the same time the photocatalyst properties are very sensitive to phase composition (the ratio of TiO_2 polymorphs – anatase, brookite and rutile) [7]. As a result the choice of titania synthesis method with the precisious control of its physicochemical parameters is the crucially important. The preparation of nanosized TiO_2 is possible with the using of different techniques. There are some different methods: Sol–gel [8], chemical precipitation [9], microemulsion [8], hydrothermal [10]. Sol–gel method is the most flexible techniques, temperature for nanosized oxide preparation. The variations of primary precursor types, hydrolysis conditions, temperature and pH reaction medium open the possibility to control nanocrystalline products nucleation and growth. Sol–gel method of titania obtaining typically is based on the the reactions of titanium alkoxides $Ti(OR)_n$ hydrolysis. The changing of these expensive chemicals on the cheaper precursor such as $TiCl_4$ is very promising for nanosized large scale manufacturing by soft chemical technique. Promising advantage of $TiCl_4$ hydrolysis is the possibility of additional control for sol-gel process polycondensation stage by using of additive ions in the reaction medium that leads to predicted nucleation of titania polymorphs specified phase. The aim of this paper is an investigation the effect of SO_4^{2-} sulphate anions on

oligomers polycondensation and oxide network formation stages of the titania nucleation during based on $TiCl_4$ hydrolysis sol-gel process.

2. Materials and Methods

Titanium tetrachloride $TiCl_4$ (Merck, 99,9%; specific density 1.73 g/cm^3 at 20°C) was cooled to 0°C with. Hydrochloric acid (36,0% aqueous solution) was added to titanium tetrachloride at the stabilized temperature with gaseous hydrogen chloride evaporation. $TiCl_4$: hydrochloric acid final volume ratio was 2:1. Sodium hydrocarbonate aqueous solution was added dropwise to sol of titanium oxychloride $TiOCl_2$ up to pH =5.0-5.5 under vigorous stirring. Gel formation was obserwed during all pH increasing process. The suspension of nanoparticles was kept at 80°C for 3 h with the next washing with distilled water until the absence of Na^+ and Cl^- ions. Precipitated TiO_2 was dried at the temperature of 150°C, obtained xerogels was marked as S1. The S2 material synthesis process was carried out in analogous was but on the initial stage crystalline dried Na_2SO_4 was added directly to titanium tetrachloride with stirring.

Diffraction patterns were obtained with the diffractometer DRON-4-07 equipped with a X-ray tube BSV28 (Cu K_α radiation, 40 kV, 30 mA). The Bragg-Brentano geometry type and Ni K_β -filter were used. A qualitative analysis was carried out with the use of ICSD structural models. The structural models for anatase and rutile were based on the ICSD ICSD #92363 [31] and ICSD #24780 [32], respectively. Copper powder annealed at vacuum (850 – 900°C for 4 h) with an average grain size of about 50 μm was used as reference sample for the determination of the instrumental peak broadening. Full width at half maximum (FWHM) for a diffraction peak of this reference sample at 2θ = 43.38° was 0.129°, therefore it permitted to distinguish the phases anatase and brookite. The size of the coherently scattering domains was calculated by the Scherrer equation [33]: $D = \frac{K\lambda}{\beta cos\theta}$, with K is the Scherrer constant (K = 0.9), λ is the wavelength (0.15405 nm), β the FWHM (in radians), and θ is the peak angular position. As profile shape, we used a combination of Gauss and Cauchy (dominated) functions.

Infrared spectra were recorded at Thermo-Nicolet Nexus 670 FT-IR spectrometer in the region of 4000 – 400 cm^{-1}. The mixture TiO_2 / KBr after vibrating milling was pressed into pellets and measured in the transmission mode.

The morphology of sample powders was studied by transmission electron microscopy (TEM) with a 100 kV microscope JEOL JEM-100CX II. The microscopic copper grid covered by a thin transparent carbon film was used as specimen support for TEM investigations.

3. Results and Discussion

The presence of sodium sulfate in the reaction medium abruptly affects on the phase state of the obtained materials (Fig. 1). Material obtained at the absence of Na_2SO_4 additive (S1) is a mixture of anatase and rutile with relative contents of 65±4 and 35±5 wt%, respectively. The average size of the coherently scattering domains (CSD) was about 14 nm for anatase and 9 nm for rutile, so the both phases are good crystallized. Meantime part of the material is in the close to amorphous state as evidenced the presence of halo on XRD pattern for 2θ=16-32°. Accordingly to synthesis conditions the formation of non-titania phase is unlikely. As the result, material consists of separated part of TiO_2 with different crystallinity degrees. The specific surface area of S1 sample was about 152 m^2 g^{-1}. The material S2 was close to amorphous ultrafine titania with clear structural features of anatase. The halo on XRD pattern is observed in this case too but it's relatively narrowed and shifted to larger 2θ. The average size of the coherently scattering domains (CSD) was about 4-5 nm (the analysis is complicated by low crystallinity of the material). The specific surface area for S2 sample was increased to 328 m^2 g^{-1}.

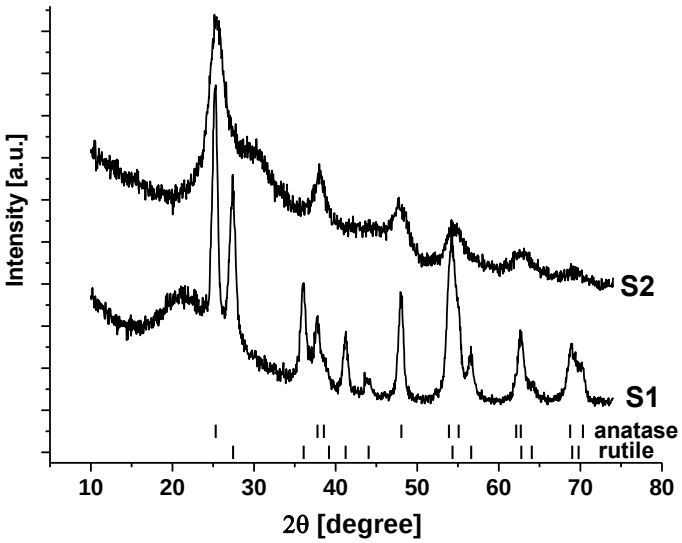

Fig. 1. XRD patterns of S1and S2 materials.

TEM images of S1 sample (Fig. 2, a) do not allow make the clear conclusions its morphology but on the agglomerates edges material consist of the lamellar-like primary particles with sizes about 10-15 nm. Simultaneously there is no any evidence of crystalline regions boundaries (Fig. 2, b). S2 sample (Fig. 2, c) has bauble-like morphology agglomerates consist of spherical primary particles. HR TEM allows directly observe good crystallinity some of separate grains with arranged atomic layers (Fig. 2, d). Accordingly to direct measurements evidence interplanar distances for crystalline domains vary in narrow range 0.34-0.37 nm (Fig. 3). The obtained interplanar spacing very good corresponds to the (101) plane of anatase (0.352 nm). It indicates the preferred growth direction of coherently scattering domains (crystallites) is [010] crystallography axis. This result correlates to conclusions that the anatase nanocrystals with oxygenated surfaces have developed facets in the ⟨010⟩ direction [11].

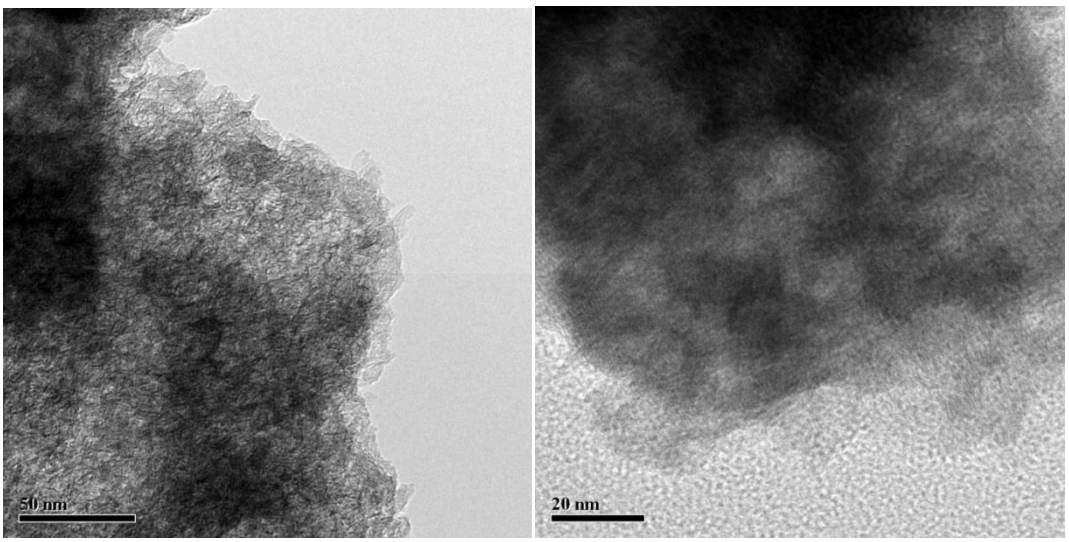

a) *b)*

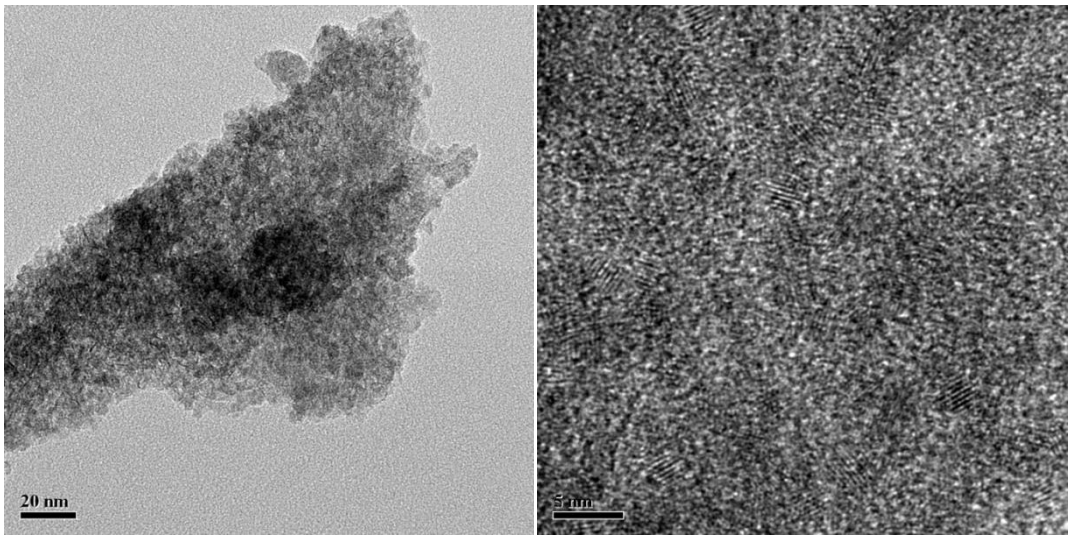

c) *d)*

Fig. 2. TEM images of the samples S1 (a,b) and S2 (c,d).

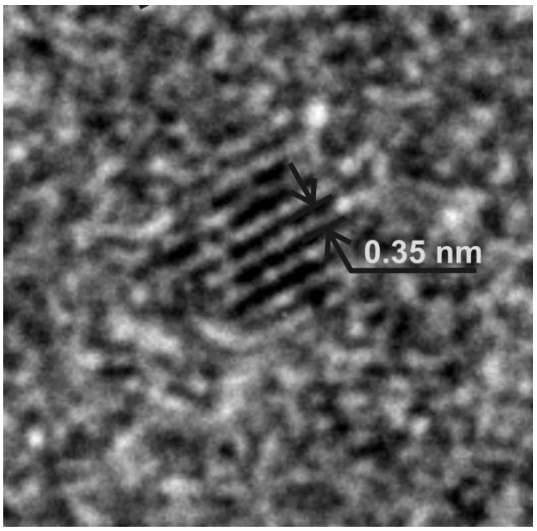

Fig. 3. HR TEM images of S2 material with the fringes from {101} planes.

Additional information about synthesized materials was obtained FT-IR spectroscopy (Fig. 4). The broad absorption region around 3400 cm^{-1} indicating the presence of chemisorbed OH groups on the titania particles surface (ν-OH modes) [12]. The shift of the ν-OH bands from typical 3700–3600 to about 3400 cm^{-1} can be caused the presence of hydrogen bonding [13]. The band around 1600 cm^{-1} demonstrates the presence of molecularly adsorbed water (δ-H_2O modes) [14]. The higher crystallinity degree for S1 sample causes the formation of relatively more distinct absortion bands in titania characteristic region (400-700 cm^{-1}) [15].

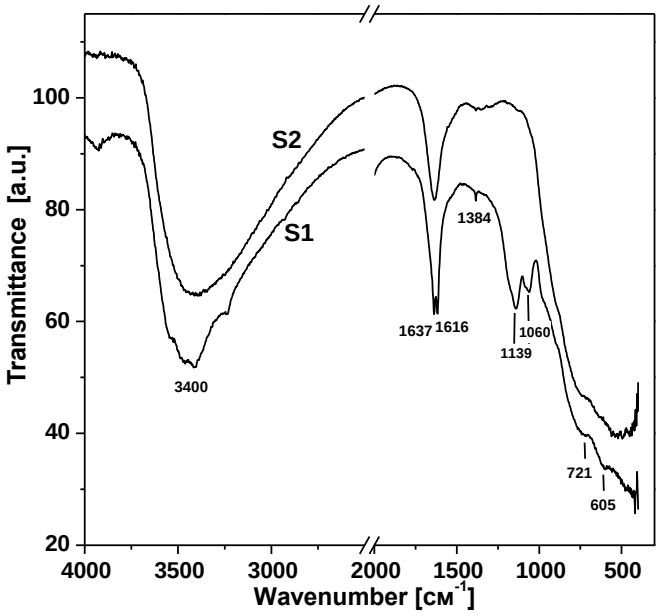

Fig. 4 FTIR spectra of S1and S2 materials.

The additional absorbance band on the FTIR patterns for S2 materials at 1139 and 1060 corresponding to chemisorbed SO_4^{2-} ions [16]. Sharp low intensity band 1384 cm^{-1} is typical for the metal oxides modified by sulfate ion bands and is assigned to S=O stretching frequency. Meantime S=O-H coordination is unlikely because in this case absorption band will shifts in low-frequencies region up to 1325 cm^{-1}.

There are two different variants of SO_4^{2-} immobilization on the titania surface – chelating bidentate complex formation (Fig. 5, a) with coordination to one metal ion through two oxygens or a bridged bidentate complex formation using bonding through two metal ions (Fig. 5, b) [17]; both complexes belong to C2v point group.

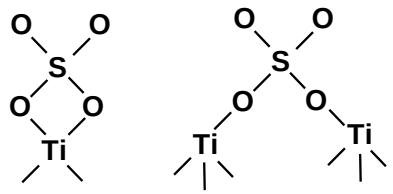

a) *b)*

Fig. 5. Possible surface structures for SO_4^{2-} chemisorptions on titania: (a) chelating bidentate; (b) bridged bidentate.

The correspondence of 1139 cm^{-1} band to bidentate sulfate ion coordinated to Ti^{4+} ions was fixed in [18].

We can suggest the following model of Na_2SO_4 impact on titania nucleation on the stage of olation interaction between primary hydrocomplexes with the taking into account previous work conclusions [19]. Crystal structures of different titania polymorphs – anatase, brookite and rutile – are formed by three-dimensional chains of $[Ti^{4+}O_6]$ octahedrons. Polymorphs differ by mutual position and distortion type of octahedrons. For anatase (space groups I41amd) each octahedron is in contact with 8 neighboring octahedrons (4 sharing edges and 4 sharing vertexes); octahedrons with joint edges align along crystallographic directions [100] and [010] and form a broken double chain perpendicular to the [001] axis. In rutile structure (space group P42mnm) each octahedron is in contact with 10 neighboring

octahedrons (2 sharing edges and 8 sharing vertexes); octahedrons with joint edges align along crystallographic directions [001] (Fig. 6).

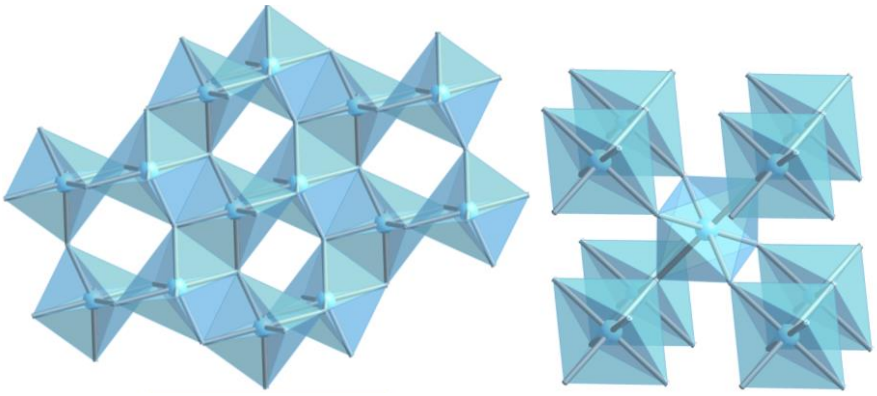

a) *b)*

Fig.6. [TiO_6] coordination octahedrons in the structure of anatase (a) and rutile (b).

The hydrolysis of $TiCl_4$ leads to $[Ti(OH_2)_6]^{4+}$ species formation where Ti^{4+} ions are in the octahedral coordination with the next transformation to $[Ti(OH)_h(OH_2)_{6-h}]^{(4-h)+}$ monomers as a result of deprotonisation. The hydrolysis ratio h is a function of pH and determined by partial charge theory [20]. In these monomers OH^- groups have thermodynamic advantages of the location in the octahedrons equatorial planes, and H_2O molecules primarily occupy the "vertex" position [21]. The hydrolysis products are $[Ti(OH)(OH_2)_5]^{3+}$ and $[Ti(OH)_2(OH_2)_4]^{2+}$ monomers when pH of reaction medium is close to 1. If pH = 3, the $[Ti(OH)_2(OH_2)_4]^{2+}$ and $[Ti(OH)_3(OH_2)_3]^{+}$ complexes coexist in solution. At pH being equal to 4 the hydrolysis leads to the formation of the $[Ti(OH)_3(OH_2)_3]^{+}$ complexes and in the range of pH 6 - 8 the $[Ti(OH)_4(OH_2)_2]^0$ monomers are formed. The possibility of titania polymorph formation is defined by spatial organization of $[Ti(OH)_h(OH_2)_{6-h}]^{(4-h)+}$ primary monomers. $[Ti(OH)_4(OH_2)_2]^0$ monomers in which OH groups occuping octahedrons equatorial planes with H_2O molecules in the vertexes have been formed in neutral or alkaline mediums. Dimers are formed as a result of olation reaction between the two primary monomers for which the coordination octahedrons have a common edge outside the octahedron equatorial plane. After further polycondensation the zigzag-like or spiral chain of $[Ti_n(OH)_{4n}(OH_2)_2]^0$ polyhedrons are formed and the conditions for the anatase phase nucleation are created. The $[Ti_{mn}O_{mn}(OH)_{2mn}(OH_2)_{2m}]^0$ polymer is formed resulting from m linear structures of $[Ti_n(OH)_{4n}(OH_2)_2]^0$ olation interaction. Nucleation of anatase phase is the result of octahedral merger by lateral planes of faces (Fig. 6,a). At the same time the hydronium ions of the reaction medium interact with OH groups in the octahedrons equatorial plane. If the hydronium ions concentration in the reaction medium grows, $[Ti(OH)_h(OH_2)_{6-h}]^{(4-h)+}$ monomers will be formed under $h < 2$ condition. Olation interaction between them leads to the polymer chains formation where monomers are linked by joint edges in octahedrons equatorial planes thus defining the precondition for rutile phase nucleation. The presence of SO_4^{2-} groups in the reaction medium will cause chelating bidentate complexes formation in the octahedrons equatorial planes (Fig.7,a). As a result the olation interaction between monomers with a common edge outside the octahedron equatorial plane is prevailing. In thse conditions polycondensation the zigzag-like or spiral chain of $[Ti_n(OH)_{4n}(OH_2)_2]^0$ polyhedrons are formed and the conditions for the anatase phase nucleation are created (Fig. 7, b).

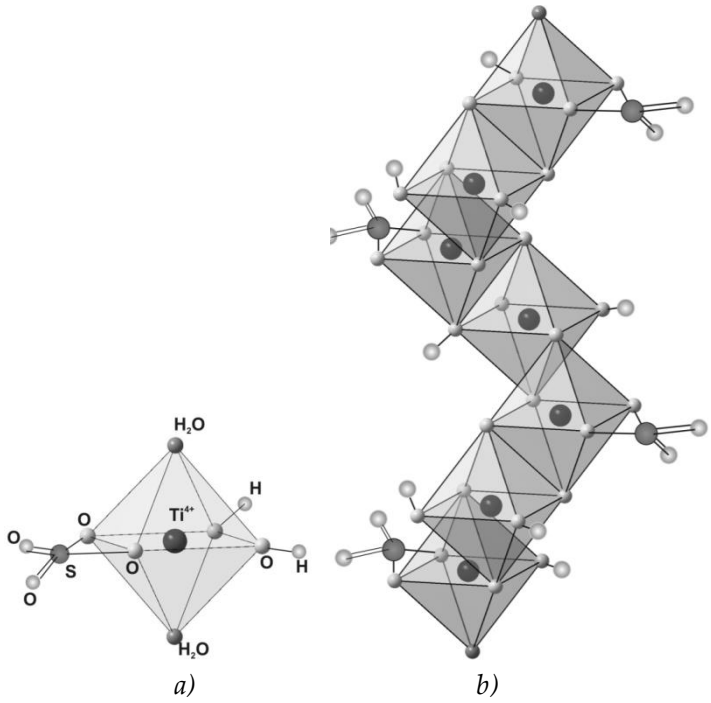

Fig. 7. A scheme of separate $[Ti(OH)_2(OH_2)_2SO_4]^0$ monomer (a) and possible formation of oligomeric chains with anatase phases nucleation (b).

4. CONCLUSIONS

An effect of SO_4^{2-} sulphate anions on the titania nucleation during hydrolysis of titanium tetrachloride was analyzed. It is assumed that the presence SO_4^{2-} leads to chelating bidentate complex formation on the stage of primary monomers $[Ti(OH)_h(OH_2)_{6-h}]^{(4-h)+}$ olation interaction. Sulphate anions bonding to titanium ion through two oxygens in the octahedrons equatorial planes causes the predominant olation between monomers with a common edge outside the octahedron equatorial plane. As a result of polycondensation the zigzag-like of $[Ti_n(OH)_{4n}(OH_2)_2]^0$ polyhedrons are formed and the conditions for the anatase phase nucleation are performed.

REFERENCES

[1] Yamashita H., Harada M., Misaka J., Takeuchi M., Neppolian B., Anpo M. Photocatalytic degradation of organic compounds diluted in water using visible light-responsive metal ion-implanted TiO_2 catalysts: Fe ion-implanted TiO_2. *Catalysis Today*, **84** (3) (2003), 191-196. doi:10.1016/S0920-5861(03)00273-6

[2] Kazuhito H., Irie H., Fujishima A. TiO_2 photocatalysis: a historical overview and future prospects. *Japanese journal of applied physics,* **44** (12) (2005), 8269-8285. doi: 10.1143/JJAP.44.8269

[3] Agrios A.G., Pierre P. State of the art and perspectives on materials and applications of photocatalysis over TiO_2. *Journal of Applied Electrochemistry*, **35** (7) (2005), 655-663. doi:10.1007/s10800-005-1627-6

[4] Bao S.J., Li C.M., Zang J.F., Cui X.Q., Qiao Y., Guo J. New nanostructured TiO_2 for direct electrochemistry and glucose sensor applications. *Advanced Functional Materials,* **18** (4) (2008), 591-599. doi:10.1002/adfm.200700728

[5] O'Regan B., Grfitzeli M. A low-cost, high-efficiency solar cell based on dye-sensitized. *Nature,* **353** (6346) (1991), 737-740. doi:10.1038/353737a0

[6] Xu N., Shi Z., Fan Y., Dong J., Shi J., Hu M.Z.C. Effects of particle size of TiO_2 on photocatalytic degradation of methylene blue in aqueous suspensions. *Industrial & Engineering Chemistry Research*, **38** (2) (1999), 373-379. doi:10.1021/ie980378u

[7] Testino A., Bellobono I.R., Buscaglia V., Canevali C., D'Arienzo M., Polizzi S., Morazzoni F. Optimizing the photocatalytic properties of hydrothermal TiO_2 by the control of phase composition and particle morphology. A systematic approach. *Journal of the American Chemical Society*, **129** (12) (2007), 3564-3575. doi:10.1021/ja067050+

[8] Macwan D.P., Dave P.N., Chaturvedi S. A review on nano-TiO_2 sol–gel type syntheses and its applications. *Journal of Materials Science,* **46** (11) (2011), 3669-3686. doi:10.1007/s10853-011-5378-y

[9] Gupta S.M., Tripathi M. A review on the synthesis of TiO_2 nanoparticles by solution route. *Central European Journal of Chemistry*, **10** (2) (2012), 279-294. doi: 10.2478/s11532-011-0155-y

[10] Yin H., Wada Y., Kitamura T., Kambe S., Murasawa S., Mori H., Yanagida S. Hydrothermal synthesis of nanosized anatase and rutile TiO_2 using amorphous phase TiO_2. *Journal of Materials Chemistry*, **11** (6) (2011), 1694-1703. doi: 10.1039/B008974P

[11] Barnard A.S., Curtiss L.A. Prediction of TiO_2 nanoparticle phase and shape transitions controlled by surface chemistry. *Nano letters*, **5** (7) (2005), 1261-1266. doi: 10.1021/nl050355m

[12] Sivakumar S., Pillai P.K., Mukundan P., Warrier K.G.K. Sol–gel synthesis of nanosized anatase from titanyl sulfate. *Materials letters*, **57** (2) (2002), 330-335. doi:10.1016/S0167-577X(02)00786-3

[13] Gutierrez-Alejandre A., Gonzalez-Cruz M., Trombetta M., Busca G., Ramirez J. Characterization of alumina–titania mixed oxide supports: Part II: Al_2O_3-based supports. *Microporous and mesoporous materials*, **23** (5) (1998), 265-275. doi:10.1016/S1387-1811(98)00121-8

[14] Karuppuchamy S., Jeong J.M. Synthesis of nano-particles of TiO2 by simple aqueous route. *Journal of Oleo Science,* **55** (5) (2006), 263-266. doi: 10.5650/jos.55.263

[15] Djaoued Y., Robichaud J., Bruning R. The effect of polyethylene glycol on the crystallization and phase transitions of nanocrystalline TiO2 thin films. *Materials Science-Poland*, **23** (1) (2005), 15-27.

[16] Yamaguchi T., Jin T., Ishida T., Tanabe K. Structural identification of acid sites of sulfur-promoted solid super acid and construction of its structure on silica support. *Materials chemistry and physics,* **17**(1-2) (1987), 3-19. doi:10.1016/0254-0584(87)90045-9

[17] Raj K.J.A., Viswanathan B. Single-step synthesis and structural study of mesoporous sulfated titania nanopowder by a controlled hydrolysis process. *ACS applied materials & interfaces,* **1** (11) (2009), 2462-2469. doi: 10.1021/am900437u

[18] Sohn J.R., Lee S.H., Cheon P.W., Kim, H.W. Acidic Properties and Catalytic Activity of Titanium Sulfate Supported on TiO_2. *Bulletin-korean chemical society*, **25** (5) (2004), 657-664.

[19] Kotsyubynsky V.O., Myronyuk I.F., Myronyuk L.I., Chelyadyn V.L., Mizilevska M.H., Hrubiak A.B., Tadeush O.K., Nizamutdinov F.M. The effect of pH on the nucleation of titania by hydrolysis of $TiCl_4$. *Materialwissenschaft und werkstofftechnik,* **47** (2-3) (2016), 288–294. doi: 10.1002/mawe.201600491

[20] Henry M., Jolivet J.P., Livage J. *Aqueous chemistry of metal cations: hydrolysis, condensation and complexation.* In: Chemistry, Spectroscopy and Applications of Sol-Gel Glasses, 77, 1992, 153-206. doi: 10.1007/BFb0036968

[21] Kumar S.G., Rao K.K. Polymorphic phase transition among the titania crystal structures using a solution-based approach: from precursor chemistry to nucleation process. *Nanoscale*, **6** (20) (2014), 11574-11632. doi: 10.1039/C4NR01657B

Address: V.O. Kotsyubynsky, I.F. Myronyuk, B.K. Ostafiychuk, A.B. Hrubiak, I.I. Hryhoruk, Vasyl Stefanyk Precarpathian National University, 57, Shevchenko Str., Ivano – Frankivsk, 76018, Ukraine;
V.L. Chelyadyn, Institute of Materials Science, I.M. Frantsevich, 3, Academic Krzhizhanovskii Str., Kyiv, 03680, Ukraine.

E-mail: v_kotsuybynsky@mail.ru; ivan.myroniuk@pu.if.ua; bo@pu.if.ua; ira.hryhoruk@gmail.com; VIChel@tut.by; hrubyak_andrii@ukr.net.

Received: 28.01.2016; **revised:** 12.04.2016.

Коцюбинський В.О., Миронюк І.Ф., Остафійчук Б.К., Челядин В.Л., Груб'як А.Б., Григорук І.І. Вплив сульфат аніонів SO_4^{2-} на процес нуклеації титану. *Журнал Прикарпатського університету імені Василя Стефаника*, **3** (1) (2016), 29–37.

Запропоновано та експериментально апробовано феноменологічну модель впливу сульфат аніонів SO_4^{2-} на нуклеацію титану в процесі гідролізу тетрахлориду титану. Сульфат аніони із первинних комплексів $[Ti(OH)_h(OH_2)_{6-h}]^{(4-h)+}$ утворюють бідентантні хелатні комплекси, впливають на процес протікання оляційних взаємодій та формування зародків фази анатазу.

Ключові слова: гідроліз, поліконденсація, енуклеація, анатаз, сульфат аніони.

Journal of Vasyl Stefanyk Precarpathian National University
http://jpnu.pu.if.ua
Vol. 3, No. 1 (2016), 38-45

UDC 541.1, 5367, 621.794
PACS numbers: 61.05.C, 75.47.Lx, 75.50.Tt, 75.50.Vv, 81.05.Rm, 81.16.Be
doi: 10.15330/jpnu.3.1.38-45

THE EFFECT OF PRECURSORS CONCENTRATION ON THE STRUCTURE AND MICROMAGNETIC PROPERTIES OF ULTRAFINE IRON OXIDES OBTAINED BY SOL-GEL ROUTE

V.O. KOTSYUBYNSKY, V.V. MOKLYAK, A.B. HRUBIAK, L.V. MOHNATSKA,

M.I. GASYUK

Abstract. Nanodispersed composite materials γ-Fe_2O_3/α-Fe_2O_3 were obtained by thermal decomposition of iron citrate xerogel hydrate synthesized by iron nitrate and citrate acid solutions with different colloidal solutions of $Fe(NO_3)_3 \cdot 9H_2O$ and $C_6H_8O_7 \cdot H_2O$ for different molar ratio between precursors. The influence of the precursors molar concentration and calcination temperature on the material phase composition, crystalline and magnetic microstructure, surface condition was studied. Methods of X-ray diffraction, Mössbauer spectroscopy, electron microscopy and IR - spectroscopy were used.
Keywords: iron citrate, sol-gel, molar ratio, nanoscale, magnetic microstructure, superparamagnetic.

1. INTRODUCTION

Ultrafine and nanostructured iron oxides are applicated as materials for spintronic [1], catalysts [2], drug delivery [3], MRI contrasts [4] and Photoanode for Water Splitting [5]. These materials are perspective for photocatalytic treatment of environmental pollutants [6], the components of magnetic fluids [7] and electrode material for lithium power sources [8]. The material efficiency in a particular area is determined by the phase composition, the characteristics of the crystal and magnetic microstructure and surface morphology. For example, ultrafine γ-Fe_2O_3 are efficient, green, heterogeneous and reusable catalyst for many multi-step organic syntheses at ambient temperature for their greater reactivity and high surface area with mesoporous structure cause the significant improvement of reaction efficiency [9]. Therefore development and improvement of methods for the nanostructured iron oxides synthesis can open the possibilities of functional materials obtaining with controlled and predetermined properties adapted for specific sphere of the use. Iron oxides nanoparticles have been synthesized by different methods [10] – from chemical precipitation and sol-gel techniques to electrochemical and mechanochemical methods. The combination of some methods is promising variant. The determination of synthesis conditions effects on the material phase composition and morphology is an important and hot topic.

The aim of this paper is an investigation the influence of precursors molar contents on the phase composition and crystal and magnetic microstructures ultrafine iron oxides obtained by thermal decomposition of sol-gel obtained iron citrate xerogel hydrate process.

2. MATERIALS AND METHODS

Iron oxides were synthesized by sol-gel route: slow drying (60°C) on the air of colloidal solutions of $Fe(NO_3)_3 \cdot 9H_2O$ and $C_6H_8O_7 \cdot H_2O$ for different molar ratio between precursors (samples obtained at 1:0.5, 1:1, 1:4 and 1:12 ratio were marked S1, S2 S3 and S4, respectively). Sedimentated during 12-15 days iron citrate hydrate was dried out in the air at 50-60°C. Obtained gels were annealed at 200, 300 and 400 C during 1 hour.

Systems of samples were investigated by X-ray diffractometry, Mossbauer spectroscopy, infra-red optical spectroscopy and scanning electron microscopy.

Diffraction patterns were obtained with diffractometer DRON-4-07 (Cu K_α radiation). Bragg-Brentano geometry type and a Ni K_β - filter were used. Quantitative analysis was realized using full pattern Rietveld refinement procedure using FullFrof Suite Program. XRD measurements were collected in a 2θ range of 16–65°.

Scanning electron microscopy images were obtained using an microscope JSM- 6490 LV JEOL, at a 30 kV.

The Mössbauer spectra were measured with a MS-1104Em spectrometer using a 57Co γ-ray source and calibrated at room temperature with α-Fe as a standard (linewidth 0.29 mm/s). The isomer shifts (δ) are relative to Fe metal. The model fitting and hyperfine field distributions recovering was performed using Mosswin 3.0 software.

Infrared spectra were recorded at Thermo-Nicolet Nexus 670 FT-IR spectrometer in the region of 4000 – 400 cm^{-1}. The mixture TiO_2 / KBr after vibrating milling was pressed into pellets and measured in the transmission mode.

3. RESULTS AND DISCUSSION

Accordingly to XRD analysis data (Fig. 1), S1, S2 and S4 samples obtained by the annealing of initial xerogels at 200°C are the mixture of γ-Fe_2O_3 and α-Fe_2O_3 phases. Meantime S3 sample (molar ratio $Fe(NO_3)_3 \cdot 9H_2O$: $C_6H_8O_7 \cdot H_2O$ = 1:4) was unexpectedly X-ray amorphous.

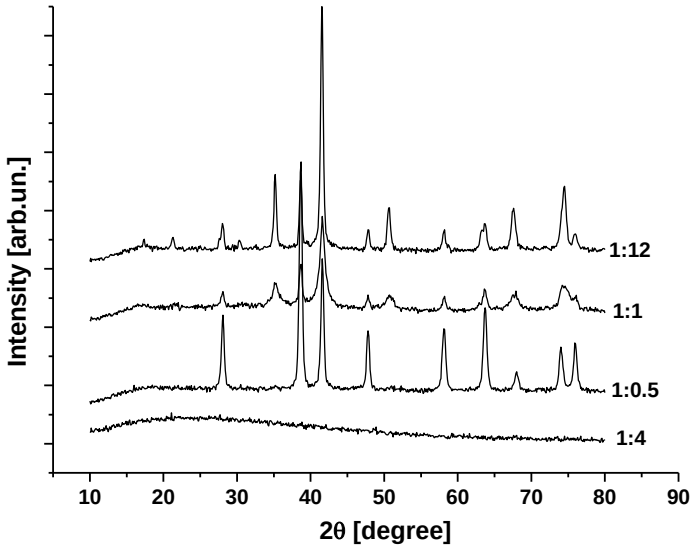

Fig. 1. XRD patterns of materials obtained by the annealing of initial xerogels at 200°C.

The content of γ-Fe_2O_3 phase nonlinear changes with the $C_6H_8O_7 \cdot H_2O$ concentration increasing (9±1, 47±3 and 43±2 mass % for S1, S2 and S4 samples, respectively). This result is correlated with changes of γ-Fe_2O_3 X-ray scattering coherent blocks average sizes 16, 6 and 14 nm for S1, S2 and S4 samples. The enlarging of annealing temperature to 300°C leads to crystallization of S3 sample (α-Fe_2O_3 phase content became 88 mass. %). Phase composition of S2 sample didn't change after calcination at 300°C when for S1 and S4 α-Fe_2O_3 content has been grown to 86 and 93 mass.%. After calcinations at 400°C only S2 sample contains γ-Fe_2O_3 (about 7 mass.%).

Accordingly to Fourier transform infrared spectroscopy (Fig. 2) all sample systems contained molecular non-dissociated water –a broad absorption band between 3200 and 3400 cm^{-1} corresponds to vibrational modes of ν (H – O) [11]. There were also presence bound OH groups (bands at 1618 cm^{-1} [12] but it's content is relatively low.

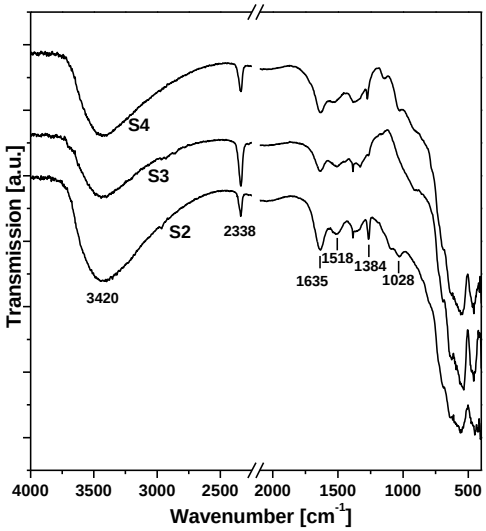

Fig. 2. FTIR spectra of iron oxides obtained by iniatiial xerogels annealing at 300°C.

The sharp band at 2338 cm^{-1} for all samples is associated with the vibrational modes of ν (C – O) in absorbed CO_2 [13]. A band with a maximum at 1384 cm^{-1} corresponds to deformation vibration COO–Fe^{3+} bonds [14]. Bands around 535–550 cm^{-1} are associated with O–Fe bond [15], absorption maximum at 453 $см^{-1}$ linled to vibrational modes octahedral coordinated Fe^{3+}–OH. The band broadening in Fourier transform infrared spectra is characteristic of structurally disordered materials. As a result the presents of amorphous γ- FeOOH phase in all samples is very possible.

Additional information about synthesized materials of phase composition and magnetic properties was obtained by mossbauer spectroscopy (Fig. 3).

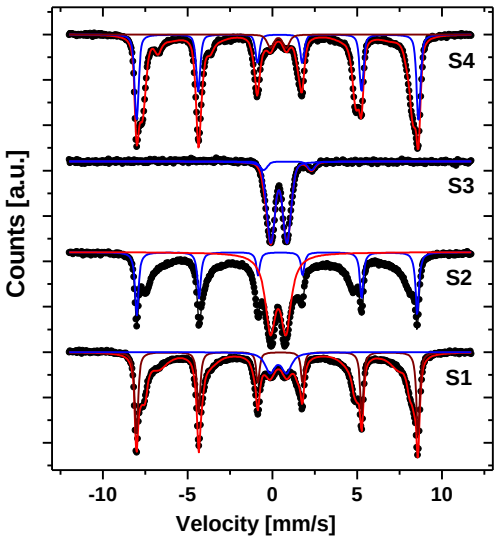

Fig. 3. Mossbauer spectra (room temperature) of iron oxides obtained by iniatial xerogels annealing at 200°C.

Mossbauer spectra for S1, S2 and S4 materials after annealing at 200°C are the superposition of two different parts: six-line pattern components corresponds to a magnetically ordered fraction of the sample and a doublet components caused by sizes effects and superparamagnetism phenomena. Sextet component which respond to the resonance absorption by ^{57}Fe nucleus in the α-Fe_2O_3 particles are clear separated due specific values of quadrupole splitting (Δ = -0.19 – -0.21mm/s) and hyperfine magnetic field more than 51 T. Comparatively low line width for these components indicates the relatively good crystallinity of this phase. Meantime sextets corresponding to γ-Fe_2O_3 are broadered so the γ-Fe_2O_3 phase consist of separate nanoparticles. For this case doublet component is the result of some particles transition to superparamegnetic state. For of γ-Fe_2O_3 nanoparticles with the diameter <10 nm monodomain state is energy favorable with temperature induced fluctuation of magnetic moments. This fluctuations cause the spectral components broadening and disappearance of magnetic hyperfine structure at a certain value of material magnetic anisotropy which determines the relaxation time τ_r of a particle magnetic moment. Relaxation time is calculated as $\tau_r = \tau_0 \exp\left(\frac{KV}{kT}\right)$, where $\tau_0 \approx 10^{-9}$-10^{-10} s, V– particle volume, K– constant of anisotropy, T– temperature. So doublet components correspond to γ-quantum resonance absorption in the γ-Fe_2O_3 particles. Accordingly to this conclusion we can refine the information about S1 sample phase composition – actually content of γ-Fe_2O_3 is about 81 %. Mismatch to XRD data is caused by nanoscale sizes of most γ-Fe_2O_3 particles which formed mesoporous 3D-grid. Paramagnetic parts of the spectra contain two components which have close values of isomeric shift about δ=0,34–0,36 mm/s and different values of quadrupole splitting Δ, which are determined by neighbour encirclement of Fe^{57} nuclei. The constant of magnetic anisotropy for the particles of γ-Fe_2O_3 is $1.2 \cdot 10^6$ J/m^3 [16] so we can estimate particles size. Accordingly this calculation average particles size S3 sample is less than about 5 nm at room temperature for superparamagnetic state implementation.

Component with Δ=0,88-0.90 mm/c is respond to resonance absorption in nanoparticles γ-Fe_2O_3 with non-zero values of electric field gradient on Fe^{57} nuclei and is explained by deformation effects in crystal lattice of maghemite. Zero values of Δ for second doublet component are determined by cubic symmetry of particle structure, which are in non-stressed state. We can suppose that the presence two types of Fe^{57} surroundings respond to the resonance absorption by nucleus in the superficial and inner regions of separate particles (grid nodes). That composition is typical for S1, S2 and S4 materials annealed at 200°C –γ-Fe_2O_3 phase is dominant for all cases. For S3 sample no any magnetically ordered structure hasn't been detected. Moreover, presence Fe^{2+} ions (10%) was observed.

The S2 magnetic microstructure transformation with annealing at 250, 300 and 400°C was studied by function of hyperfime field distributions recovering methods which allows obtain additional information magnetic ordering changes. The calculated distributions are non monotonous (Fig.4) and are characterized by some maxima in low field region (22-33T), region of magnetic hyperfine interaction probability smooth growth (35-45T) and major maxima (48±3 T). Optimal fitting results for samples obtained after sinering at 250°C and 300°C became possible only in case of wide doublet component addition with close to zero quadrupole splitting (Fig. 4, a, b). This component represents an intermediate stage between magnetically ordered and superparamagnetic states of a particle in the case of strong dipole-dipole interaction [17]. This component is a result of resonance absorption by the ^{57}Fe nucleu, for which the hyperfine field has the value between zero and saturation level. Thermal fluctuation of magnetic moment of particles takes place but the "temporary freezing" is possible. At the same time, the transition to superparamagnetic state is not observed although the energy of thermal fluctuations exceeds the anisotropy energy.

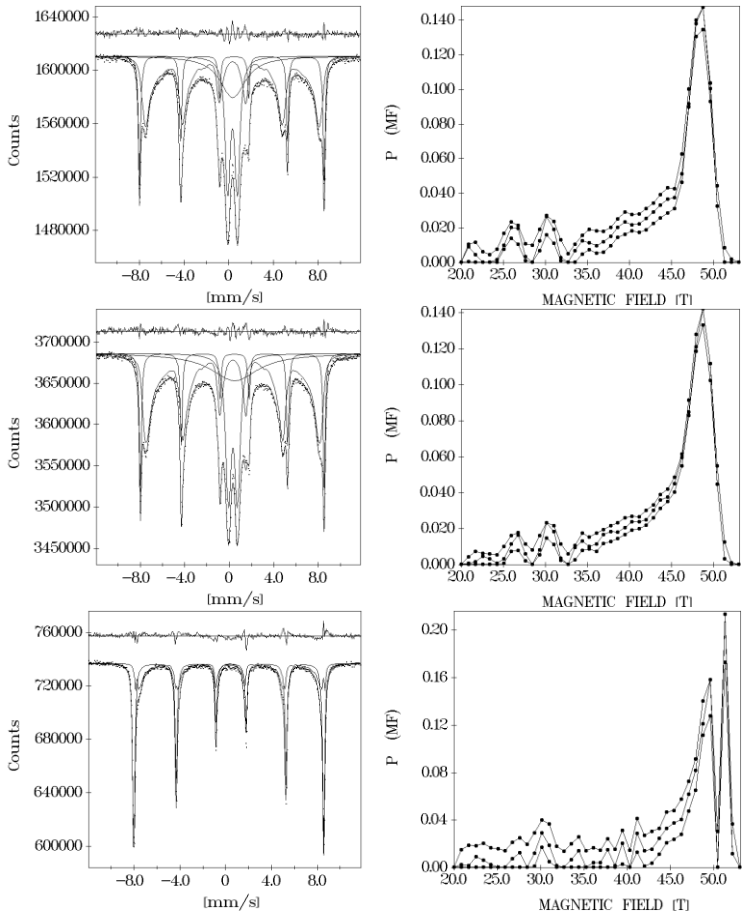

Fig. 4. Mossbauer spectra of S2 sample after annealing at 250 (a), 300 (b) and 400°C; additional plots – recovered functions of hyperfine fields on ^{57}Fe nucleus probabilities distributions (central line) and confidential intervals of computations (zones confine upper and confine lines).

General peculiarities of samples microstructure which were detected by XRD and Mossbauer methods are reflected on the scanning electron microscopy data (Fig. 5). Materials of all series are characterized by porous structure as a result of evaporation of metal-organic precursor decomposition products. For S1 and S4 samples sizes of separate particles which formed the agglomerates are relatively larger comparatively to S2 and S3 samples (especially S3). At the same time the density of S2 and S3 sample is higher.

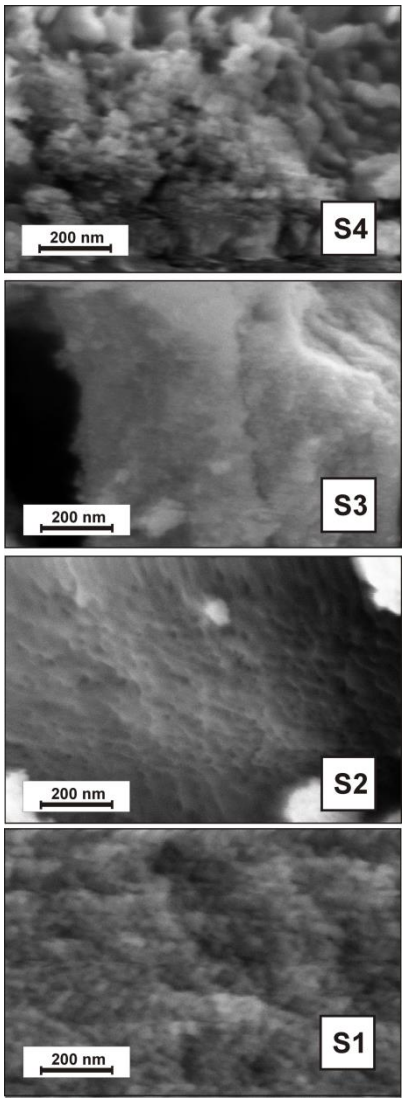

Fig.5. SEM images of γ-Fe2O samples obtained at different sintering temperatures.

4. CONCLUSIONS

To sum up the experimental data we can allow that the molar ratio between $Fe(NO_3)_3 \cdot 9H_2O$ and $C_6H_8O_7 \cdot H_2O$ precursors is the determination factors of the phase composition, magnetic microstructure and morphological peculiarities of the nanodispersed composite γ-Fe_2O_3 / α-Fe_2O_3 obtained by the thermal decomposition of the synthesized iron citrate hydrate. It was determined that the material syntesized at $Fe(NO_3)_3 \cdot 9H_2O$ and $C_6H_8O_7 \cdot H_2O$ precursors molar ratio equal 1:4 consist of nanoparticles iron oxides in superparamagnetic state with the <5 nm sizes with the maximal content of γ-Fe_2O_3 and minimal macroporous precence. At the same time all composites are characterized by porous structure as a result of organic components evaporation. The investigations of the magnetic microstructure thermal-induced transformation for obtained composites have shown that the phase transition γ-$Fe_2O_3 \rightarrow \alpha$-$Fe_2O_3$ practically finished after sintering at 400°C. Interparticle dipoledipole magnetic interaction is observed be Mossbauer spectroscopy method. Obtained results are interesting for the approach formulation of magnetic nanomaterials controlled obtaining.

REFERENCES

[1] Cheng W., He J., Yao T., Sun Z., Jiang Y., Liu Q., Yan W. Half-Unit-Cell α-Fe_2O_3 Semiconductor Nanosheets with Intrinsic and Robust Ferromagnetism. *Journal of the American Chemical Society*, **136** (29) (2014), 10393-10398. doi: 10.1021/ja504088n

[2] Shi F., Tse M.K., Pohl M.M., Brückner A., Zhang S., Beller M. Tuning Catalytic Activity between Homogeneous and Heterogeneous Catalysis: Improved Activity and Selectivity of Free Nano-Fe_2O_3 in Selective Oxidations. *Angewandte Chemie International Edition,* **46** (46) (2007), 8866-8868. doi: 10.1002/anie.200703418

[3] Cao S.W., Zhu Y.J., Ma M.Y., Li L., Zhang L. Hierarchically nanostructured magnetic hollow spheres of Fe_3O_4 and γ-Fe_2O_3: preparation and potential application in drug delivery. *The Journal of Physical Chemistry C.,* **112** (6) (2008), 1851-1856. doi: 10.1021/jp077468+

[4] Arsalani N., Fattahi H., Nazarpoor M. Synthesis and characterization of PVP-functionalized superparamagnetic Fe_3O_4 nanoparticles as an MRI contrast agent. *Express Polym Lett.*, **4** (6) (2010), 329-38. doi: 10.3144/expresspolymlett.2010.42

[5] Cesar I., Kay A., Gonzalez Martinez J.A., Grätzel M. Translucent thin film Fe_2O_3 photoanodes for efficient water splitting by sunlight: nanostructure-directing effect of Si-doping. *Journal of the American Chemical Society,* **128** (14) (2006), 4582-4583. doi: 10.1021/ja060292p

[6] Cao S.W., Zhu Y.J. Hierarchically nanostructured α-Fe_2O_3 hollow spheres: preparation, growth mechanism, photocatalytic property, and application in water treatment. *The Journal of Physical Chemistry C.,* **12** (16) (2008), 6253-6257. doi: 10.1021/jp8000465

[7] Oliveira F.C., Rossi L.M., Jardim R.F., Rubim J.C. Magnetic fluids based on γ-Fe_2O_3 and $CoFe_2O_4$ nanoparticles dispersed in ionic liquids. *The Journal of Physical Chemistry C.*, **113** (20) (2009), 8566-8572. doi: 10.1021/jp810501m

[8] Arico A.S., Bruce P., Scrosati B., Tarascon J.M., Van Schalkwijk W. Nanostructured materials for advanced energy conversion and storage devices. *Nature materials,* **4** (5) (2005), 366-377. doi: 10.1038/nmat1368

[9] Medisetti V., Parimi U., Anagani R.B., Satyanarayana K.V. Nano-γ-Fe_2O_3: Efficient, Reusable and Green Catalyst for N-tert-Butoxycarbonylation of Amines in Water. *Green and Sustainable Chemistry*, **4** (2) (2014), 95-101. doi: 10.4236/gsc.2014.42014

[10] Mohapatra M., Anand S. Synthesis and applications of nano-structured iron oxides/hydroxides–a review. *International Journal of Engineering, Science and Technology,* **2** (8) (2010), 127-146. doi: 10.4314/ijest.v2i8.63846

[11] Crisan M., Jitianu A., Crisan D., Balasoiu M., Dragan N., Zaharescu M. Sol-gel monocomponent nano-sized oxide powders. *Journal of Optoelectronics and Advanced Materials,* **2** (4) (2000), 339-344. doi: 10.1023/A:1008735127136

[12] Balachandran K., Venckatesh R., Sivaraj R. Synthesis of nano TiO_2-SiO_2 composite using sol–gel method: effect on size, surface morphology and thermal stability. *International Nano Letters*, **2** (8) (2010), 3695-3700. doi: 10.1186/2228-5326-2-15

[13] Duncan M. *Cluster Materials*. J. I Press Limited, N.Y, 1998, 402.

[14] El-Akkad T.M. Effect of thermal dehydration on surface characteristics of titania gel. *Thermochimica Acta,* **37** (3) (1980), 269-277. doi: 10.1016/0040-6031(80)87155-3

[15] Guo L., Wu Z., Liu T., Yang S. The effect of surface modification on the microstructure and properties of γ-Fe_2O_3 nanoparticles. *Physica E: Low-dimensional Systems and Nanostructures,* **8** (2) (2000), 199-203. doi: 10.1016/S1386-9477(00)00140-5

[16] Coey J.M.D., Khalafalla D. Superparamagnetic γ-Fe_2O_3. *Physica status solidi (a)*, **11** (1) (1972), 229-241. doi: 10.1002/pssa.2210110125

[17] Kotsyubynsky V., Moklyak V., Hrubiak A. Synthesis and Mossbauer studies of mesoporous γ-Fe_2O_3. *Materials Science-Poland,* **32** (3) (2014), 481-486. doi: 10.2478/s13536-014-0202-4

Address: V.O. Kotsyubynsky, A.B. Hrubiak, L.V. Mohnatska, M.I. Gasyuk, Vasyl Stefanyk Precarpathian National University, 57, Shevchenko Str., Ivano – Frankivsk, 76018, Ukraine;
V.V. Moklyak, Institute of Metal Physics, National Academy of Science, 36 Ac. Vernadsky Boulevard, Kyiv, 03680, Ukraine.
E-mail: v_kotsuybynsky@mail.ru; hrubyak_andrii@ukr.net; mvvmcv@gmail.com; knooopka@ukr.net; gasyukim@gmail.com.
Received: 08.02.2016; **revised:** 28.04.2016.

Коцюбинський В.О., Мокляк В.В., Груб'як А.Б., Мохнацька Л.В., Гасюк М.І. Вплив концентрації прекурсорів на структурні та магнітні властивості ультра дисперсного оксиду заліза отриманого цитратним золь-гель методом. *Журнал Прикарпатського університету імені Василя Стефаника*, **3** (1) (2016), 38–45.

Нанодисперсні композитні матеріали γ-Fe_2O_3/α-Fe_2O_3 синтезовано термічним розкладанням ксерогелів гідрату цитрату заліза сформованих в результаті висушування золів цитрату заліза, які отримували шляхом змішування розчинів нітрату заліза та лимонної кислоти у різних співвідношеннях. Досліджено вплив молярного співвідношення $Fe(NO_3)_3 \cdot 9H_2O$ та $C_6H_8O_7 \cdot H_2O$, а також температури відпалювання ксерогелю на фазовий склад, кристалічну та магнітну структури та стан поверхні композитних матеріалів. Застосовувалися методи рентгеноструктурного аналізу, месбауерівської спектроскопії, електронної мікроскопії та оптичної спектроскопії у інфрачервоному діапазоні.

Ключові слова: цитрат заліза, золь-гель, молярне співвідношення, нанорозмірні, магнітна мікроструктура, суперпарамагнетизм.

Journal of Vasyl Stefanyk Precarpathian National University
http://jpnu.pu.if.ua
Vol. 3, No. 1 (2016), 46-55

UDC 544.643.076.2, 661.666.1
PACS numbers: 81.25.Rm, 81.05.Uw, 82.45.Fk
doi: 10.15330/jpnu.3.1.46-55

MORPHOLOGY, CONDUCTIVITY AND ELECTROCHEMICAL PROPERTIES OF HYDROTHERMAL CARBONIZED POROUS CARBON MATERIALS

N.I. NAGIRNA, V.I. MANDZYUK

Abstract. The paper studies the morphology, conductivity and electrochemical properties of carbon materials, obtained from raw plant materials at different condition of hydrothermal carbonization, using low-temperature porometry, impedance spectroscopy and galvanostatic charge/discharge. It is set, that in porous structure of carbon materials micropores are dominant; when carbonization temperature increased the specific surface and pore volume decrease more than 10 times. The temperature growth results in increasing the electrical conductivity of the carbon material more than 6 orders. It is found, that the maximal value of specific capacity (1138 mA·h/g) has an electrochemical system based on porous carbon carbonized at 1023 K.

Keywords: porous carbon material, morphology, conductivity, lithium power source.

1. INTRODUCTION

As know [1], current creative process in lithium power sources (LPS) is a result of lithium ions insertion (intercalation) into cathode material. Energy potential of current sources is determined by possibility of cathode absorb reversibly a certain number of "guest" ions, which is characterized by insertion degree x. To increase significantly the amount of absorption centers and increase the specific energy parameters of the power sources the maximum possible dispersion of cathode material in order to increase the specific surface of the material is used. When used as a cathode porous carbon material (PCM) the value of its specific surface area can be effectively controlled by selecting of carbonization temperature [2, 3]. The question is, how carbonization temperature effect on the electrochemical processes in the LPS based on PCMs and its specific energy characteristics, and is the subject of this paper.

2. EXPERIMENTAL

Mechanically crushed apricot pits, placed in an autoclave filled with distilled water, were the initial material for carbonization. Tightly sealed autoclave is placed in the furnace, where PCM was obtained at a certain temperature. Hydrothermal carbonization of the material was carried out in the temperature range T = 873 – 1373 K (temperature change every 50 K) at a pressure of water vapor in the

range (6 - 8)·10^5 Pa. The regimes of hydrothermal carbonization of feedstock are described in detail in [4]. After the heat treatment material obtained has undergone mechanical milling twice.

The textural characteristics of samples were analyzed on the basis of low-temperature (77.4 K) nitrogen adsorption-desorption isotherms recorded using a Quantachrome Autosorb Nova 2200c adsorption analyzer. Before measurements, the samples were heated at 180°C for 24 h. Quantitative analysis of adsorption/desorption isotherms was held according to the standard BET- [5] and t- [6] methods. This made it possible to calculate the parameters of porous structure of carbon materials: surface area (S_{sp}), micropore surface (S_{micro}), the external pore surface (S_{ext}), micropore volume (V_{micro}). The total pore volume V was evaluated from the nitrogen adsorption at $p/p_0 \approx 0.99$, where p and p_0 denote the equilibrium and saturation pressure of nitrogen at 77.4 K, respectively. The pore size distribution (PSD) was calculated using nonlocal density functional theory method [7] using equilibrium model with slit pores.

To study the electrically parameters of PCMs used the capacitor system consisted of two copper electrodes and a sample in between. Nyquist diagrams $Z' = f(Z'')$, where Z' and Z'' – real and imaginary parts of complex resistance of system, was carried out using a Autolab FRA-2 (Frequency Response Analyzer) at 10^{-2} – 10^5 Hz and voltage amplitude of 10 mV. The specific resistance, conductivity and frequency dependence of the electrical parameters were calculated taking into account the geometric parameters of samples according to equation

$$\rho^* = \rho' - j\rho'',$$

where $\rho' = Z'A/d$ and $\rho'' = Z''A/d$, and A, d – electrode surface area and sample thickness respectively. Complex conductivity was determined from the ratio

$$\sigma^* = 1/\rho^* = \sigma' + j\sigma'',$$

where $\sigma' = \rho'/M$, $\sigma'' = \rho''/M$, $M = \left|Z^*\right|^2 (A/d)^2$, and total conductivity $\sigma^* = \sqrt{(\sigma')^2 + (\sigma'')^2}$ [8].

The cathode was made from a mixture of PCM and a binder component (teflon) at a ratio of 96%: 4% respectively. These components mechanically mixed to obtain a homogeneous mixture, then acetone was added to achieve a paste-like consistency and the resulting slurry was applied to the nickel mesh size of 5×5 mm^2 and pressed. The anode from a lithium foil was pressed at nickel net. After drying electrodes impregnate into the electrolyte solution and element was sealed. 1M solution of lithium tetrafluoborate ($LiBF_4$) in γ-butyrolactone was used as an electrolyte. All operations for LPS manufacturing was carried out in a glove box with dry atmosphere. The equilibrium electrode potential of explored materials regarding lithium reference electrode was 3.2-3.4 V. Electrochemical insertion of lithium ions into PCM carried out in galvanostatic mode at a current density of 40 μA/cm^2 (2 mA/g).

Specific discharge capacity C_{sp} of LPS was calculate as

$$C_{sp} = I\,t/m,$$

where I – discharge current, t – discharge time, m – mass of PCM.

Specific energy E_{sp} of LPS was determined as area under discharge curve $U = f(C_{sp})$.

3. Results and Discussion

The primary step in the study of porous structure of any material is to obtain adsorption/desorption isotherms on which you can make further calculations. Typically, sorption isotherm is dependence of quantity of gas adsorbed by material on relative pressure p/p_0 at constant temperature.

Isotherms of nitrogen adsorption/desorption for PCMs (Fig. 1), obtained at different temperatures carbonization, is similar quality. However, a more detailed analysis, based on a quantitative comparison of the magnitude of adsorbed nitrogen and form of adsorption curve, gives reason to assert that for PCMs received at carbonization temperatures of 873-1173 K adsorption isotherm can be classified as I type according to the IUPAC classification [9], which is typical for microporous solids

having a relatively small external surface (activated carbons, zeolites, organic metal grating). The adsorption isotherm for PCMs, obtained at higher temperatures, can already be attributed to the II type that is characteristic of non-porous adsorbents. This difference is due to processes that occur during the carbonization of feedstock. In particular, temperature range, which corresponds to a change of adsorption isotherm type, is in the region where the transition from polycondensation of aromatic molecules to the stage of first carbonization take place, during which begins the formation of carbon layers and the formation of primary graphite nuclei. The removing of volatile components at the stages of cyclization, aromatization and polycondensation leads to the formation of developed microporous structure with small external surface in the raw material. The reduction of micropores number, their merging with transition in mesopores and the formation of microparticles of non-porous PCM are possible at higher temperatures. It should be noted that all isotherms are characterized by a mismatch of adsorption and desorption branches, especially in the area of low pressure, called low pressure hysteresis. This can be due to the presence of long and narrow pores with narrow necks close in size to the nitrogen molecules [9].

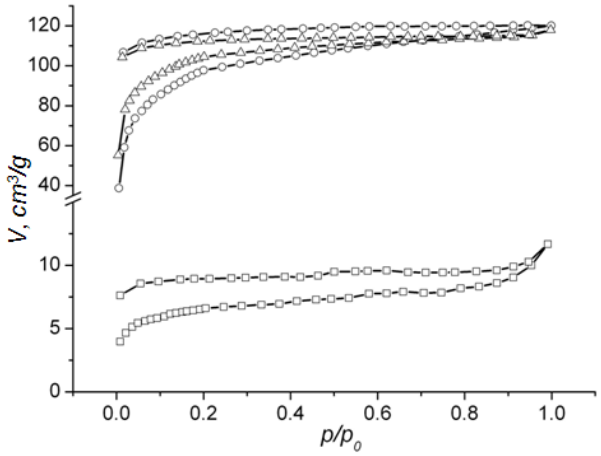

Fig. 1. Nitrogen sorption isotherms for PCMs: 873 K (-○-), 1073 K (-Δ-), 1323 K (-□-).

Quantitative analysis of sorption isotherms shows that PCMs obtained at carbonization temperatures of 873-1173 K, characterized by high specific surface area, the value of which gradually decrease with increasing temperature (Tab. 1). The specific surface area decreases more than an order at the temperatures of carbon layers formation (first carbonization). The data of Tab. 1 confirm the assumption of the mesopore existence in PCM, in addition to micropores; the number one, so other decreases with increasing temperature. Somewhat different is the situation regarding the ratio of micro- and mesopores surface. For samples obtained in the temperature range 923-1123 K, the proportion of the surface occupied by micropores is greater than 85% of the surface, whereas this value is 60% when the temperature increases. It is clear, that when carbonization temperature is increased the parameters that characterize the pore volume of PCM will be altered so. In particular, there is a tendency to decrease of the total volume of pores V (Tab. 1). The micropore volume V_{micro} is changed similarly. Having the last two parameters, you can determine the amount of meso- and macropores. However, the absolute values are less informative; more interesting is the change in the micropore fraction in the total pores at temperature increasing. As follows from Tab. 1, in the temperature range of 873-1123 K fraction of micropores is from 64 to 88 %, while at higher temperatures their content sharply reduced and does not exceed 50 %. This behavior is similar to that described above change of the proportion of surface micropores S_{micro} relation to the total surface S_{sp}.

Carbonization temperature T, K	S_{sp}, м²/г	S_{micro}, m²/g	S_{ext}, m²/g	V, cm³/g	V_{micro}, cm³/g
873	357	282	75	0,186	0,119
923	407	354	53	0,193	0,149
973	374	338	36	0,174	0,143
1023	343	292	51	0,166	0,123
1073	382	338	44	0,182	0,143
1123	331	314	17	0,148	0,131
1173	265	185	80	0,151	0,078
1223	168	96	72	0,116	0,040
1273	45	34	11	0,031	0,014
1323	24	18	6	0,018	0,008
1373	12	9	3	0,011	0,005

Tab. 1. Structure-sorption parameters of PCMs.

PSD (Fig. 2) indicates that the in explored samples micropores dominate, which is in the range of d = 1.25-1.65 nm; the amount of adsorbed nitrogen remains unchanged to a temperature of 1173 K. Above this temperature gas volume decreases sharply and it content decreases in 10 times at T = 1323 K.

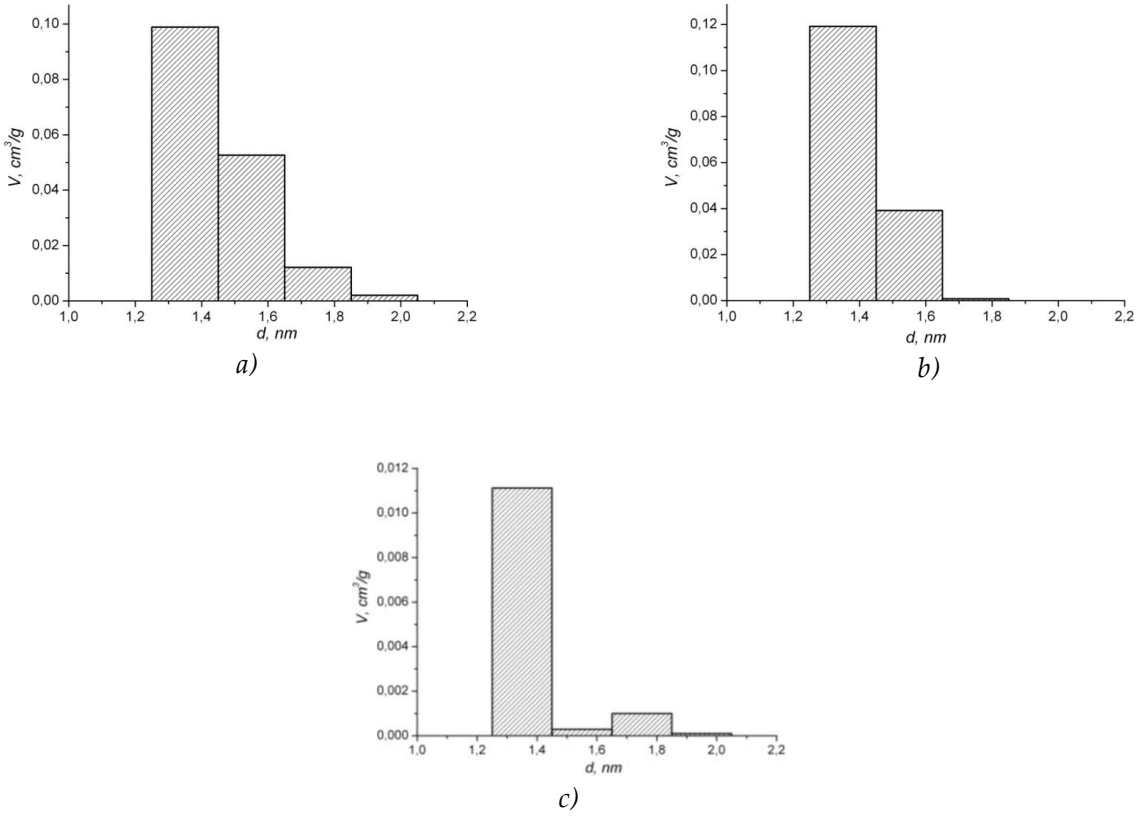

Fig. 2. Pore size distribution for PCMs carbonized at 873 (a), 1073 (b), and 1323 K (c).

As the main factors that affect the electrical properties of the PCMs is thermal treatment of feedstock, which detects the presence on the surface of different functional groups, chemical composition and morphology of the material, and the pressure applied to the packing of particles, so it is necessary to establish relation between conductivity of PCMs and temperature carbonization of feedstock.

As follows from the results of the research, increasing of PCM carbonization temperature greatly changes the character of the complex impedance system (Fig. 3), thus reflecting the possible changes in

the electrical conductivity of carbon materials. These are the real and imaginary reduce the system resistance more than 4-6 order, and the general view of hodograph curve.

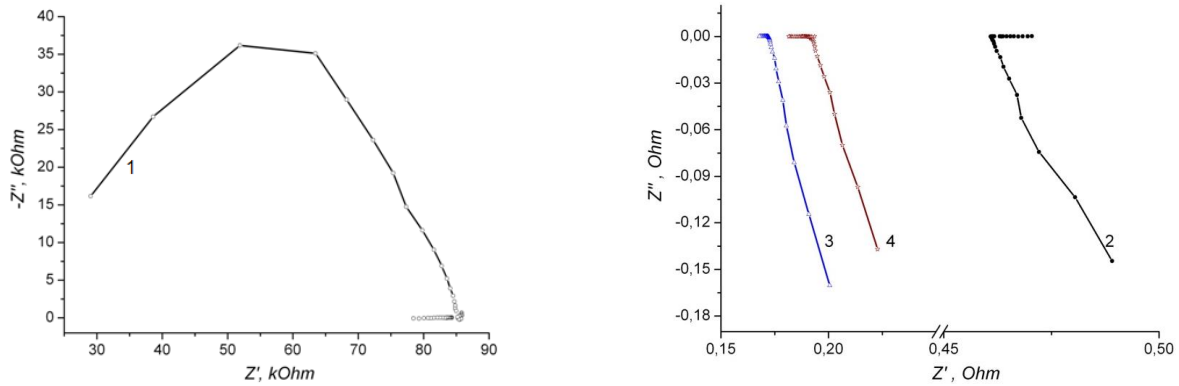

Fig. 3. Nyquist diagrams for PCMs, obtained at 923 (1), 1073 (2), 1223 (3) and 1373 K (4).

A characteristic feature of the frequency behavior of resistances with temperature increasing is the transition of imaginary resistance values Z'' from negative half plane in a positive one, indicating the dominance of inductive behavior over capacitive one at frequencies $f = 10^5$-400 Hz. The values of real resistance Z' for PCMs, obtained at temperatures above 923 K, are independent on frequency. Based on the ratios described above the values of real, imaginary and complete conductivity of PCMs and their dependence on the frequency were calculated (Fig. 4). Because the value of the real part of the electrical conductivity (Fig. 4, a) is approximately in two orders greater than the imaginary conductivity (Fig. 4, b), the contribution of the latter in full conductance (Fig. 4, c) of PCM is insignificant. As follows from the data, values σ', σ'' and σ^* are independent on frequency in the frequency range $f = 10^{-2}$-10^3 Hz for all materials. In the range of low frequencies ($f < 10^{-2}$ Hz) for PCMs ($T > 1123$ K) is a slight increase in value σ' and σ^* accordingly.

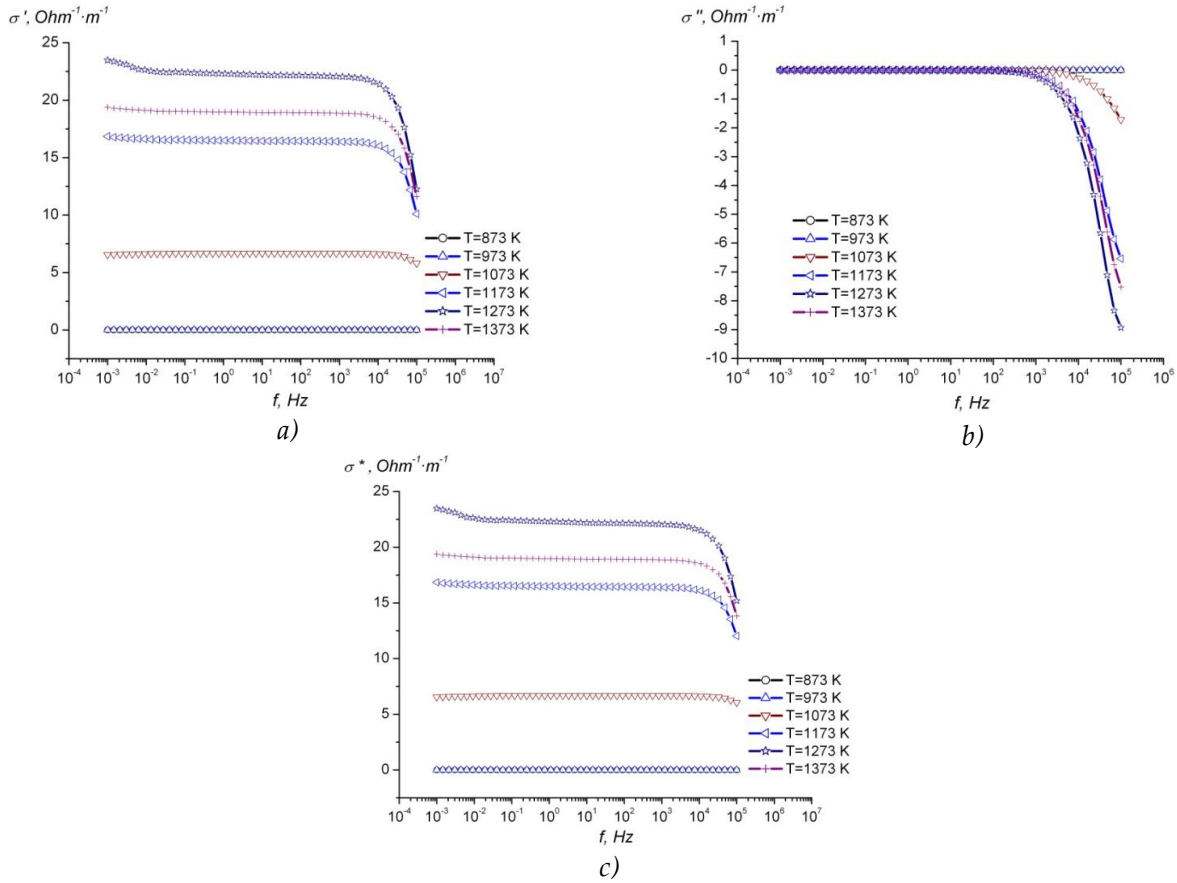

Fig. 4. The frequency dependences of real (a), imaginary (b) and complete (c) conductivities of PCMs obtained at different carbonization temperatures.

Interesting is the behavior of the conductivity in the frequency range 10^3-10^5 Hz. For PCMs, carbonized at a temperature below 1023 K, a sharp drop of conductivity with decreasing frequency is observed in this frequency range, whereas conductivity increases when frequency decreasing at $T > 1023$ K. This is because during carbonization is thermal decomposition of raw materials, at which a removing of volatile materials take places. Further increase in temperature leads to nucleation of graphite inclusions, which increases when heated and form ordered graphite layers.

The kind of raw materials and treatment conditions determine the size and number of graphene layers and relative orientation of crystallites. The size and orientation of crystallites are important because they determine the texture of the material and mechanisms of electrical conductivity [10]. It is believed that at 1023 K a change of PCM conductivity is observed caused by the above-mentioned reasons.

Submission of frequency dependence of conductivity in semi-logarithmic coordinates makes it possible to determine the value of the electrical conductivity of the material by extrapolating of frequency independent area of curve to its intersection with the σ^*-axis (when $f \to 0$ we have access to the direct current) (Fig. 5).

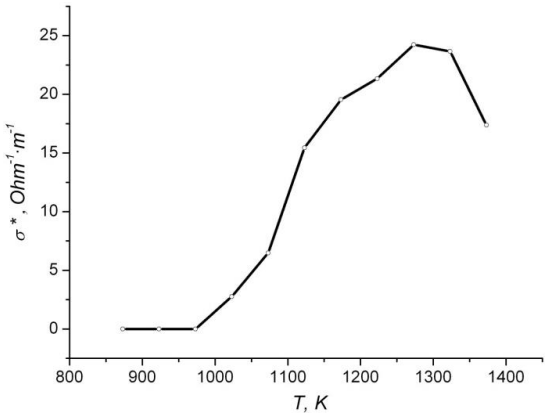

Fig. 5. The complete conductivity of PCMs as function of carbonization temperature.

As can be seen from this dependence, the increasing of carbonization temperature leads to a significant increase in conductivity compared to the temperatures $T \le 973$ K. Most probably, this is because at lower carbonization temperatures is a partial burning organic base of feedstock and incomplete formation of the complex frame from condensed aromatic layers formed by carbon atoms. As a result, the complete resistance of aggregate particles of PCM, which depends on a resistance of each particle and the contact resistance between them is quite high (the conductivity in this temperature range is between 0.31 ÷1250 μOhm^{-1}·m^{-1}). There is an increase in conductivity of PCM to the value of 24,23 Ohm^{-1}·m^{-1} (T = 1273 K) with increasing temperature, then there is a slight decline – its value is 17.38 Ohm^{-1}·m^{-1} at T = 1373 K.

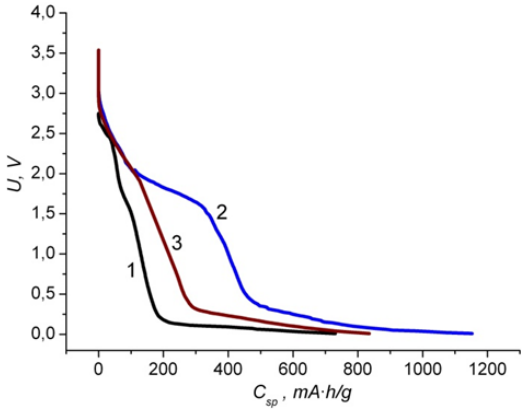

Fig. 6. Discharge curves of LPS based on PCM carbonized at 873 (1), 1073 (2), and 1373 K (3).

Electrochemical power sources were made on the bases of PCMs. As follows from the results of the experiment, the electrochemical process of lithium ions insertion into PCM has a stage character. There are 3-4 areas at discharge curves with different slope ratio (Fig. 6), at which speed the flow of electrochemical processes are different. For all material the main part of discharge capacity is provided at voltages less than 0.5 V. The wide horizontal plateau on the discharge curve answers this process. This behavior is typical for almost all carbon materials used in LPS [11-13]. The forming of insertion compounds as Li_xC takes place in this voltage range. Unlike natural (synthetic) graphite or highly ordered carbon materials for which this area is divided further into several horizontal plateau [14], for explored PCMs there is monotonically downward profile of this area of discharge curve. The latter is because the structure of the PCM is highly disordered and no clear boundaries of transition from one intercalation compound to another. Something different is character of discharge curves at voltages above 0.5 V. For PCMs, carbonized at temperatures of 1023-1173 K, can distinguish two areas in the voltage range of 2.8-1.6 V and 1.6-0.5 V (Fig. 6, curves 1 and 3); the first range can also be further divided into two ones (from 2.8 to 2 V and 2 to 1.6 V). For PCMs, carbonized at temperatures of 873-973 K and 1223-1373 K, such separation is difficult, because the first three intervals are merged into one, which corresponds to the voltage range 2.8-0.5 V. It is clear that such behavior is due morphological features of PCMs. In particular, PCM has a disordered structure and highly developed microporosity at low temperature carbonization (873-973 K), while at high temperatures (1223-1373 K) the surface area of the material decreases sharply, the process of material compacting and primary nucleation of graphite nanoclusters and layers take place. At carbonization temperatures of 1023-1173 K carbons are derived, which have properties of PCMs carbonized both at low and high temperatures. This feature provides the highest value of discharge capacity of these materials (Fig. 6, curve 2). As follows from the data (Tab. 2), the energy parameters of LPS depend on temperature carbonization non-monotonically. The greatest value of specific capacity has electrochemical system based on PCM, carbonized at 1023 K. However, due to higher discharge voltage the system based on PCM, carbonized at 1123 K, has a maximum specific energy. This behavior is caused mainly by the morphology of the material – specific surface, pore volume and PSD.

Carbonization temperature *T*, K	**C_{sp}, mA·h/g**	**E_{sp}, W·h/kg**
873	730	325
923	800	445
973	866	575
1023	1138	690
1073	1025	779
1123	984	977
1173	593	643
1223	571	500
1273	545	553
1323	877	754
1373	835	547

Tab. 2. Discharge parameters of LPS based on PCMs.

Comparing the results of low-temperature porometry (Tab. 1) with data of Tab. 2, it can be state that there is no clear correlation between the value of the discharge capacity and structural morphological parameters of PCMs. The cumulative impact of all these parameters creates preconditions for larger values of discharge parameters.

Determine what fraction of the total capacitance is a value of specific capacity of the initial stage of lithium ions insertion $\varepsilon_{in} = \frac{C_{in}}{C_{sp}} \cdot 100\%$ and on the plateau $\varepsilon_{pl} = \frac{C_{pl}}{C_{sp}} \cdot 100\%$, where C_{in} – capacity spent in voltage range of 2.8-0.5 V, C_{pl} – capacity spent at voltages less than 0.5 V (Tab. 3).

Carbonization temperature T, K	ε_{in}, %	ε_{pl}, %
873	0,39	0,61
923	0,37	0,63
973	0,30	0,70
1023	0,28	0,72
1073	0,45	0,55
1123	0,53	0,47
1173	0,54	0,46
1223	0,52	0,48
1273	0,55	0,45
1323	0,48	0,52
1373	0,34	0,66

Tab. 3. Capacity distribution in LPS based on PCMs.

The analysis made gives the possibility to establish that the C_{in} value satisfactorily correlated with the value of specific surface of PCM. This fact indicates that in this voltage range the basic electrochemical processes associated with the occurrence of reactions at the electrolyte/PCM boundary. A proof of this is the behavior of the discharge curve, i.e. a slope ratio that characterizes the rate of the electrochemical reaction. It is clear that due to the high mobility of ions in the electrolyte and absence of diffusion limitations fastest processes will occur exactly at the interface of two phases. Lithium ions inserted into PCM to be affected by the carbon matrix and electrostatic interactions with other lithium ions. Therefore, these processes will occur in time slowly, that meet nearly horizontal area at the discharge curve. Regarding the relation between ε_{in} value and other structural and morphological parameters, the precise relationship between them does not exist. There is no clear relation between these parameters and ε_{pl} value. It is logical to assume that the value of the specific capacity on the plateau should not depend on variables that describe the properties of the carbon material surface, since, as noted above, the passing of electrochemical processes in a voltage range below 0.5 V, is associated with the involvement of microcrystalline structure of PCM particles, but not their surface.

4. CONCLUSIONS

PCMs, which have developed porous structure, obtained in the temperature range 873-1373 K by the method of hydrothermal carbonization of raw plant materials. This structure is formed by both micro- and mesopores. The increasing of carbonization temperature leads to a reduction in both types of pores with a simultaneous increase in the part of mesopores (from 12 % at T = 873 K to 55 % at T = 1323 K) relative to the total pore volume.

The growth of carbonization temperature of feedstock in the range of 873-1373 K results in increasing of PCM conductivity in more than 6 orders. It value achieves maximum at 1273 K and is 24 $Ohm^{-1}\cdot m^{-1}$.

Specific energy parameters of LPS depend largely on the structure and morphology of PCMs. The maximum value of specific capacity (1138 mA·h/g) has electrochemical system based on a PCM obtained at 1023 K. For this carbon material the main part of the transferred charge (72 %) spent on the formation of Li_xC insertion compounds. It is set, that the process of lithium ions electrochemical insertion into PCMs has stage nature. The electrochemical processes related to the reactions on the material surface in the voltage range of 3.3-0.5; at voltages less than 0.5 V, is the formation of a continuous series of non-stoichiometric insertion compounds as Li_xC according to the reaction $xLi^+ + xe^- + C \rightarrow Li_xC$.

REFERENCES

[1] Kedrinskiy I.A., Dmitrienko B.E., Grudyanov I.I. *Lithium power sources.* Energoatomizdat, Moskow, 1992. (in Russian)

[2] Mandzyuk V.I., Kulyk Yu.O., Nagirna N.I., Yaremiy I.P. The Porous Carbon Materials Structure by X-ray Diffractometry and Small Angle X-ray Scattering Methods. *Physics and Chemistry of Solid State,* **13** (3) (2012), 616-624. (in Ukrainian)

[3] Mandzyuk V.I., Lisovskiy R.P., Nagirna N.I, Rachiy B.I. The structure of porous carbon materials according data of nitrogen adsorption/desorption. *Journal of Surface Physics and Engineering,* **11** (1) (2013), 112-121. (in Ukrainian)

[4] Mandzyuk V.I., Rachiy B.I., Lisovskiy R.P., Merena R.I. Electrochemical intercalation of lithium ions into nanoporous carbon material. *Physics and Chemistry of Solid State,* **10** (3) (2009), 647-659. (in Ukrainian)

[5] Brunauer S., Emmett P.H., Teller E. Adsorption of gases in multimolecular layers. *J. Amer. Chem. Soc.*, **60** (2) (1938), 309-319.

[6] Lozano-Castelló D., Suárez-Garsía F., Cazorla-Amorós D., Linares-Solano Á. *Porous texture of carbons.* In: Béguin F., Frackowiak E. (Eds.) Carbons for Electrochemical Energy Storage Systems. CRC Press - Taylor and Francis Group, Boca Raton-New York, 2002, 115-162.

[7] Neimark A.V., Ravikovitch P.I. Capillary condensation in MMS and pore structure characterization. *Micropor. Mesopor. Mater.*, **44/45 (**2001), 697-707.

[8] Abdullah M.H., Yusoff A.N. Complex impedance and dielectric properties of an Mg-Zn ferrite. *J. Alloys Comp.*, **233** (1996), 129-135.

[9] Gregg S.J., Sing K.S.W. *Adsorption, surface area and porosity*, *2nd ed*. London, Academic Press, 1982.

[10] Marsh H. *Introduction to carbon science*. Butterworth-Heinemann, 1989, 321.

[11] Novak P. *Carbon materials in lithium-ion batteries.* In: Novak P., Goers D., Spahr M.E. Carbons for electrochemical energy storage and conversion systems. Advanced materials and technologies series, CRC Press Taylor & Francis Group, 2010, 263-328.

[12] Noel M., Suryanarayanan V. Role of carbon host lattices in Li-ion intercalation/de-intercalation processes. *J. Power Sources*, **111** (2002), 193-209.

[13] Ogumi Z., M. Inaba. *Carbon anodes*. In: W. van Schalkwijk, B. Scrosati (Eds.) Advances in lithium-ion batteries. Kluwer Academic / Plenum publishers, 2002, 79-101.

[14] Ohzuku T., Iwakoshi Y., Sawai K. Formation of lithium-graphite intercalation compounds in nonaqueous electrolytes and their application as a negative electrode for a lithium ion (shuttlecock) cell. *J. Electrochem. Soc.*, **140** (9) (1993), 2490-2498.

Address: N.I. Nagirna, The Electronic Device College of IFNTUOG', 223 Vovchynetska Str., Ivano-Frankivsk, 76000, Ukraine;
V.I. Mandzyuk, Vasyl Stefanyk Precarpathian National University, 57, Shevchenko Str., Ivano-Frankivsk, 76018, Ukraine.

E-mail: n.nagirna@mail.ru; mandzyuk_vova@ukr.net.

Received: 04.02.2016; **revised:** 19.04.2016.

Нагірна Н.І., Мандзюк В.І. Морфологія, провідність та електрохімічні властивості гідротермально карбонізованих пористих вуглецевих матеріалів. *Журнал Прикарпатського університету імені Василя Стефаника*, **3** (1) 2016, 46–55.

У роботі досліджено морфологію, провідність та електрохімічні властивості вуглецевих матеріалів, отриманих із сировини рослинного походження за різних умов гідротермальної

карбонізації, з використанням методів низькотемпературної порометрії, імпедансної спектроскопії та гальваностаптичного заряду/розряду. Встановлено, що у пористій структурі вуглецевих матеріалів домінують мікропори; при збільшенні температури карбонізації питома поверхня та об'єм пор зменшуються більш ніж у 10 разів. Ріст температури також призводить до збільшення питомої електропровідності вуглецевого матеріалу більш ніж на 6 порядків. З'ясовано, що максимальним значенням питомої ємності (1138 мА·год/г) володіє електрохімічна система на основі пористого вуглецю, карбонізованого за температури 1023 K.

Ключові слова: пористий вуглецевий матеріал, морфологія, питома електропровідність, літієве джерело струму.

Journal of Vasyl Stefanyk Precarpathian National University
http://jpnu.pu.if.ua
Vol. 3, No. 1 (2016), 56-64

UDC 548.73/75+621.315.592
PACS numbers: 71.18+Y
doi: 10.15330/jpnu.3.1.56-64

THERMOCHEMICAL TRANSFORMATION IN THE PROCESS OF OBTAINING AND MODIFICATION OF NANOPOROUS CARBON

M.O. NYKOLIUK, B.I. RACHIY, I.M. BUDZULYAK, L.O. MOROZ

Abstract. The paper is devoted to the study of the thermochemical transformation in the process of obtaining and modification of nanoporous carbon. Nanoporous carbon material, which was gotten in carbonization process, is characterized by specific surface area. The thermogravimetric study of materials with linear heating and isothermal aging at a certain temperature were made to study the effect of thermal activation, which was conducted in air and argon atmospheres.

Keywords: nanoporous carbon material, heating, thermogravimetric study, weight loss.

1. INTRODUCTION

The unique ability of carbon atoms to form different valence states of hybridization of atomic orbitals creates conditions for the use of these materials in different areas of production. Nanoporous carbon materials (NVM) have a particular interest, which contain a mixture of nano-sized fragments of sp2 and sp3 - bonds, because these structures are of considerable scientific and practical interest as a material for creating extra large capacity in the capacitor systems and selective sorbents.

High requirements for properties of nanoporous carbon require systematic research on the influence of process parameters and subsequent receipt of chemical and thermal processing on its structure (size and pore volume, pore size distribution, specific surface area), when it is used as an electrode material of electrochemical capacitors (EC). Particularly important is the study of the characteristics of nanoporous carbon directly in the process of obtaining it from biomass (fruit seeds, coconut shell, flax fibers).

Natural raw materials are a composite chemical complex, which mainly consists of structurally bound water and less of non-structural compounds such as ash, protein, soluble sugars, starches, lipo and oils. The main structural compounds of dry plant material are cellulose, hemicellulose and lignin. Hemicellulose has a lower thermal stability than cellulose (Fig. 1), it is the first decomposed by heating biomass temperature range of 220-320°C, more thermostable cellulose starts to decompose around 320°C.

Cellulose and hemicellulose polysaccharides have different thermal stability due to differences in chemical structure. Cellulose is a natural linear polysaccharide, which is built from anhydride of D-glucopyranose, with a polymerization degree in the order of 10,000. Cellulose polymers are combined into crystalline, fibrous structures which ensure thermal stability. Hemicellulose is a branched hetero-

sacharide which consists of complex non-amyloid and non-cellulose polysaccharides. The degree of polymerization of hemicellulose is quite low, so it is amorphous.

2. Materials and Methods

Lignin is a irregular branched polymer with macromolecules, which are held by ethereal and C-C bonds. Lignin is characterized by a slow process of thermal decomposition, covering the temperature range from 160 to 900°C. Different content from chemicals leads to differences in the behavior of biomass in the process of carbonization. To study the carbonization plant material are used differential-thermal (DTA) and thermogravimetric (TG) analysis.

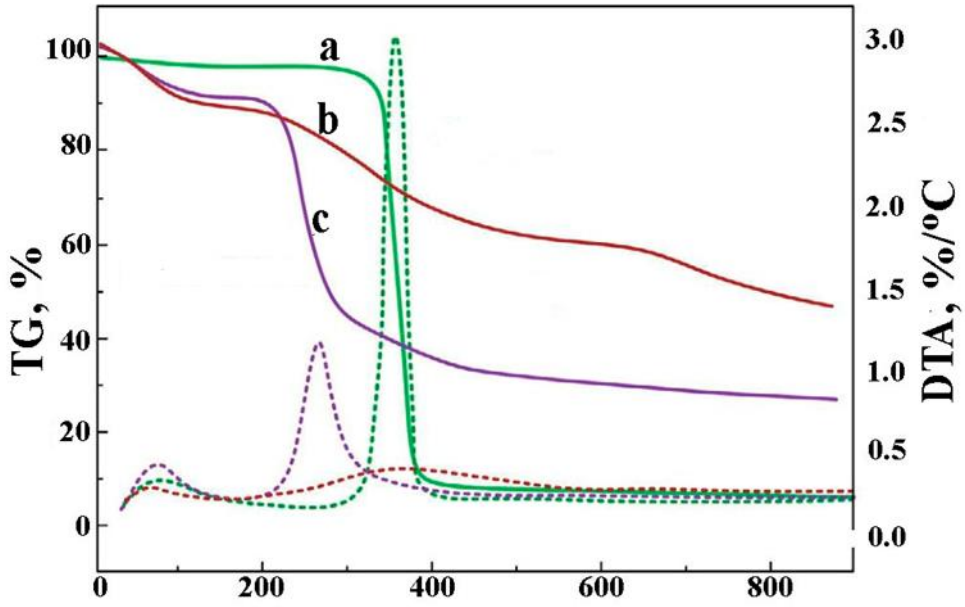

Fig. 1. Thermogram a) pulp, b) lignin in) hemicellulose. (- TG, ••• DTA) [1].

The study of chemical reactions and physical changes, that occur by heat in non-carbonated (ankle apricot, plum, cherry, coconut shell) and carbonated (coal from the pits of apricots, plums, coconut, cherry, fiber flax) materials, are conducted in derivatograph MOM Q-1500 D at a heating rate of 10 and 20 °C per min in air and the temperature range 20 - 900°C. The empty crucible of Al_2O_3 was used as a comparative standard. The sample was heated with a reference sample and recorded current temperature of the sample and the temperature difference between the sample and the standard. The change in mass of the samples presented by heating TG curve, the rate of change of weight - DTG, the change in enthalpy curve - DTA.

3. Results and Discussion

The analysis of the DTA and TG curves shows that carbonated materials (Figure 2) loss weight due the heating of the specified temperature range of 85-90% of the total mass of the sample (Table. 1). At relatively low temperatures (120-130°C) the reducing of mass of the samples to 10% can be explained by the release of the sorbed forms of water, which are contained in the material. This is evidenced by at least endothermic DTA curve at this temperature (Tab. 2; Fig. 2, curve DTA), that is an additional absorption of heat by evaporation of water. The next small horizontal plateau at temperatures of 170-210°C indicates the resistance of the materials in this temperature range and the absence of any significant chemical reactions that consists with Figure 1. The maximum reduction of weight (approximately 75-80%) (Tab. 1) feedstock occurs in the temperature range 250-900°C (Fig. 2, TG curve).

The heat is in the temperature range 220-500°C (Tab. 2; Fig. 2, curve DTA). As a result of decomposition of organic material and burning a large amount are released of organic volatiles (CO, CO_2) and volatile organic compounds. Simultaneously with this process another process is, that is accompanied by increased carbon content that processes at temperatures above 600°C in the material 85% from the total mass of the sample.

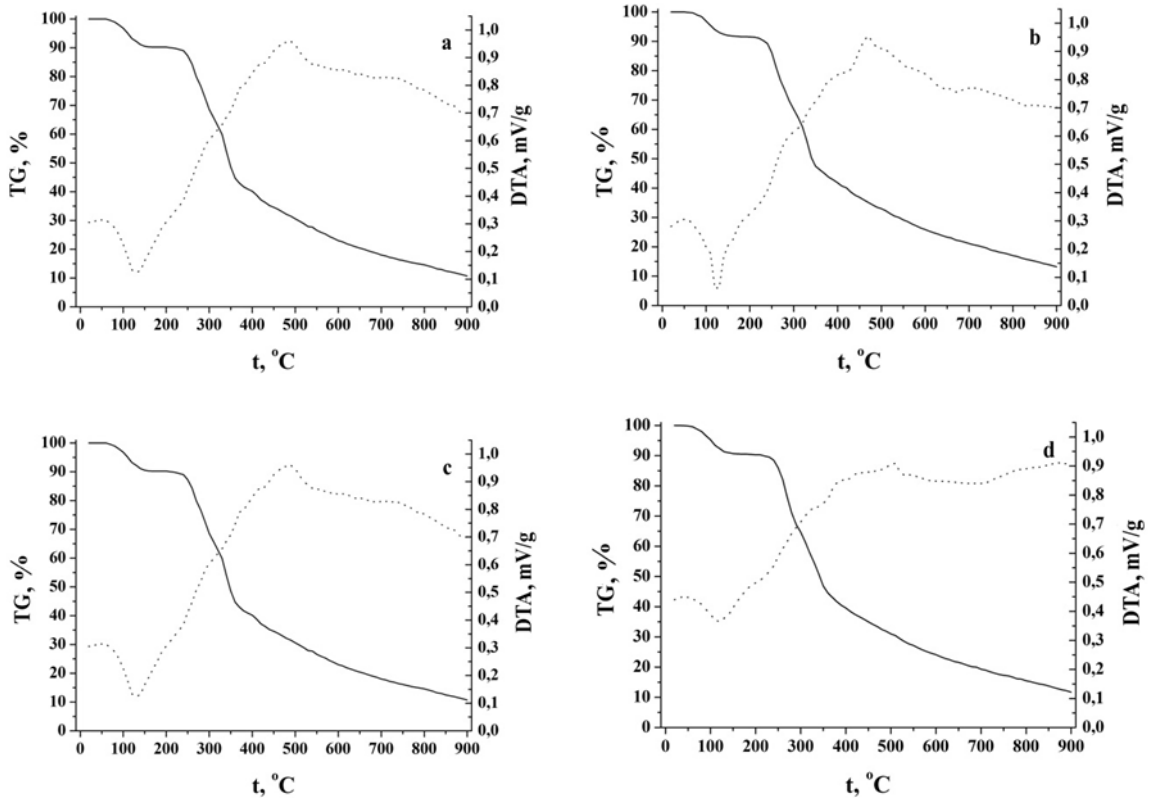

Fig.2. Thermography curves: a) apricot b) plums and) cherry and d) coconut shell. (--- TG, ●●●●● DTA).

The temperature range, ^{0}C	The loss of samples mass, %			
	Plum pits	Cherry pits	Apricot pits	Coconut shell
20-900	86	90	89	89
20-130	7,5	8,5	8,1	8,5
240-900	77	77,2	79,5	77,1

Tab. 1. The lose of weight for carbonated samples due to heat.

Sample	Non-carbonated samples			
	Plum pits	Cherry pits	Apricot pits	Coconut shell
Endothermic minimum, ^{0}C	120	125	130	120
Endothermic maximum, ^{0}C	470	475	480	485

Tab. 2. Temperature values of the endo-(exo)thermal effects for carbonated samples.

The final schedule of glucose residues occurs at temperatures above 500°C. In the temperature range 650-900°C, the process of polycondensation is with loss of oxygen, hydrogen, nitrogen and sulfur

is further carbonization material and carbon matrix transformation, namely the transformation of semicoal into structure of coal.

The carbon, which was gotten in carbonization process, is characterized by specific surface area of the maximum value of ≈ 400 m^2 /g [2]. The additional process of the carbonated carbon is required to increase the area and pore volume such as, for example, temperature or chemical activation. Air, water vapor, carbon dioxide, nitrogen oxide and sulfur dioxide can be used at the activation temperature as the oxidizing gases. The thermogravimetric study of materials with linear heating and isothermal aging at a certain temperature were made to study the effect of thermal activation in air and argon atmospheres conducted.

Data analysis TG and DTA, which are obtained for carbonated samples (coal apricot, plum, coconut, cherries), shows that the loss of mass due the heating in air atmosphere around the test temperature range is approximately 40-45% of the original mass (Fig. 3 curve TG), and the carbon was derived from waste flax weight loss due to heating is 57% (Fig. 4, curve TG), which is considerably less than in the case of carbonated material.

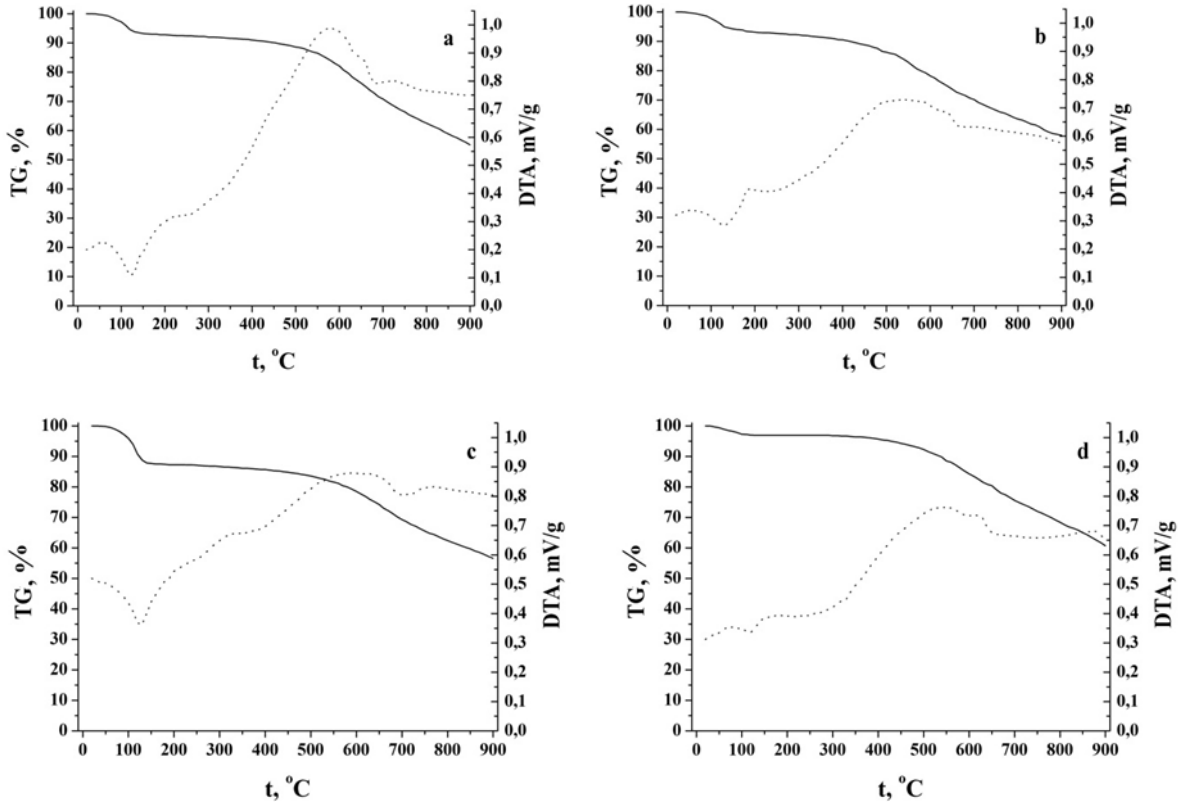

Fig. 3. The thermographs of the carbon that was obtained from: a) coconut shell; b) pitted plums, c) pitted cherries; d) apricot pits. (--- TG, ●●●●● DTA).

Obviously, in the case of carbonated material weight loss is possible mainly by burning carbon material as a result of the exothermic reaction $2C + O_2 \rightarrow 2CO$, as the part of bound water and other organic components of the source material were removed during carbonization.

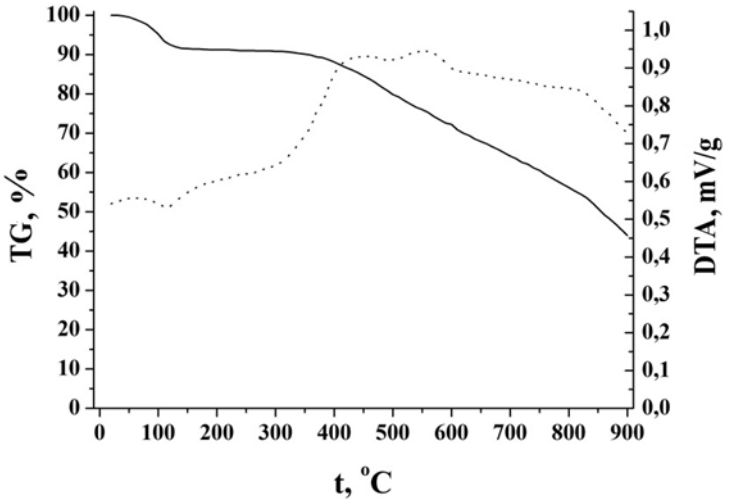

Fig. 4. The thermogram of the carbon that was obtained from flax fibers. (--- TG, ••••• DTA).

The obtained dependence for carbonated samples (coal apricot, plum, coconut, cherries) give reason to believe that at relatively low temperatures (120-130°C), the weight loss is only 5.7% (Tab. 3) by removing sorbed water forms. As feedstock at 120-130°C DTA curve reaches its minimum (Tab. 4; Fig. 3, curve DTA), which indicates endothermical process in this temperature range.

The temperature range, °C	**The lose of samples weight, %**			
	Carbon from plum	Carbon from cherry	Carbon from apricot	Carbon from coconut
20-900	43	43,7	42	45
20-130	5	5,5	5,8	6,5
450-900	32	33,7	34	34

Tab. 3. The lose of weight for carbonated samples due their heating.

Sample	Carbon from plum	Carbon from cherry	Carbon from apricot	Carbon from coconut
Endothermic minimum, ^{0}C	130	125	125	125
Endothermic maximum, ^{0}C	190, 560	560	550	220, 580

Tab.4. The temperature values of endo-(exo) thermal effects for carbonated samples.

Unlike raw materials of plant origin, the sharp weight reduction of carbonated material occurs at temperatures of 450-500°C (Fig. 3, curve TG) and is about 32-34% of the total weight (Table. 3), which is two times less than in the case of carbonated samples. In the temperature range 170-770 °C (Fig. 3, curve DTA) is the heat, which is obviously associated with the oxidation and subsequent outgassing of organic residues. Exothermic peaks are observed at 220°C and 580°C for coal from coconut and at 190°C and 560°C for coal from plums (Tab. 4) indicate the intensification of these processes.

The study of differences in the TG and DTA curves for coal, that was obtained at a pressure of 5-10 bar [2] and atmospheric pressure, shows that charcoal was derived from apricot pits, weight loss in the first case is 41%, while the second - 52%. The comparing of DTA curves (Fig. 3, g and Fig. 5, curve DTA) shows that charcoal was derived from the seeds of apricot at atmospheric pressure, there are two distinct maximum of exothermic effect at temperatures of 520°C and 640°C, which is likely due to the restructuring and stabilization system formed pores (Fig. 5, curve DTA). Also at 600-700°C, the process of annealing can be due to the passage of the exothermic reaction between carbon and oxygen.

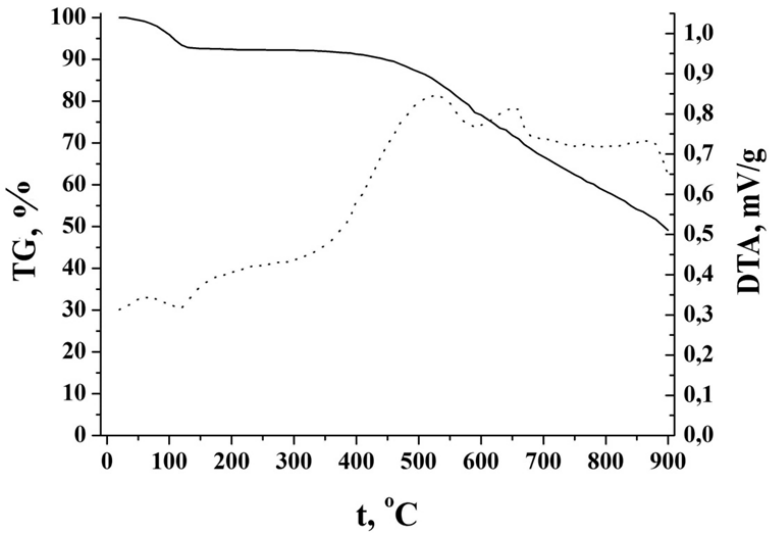

Fig. 5. The thermogram of carbon that derived from apricot pits at the atmosphere pressure (--- TG, DTA •••••).

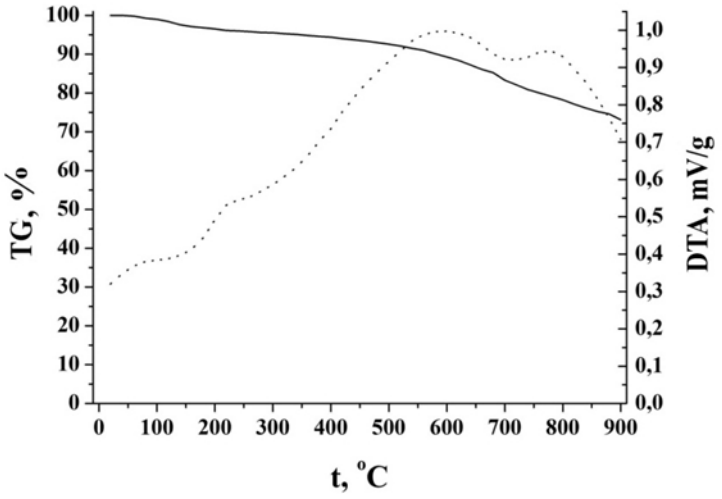

Fig. 6. The thermogram of carbon that obtained from coconut shell (heating rate 20 °C /min) (--- TG, DTA •••••).

It is known that the temperature endothermic process of beginning and end depends on the rate of heating of the sample, and with increasing heating rate the temperature range of the main stage of dehydration is shifted towards higher temperatures. In particular, the carbon of coconut at heating rate of 20°C/min the endothermic least, that is consistent the temperature of 125°C at a heating rate of 10°C/min, it is less pronounced and shifted towards more temperatures (~ 175°C) (Fig. 6, curve 2).

The study of carbonated carbon mass change at the isothermal aging in an argon atmosphere was performed on synchronous termoanalizator STA 449 F3 Jupiter (Fig. 7). Samples were kept at temperatures of 300, 400, 500, 600 and 700°C for 4 h. [3].

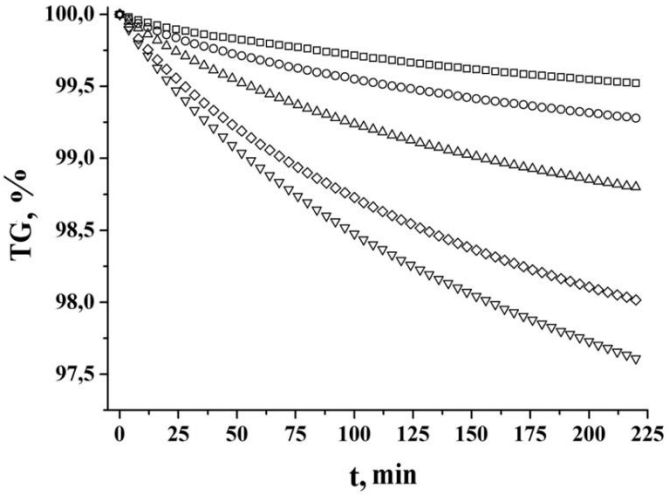

Fig. 7. TG curves of the carbonated carbon at isothermal aging at temperatures: □ - 300°C, ○ - 400°C - 500°C, ◊ - 600°C - 700°C.

For all samples on the DTA curves are no exo- and endothermic effects, this change of mass is not related to the release of reaction products with oxygen, and therefore the change in mass (Tab. 5) is most likely caused by the release of hydrogen atoms [4].

T, ºC	300	400	500	600	700
TG, %	0,5	0,7	1,3	1,9	2,4

Tab. 5. The changes of carbon mass at isothermal aging.

The important characteristics of the changes, which occurs in the structure of raw materials at the molecular level, there is evidence of the elemental composition of particular significance atomic ratio C/H and C/O. In addition, the surface of activated carbon is characterized by the type and number of oxygen functional groups. We know that intensive reduction of hydrogen [4], is based on changes in the atomic ratio C/H and observed at higher temperatures of 600°C, and C/O - up to 600°C. Removal of oxygen at higher temperatures is slowed, but complete removal of oxygen can not be achieved even at a temperature of 1500°C (1500°C when the content is 0.09% by weight of coal [4]). Dehydrogenatin from the nanoporous carbon at isothermal conditions is due to the fact that when exposed to high temperatures hydrocarbons are decayed the deep break ties C-C or C-H. It formed products, the composition of which depends on the thermal action (temperature, pressure, duration of heating) and the nature of the hydrocarbon. is The free radicals are the primary products of chemical reactions in the thermal decomposition of hydrocarbons, which then come into interaction with each other and with other molecules. The mechanism of this process is rather complicated. Chemical reactions in the thermal decomposition of hydrocarbons lead to cracks on the surface of the carbon particles. Exposure at 400°C does not lead to the destruction of the surface of the carbon material. The devastated areas can be seen clearly at 500°C, an increase in temperature to 100°C led to extensive changes in surface structure [3]. This indicates the existence of an optimal temperature activation process dehydrogenation reactions of these materials. Note that, because the changes in the structure of isothermal holding are followed by removal of hydrogen, it can not be taken his role in the degradation of the material due to the destruction of porous structure, which is crucial in electrochemical power sources. Another reason for the destruction of the surface at 500°C can be extensive selection of ash that is presented in the structure of the material. However, this assumption is not confirmed by the thermographic analysis because most likely responsible for destruction is the process of dehydrogenation.

4. CONCLUSIONS

Depending on the process for activated carbon and the kind of the original plant material, the weight loss and allocation processes or heat absorption are not significantly different. The maximum weight loss for carbonated samples are ≈ 80% of the total weight in the temperature range 250-900°C.

Maximum of DTA curves in the temperature range 180-770°C shows the heat, which is obviously associated with the oxidation and subsequent outgassing of organic residues and the minimum at 120-130°C can be explained by the removal of the sorbed forms of water that contained in the material.

Formation of pores in the studied material are possible through the pore-creator, that is introduced from outside (water vapor), bound water that is presented in the bulk material and by heating in an air atmosphere.

It is established that due to five-hour isothermal aging at temperatures of 300, 400, 500, 600 and 700°C nanoporous carbon is carbonated weight reduction due to its dehydrogenation. The main causes of this process are breaking the bonds C-C or C-N by free radical mechanism, which are accompanied by cracking the carbon matrix. It was found that the optimal temperature activation process of dehydrogenation reactions of these materials is in the range 500-600°C.

REFERENCES

[1] Yang H., Yan R., Chen H., Lee D.H., Zheng C. Characteristics of hemicellulose, cellulose and lignin pyrolysis. *Fuel*, **86** (2007), 1781–1788.

[2] Mandzyuk V.I., Lisovskiy R.P., Nagirna N.I., Rachiy B.I. The structure of the porous carbon material shall comply with the method of adsorption / desorption of nitrogen. *Physical Surface Engineering*, **11** (1) (2013), 112-121.

[3] Magomet O.D., Ostafiychuk B.K., Solovko Ya.T., Rachiy B.I., Budzulyak I.M., Yablon L.S. Dehydrogenation of Nanoporous Carbon in isothermal conditions. *Physics and Chemistry of Solid*, **11** (4) (2010), 864-867.

[4] Kyslytsyn A.N. *Pyrolysis of wood. Chemistry, kinetics, productivity, new processes.* Woods prod-ty, M., 1990, 312.

Address: M.O. Nykoliuk, B.I. Rachiy, I.M. Budzulyak, L.O. Moroz, Vasyl Stefanyk Precarpathian National University, 57, Shevchenko Str., Ivano- Frankivsk, 76018, Ukraine.
E-mail: marik.mbudoy@yandex.ua; bogdan_rachiy@ukr.net; ivan-budzulyak@ukr.net.
Received: 01.03.2016; **revised:** 25.04.2016.

Николюк М.О., Рачій Б.І., Будзуляк І.М., Мороз Л.О. Термохімічні перетворення в процесі одержання і модифікації нанопористого вуглецю. *Журнал Прикарпатського університету імені Василя Стефаника*, **3** (1) (2016), 56–64.

Робота присвячена вивченню термохімічних перетворень в процесі отримання і модифікації нанопористого вуглецю. Нанопористий вуглецевий матеріал, який отримали в процесі карбонізації, характеризується питомою площею поверхні. Термогравіметричні дослідження матеріалів з лінійним

нагріванням і ізотермічною витримкою при певній температурі були зроблені для вивчення впливу термічної активації, яка була проведена в повітряній і аргоновій атмосферах.

Ключові слова: нанопористий вуглецевий матеріал, нагрівання, термогравіметричні дослідження, втрата ваги.

Journal of Vasyl Stefanyk Precarpathian National University
http://jpnu.pu.if.ua
Vol. 3, No. 1 (2016), 65-70

UDC 621.315.592:535
PACS numbers: 05.05.70.Ce
doi: 10.15330/jpnu.3.1.65-70

THERMODYNAMICS OF THE POINT DEFECTS IN THE METALLIC PHASE OF THE SAMARIUM MONOSULPHIDE

I.V. GORICHOK, M.O. SHEVCHUK, V.M. BOYCHUK

Abstract. The equilibrial values of the vacancy concentration of chalcogen and antistructural samarium atoms in metallic phase of SmS were calculated by minimization the crystal thermodynamic potential. It was determined that the dominant defects are Sm_s^+ at the concentration of samarium 50,5-54 at. % and at the temperature of T=300-400 K. Also the concentration of negatively charged sulfur vacancies V_s^- is less on 1-2 points. The concentric dependence of samarium monosulphide density was explained using this offered model.

Keywords: samarium monosulphide, points defects.

1. INTRODUCTION

Samarium monosulphide is a promising material for using it in many branches of electronics that is conditioned by the complex of unique qualities [1-3]. In particular it concerns the huge tensoresistive effect, isomorphic phase transition of the I kind semiconductor-metal at the low pressure and also the appearance of electric power at steady warming of this sample under the condition of absent external temperature gradients [1-3].

The wide spectrum of properties is caused by the peculiarities of the material energetic structure and first of all by the presence of crystal of low energetic band formed by the metal atoms 4f-electrons at band gap [1, 2]. Point defects have a great influence on electrical properties of SmS whose concentration can reach to ~ 10^{21} cm^{-3} due to wide zone of compound homogeneity displaced to direction of the samarium surplus. Accordingly to the researches [3, 5, 8] in crystals with samarium surplus the dominant defects are antisite samarium SmS atoms that form shallow donor levels with ionization energy 0,045eV in crystal band gap. Also sulphur vacancies can be formed in samarium monosulphide [6], that are considered to be shallow acceptors accordingly to [7]. But their predominant zone or their quantitative correlation between the V_S and Sm_S concentrations are not expressly established.

The main aim of this work is determination of dependence species, charge state and concentration of dominant point defects on the degree of nonstoichiometry in the samarium monosulfide crystals.

2. METHOD OF CALCULATION

Concentrations of point defects in crystal at the temperature T can be determined by minimization of free energy F [8]. Taking into account the fact that all defects and samarium f-electrons are ionized in metallic phase and that the holes concentration is lesser than the concentration of electrons and point defects we can present the crystal thermodynamic potential as:

$$F = F_0 + \left(E_{V_S^-} + F_{vib,V_S^-}\right)[V_S^-] + \left(E_{Sm_S^+} + F_{vib,Sm_S^+}\right)[Sm_S^+] + (n_s + n_d)\mu - TS_{k,a} \quad (1)$$

where F_0 – free energy that is independent on defects, E – energy of point defects forming (vacancy or antisite atom); F_{vib} – free vibrational energy of defect; [D] – defect concentration; n_s, n_d – electron' concentration in s- and d-zone of conduction [9], $S_{k,a}$ – configuration entropy of anion sublattice.

Energies of single ionized donor and acceptor defects are determined according to the formula:

$$E_1 = E_0 - \varepsilon_1, \qquad E_1 = E_0 + \varepsilon_1, \quad (2)$$

E_0 – energy of neutral defect forming, E_1 – energy of formed defect ionization.

Change of the free vibrational energy of crystal at vacancy forming [10]:

$$F_{vib} = -\left\{3kT\ln\left(\frac{T_\theta}{T}\right) - kT\right\} + x \cdot 3kT\ln\left(\frac{\omega}{\omega_0}\right) \quad (3)$$

and at the forming of antisite defect:

$$F_{vib} = x \cdot 3kT\ln\left(\frac{\omega}{\omega_0}\right) \quad (4)$$

x – the amount of atoms that changed frequency of their vibrations from ω_0 to ω Entropy was determined using the Boltzmann law

$$S_{k,a} = k\ln(W_{k,a}) \quad (5)$$

where $W_{k,a}$ – thermodynamic probability:

$$W_{k,a} = \frac{N!}{(N-\sum[D])!\cdot\prod[D]!} \quad (6)$$

where N – concentration of sites in anionic sublattice.

Concentrations of electrons in s- and d- zone of conductions can be determined using the formula:

$$n_s = \left(\frac{2\pi m_s^* kT}{h^2}\right)^{\frac{3}{2}} a e^{b\frac{\mu}{kT}}, \qquad n_d = \left(\frac{2\pi m_d^* kT}{h^2}\right)^{\frac{3}{2}} a e^{b\frac{\mu-\Delta E_c}{kT}} \quad (7)$$

where the coefficients a and b – amendments that include degree of carrier degenerations and they are calculated by approximation of Fermi integral; μ - chemical potential of electrons, m_s^*, m_d^* – effective electron mass in s and d zones respectively; ΔE_c – distance between bottoms of s and d zones.

Chemical potential of electrons is determined from the equation of electroneutrality. Taking into account that density of the states in d-zone depends on the carrier concentration we can get:

$$Z_{V_S^-}[V_S^-] + Z_{Sm_S^+}[Sm_S^+] + N = N_{C,s} \cdot a\exp\left(b\frac{\mu}{kT}\right) + \left(N_{C,0}\right)^2\left(\frac{6}{10^5}\right)^6 \exp\left(-2b\frac{dE_c}{kT}\right) \cdot a^2\exp\left(2b\frac{\mu}{kT}\right) \quad (8)$$

Therefore

$$\mu = \frac{1}{b}kT\ln\left(\frac{-B+\sqrt{B^2+4A\cdot ZZ}}{2A}\right) \quad (9)$$

where:

$$A = \left(N_{C,0}\right)^2\left(\frac{6}{10^5}\right)^6\exp\left(-2b\frac{dE_c}{kT}\right) \cdot a^2$$

$$B = N_{C,s} \cdot a$$

$$ZZ = Z_{V_S^-}[V_S^-] + Z_{Sm_S^+}[Sm_S^+] + N$$

Electrons concentration in s-zone is lesser than in d-zone and that's why we get:

$$\mu \approx \frac{1}{b}kT\ln\left(\frac{\sqrt{A\cdot ZZ}}{A}\right) = \frac{1}{b}kT\ln\left(\sqrt{\frac{ZZ}{A}}\right) = \frac{1}{2}\frac{1}{b}kT\ln(\frac{ZZ}{A}) \quad (10)$$

Free energy of crystal is:

$$F = F_0 + \left(E_{V_S^-} + F_{vib,V_S^-}\right)[V_S^-] + \left(E_{Sm_S^+} + F_{vib,Sm_S^+}\right)[Sm_S^+] + ZZ\frac{1}{2b}kT\ln\left(\frac{ZZ}{A}\right)$$
$$-kT(N\ln N - [V_S^-]\ln[V_S^-] - [Sm_S^+]\ln[Sm_S^+] - (\mathrm{N} - [V_S^-] - [Sm_S^+])\ln(\mathrm{N} - [V_S^-] - [Sm_S^+])) \quad (11)$$

By minimizing (11) we get the equilibrial values of defects concentrations.

Thus it is important to include the condition:

$$[Sm_S^+] + [V_S^-] = X_{Sm} \quad (12)$$

When $Na \gg Sm_S^+ + V_S^-$ we get analytical expression for the determining of defects' concentrations. It's ne cessary for this to calculate the sulphur vacancy concentration from the condition (12) as a function of antisite defects concentration and to substitute it into (11). Differentiating (11) on the concentration of antisite defects and equating this expression to zero we can get:

$$[Sm_S^+] = \frac{X_{Sm}}{1 + \exp(\frac{(E_{Sm_S^+} + F_{vib,Sm_S^+}) - (E_{V_S^-} + F_{vib,V_S^-})}{kT} + \frac{Z_{Sm_S^+} - Z_{V_S^-}}{2b})(1 + \ln\left(\frac{N}{A}\right)))} \quad (13)$$

This formula is correct for rather narrow interval of defects concentration that's why we get the results in this investigation by the minimizing of the thermodynamical potential (11). The method of random disturbance was used for the searching function minimum (11) and the penalty function method was used to take into account the condition (12).

Energies of neutral defects forming according to (8) were accepted equal $E_0(Vs) = 10.69$ eV, $E_0(Sm_s) = 6{,}24$ eV. Antisite defect was considered to be shallow donor with energy of ionizing 0,045 eV [3], and sulphur vacancy as shallow acceptor with energy of ionizing $E_V + (\approx 0.1)\ eV$ [7]. The density was determined by the formula:

$$\rho = \frac{4}{a^2}M_{Sm} + [Sm_s^+](M_{Sm} - M_S) + \frac{4}{a^2}M_S - [V_s^-]M_S \quad (14)$$

3. Results and Discussion

As you can see on the picture (Fig. 1, a) with the growth of super stoichiometric samarium content concentration of sulphur vacancies and antisite samarium atoms is increasing. But concentration growth of the antisite samarium atoms is slower. Such character of correlation change between point defects determines non-linearity concentration dependence of samarium monosulphide density (Fig. 1, b): at the low content of surplus samarium the increase of density is caused by the increase of antisite defects concentration; and vacancy concentration does not significantly influence on this change; at the subsequent increase of Sm content concentration of sulphur vacancies becomes the same as concentration of antisite defects and the density increase of SmS is slowing.

In comparison with semiconducting phase of SmS, which defective subsystem is reported in [8], the concentration of sulphur vacancies V_S^- is rather higher in metal phase. Such effect can be explained that the chalcogen vacancies, forming vacant levels near the valence band top, are traps for the free electrons that go down from the bottom of the conductivity zone on the localized levels Vs, and predetermine increase according to the module of crystal free energy on the one level of the band gap width (area ~ 2,3 eV). Substantial increase of electrons concentration that takes place at isomorphic phase transition semiconductor-metal promotes the sulphur vacancies appearance because it causes to the considerable winning in complete crystal's energy.

It should be mentioned that the change of vibrations frequency of atoms near defects was accepted

as one in calculation. For the antisite defects Sm_s^+ as it is showed in [8], such supposition is correct but for sulphur vacancies – the situation is more complicated: exactness of the theoretical methods of calculating ω/ω_0 is insufficient for using calculated numerical values at the modeling, and experimental determination of this value has different difficulties. But as far as calculation curve ϱ (X_{Sm}) (Fig.1 b) satisfactorily describes experimental data it should be supposed that real value ω/ω_0 for sulphus vacancy is indeed close to one.

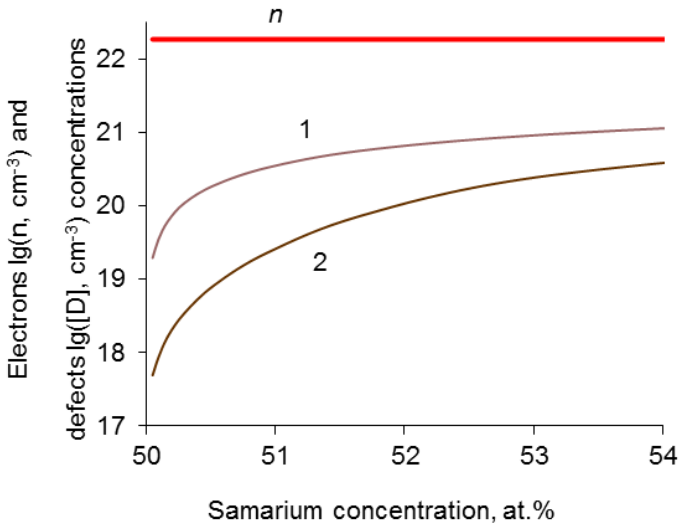

a)

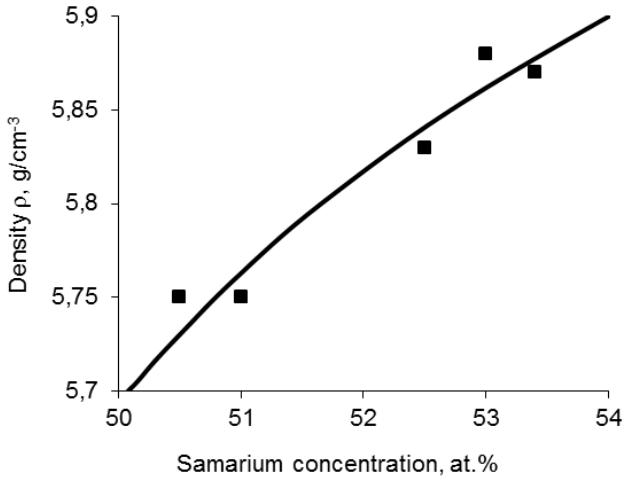

b)

Fig. 1. Dependences of the electron concentrations n, point defects (1–Sm_s^+, 2 – V_s^-) (a) and density ρ (b) on content of Sm in metal phase of samarium monosulphide.

4. CONCLUSIONS

1. Using the method based on the minimization of thermodynamical potential of crystal as function of defects concentration, dependences of the sulphur vacancies and antisite samarium atoms concentration in the area of homogeneity were calculated.

2. It was investigated that at the concentration of the superstoichometrical samarium 0,5–4.0 at% the predominant type of defects is antisite samarium atoms and the concentration of sulphur vacancy is on 1-2 points lower.

3. Non-lineal growth of the SmS density with the increase of samarium atoms amount in the range ~ 0,5 to 4,0 at% Sm was explained on the base of the obtained dependences of the point defect concentration on chemical composition of crystals.

ACKNOWLEDGMENT

This work according to scientific projects of the MES of Ukraine (registration number 0115U002303), and NATO diplomacy department publicly pursuant program we "Science for Peace" (NUKR, SEPP 984536).

REFERENCES

[1] Golubkov A.V., Goncharova E.V., Zhuse V.P., Loginov G.M., Sergeeva B.M., Smirnov I.A. *Physical quality of chalkogenids of the rare-earth elements.* Nauka, Leningrad, 1973. (In Russian)

[2] Ulashkevich Ju.V., Kaminskii V.V., Golubkov A.V. Specifics of infrared reflection spectrum of semiconductor Sm S in homogeneity region. *Jornal of Physics and Technics of semiconductors*, **43** (3) (2009), 324-328. (In Russian)

[3] Kaminskii V.V., Golubkov A.V., Vasiliev L.N. Defect samarium ions and generation effect of electromotive force in SmS. *Jornal of Physics of Solid State*, **44** (8) (2002), 1501-1505. (In Russian)

[4] Sergeeva V.M., Goncharova E.V., Kartenko N.F., Domina M.A., Smirnov I.A., Andriushin A.I., Misiuriev Ju.K. Research of SmS homogeneity region. *Jornal of Inorganic Materials*, **13** (12) (1972), 2114-2119. (In Russian)

[5] Kaminskii V.V., Vasiliev L.N. Concentration model of semiconductor – metal phase transition in SmS. *Jornal of Physics of Solid State*, **50** (4) (2008), 685-688. (In Russian)

[6] Kaminskii V.V., Sharenkova N.V., Vasyliev L.N., Soloviev S.M. Research of temperature dependence of SmS crystal structure parameter. *Jornal of Physics and Chemistry of Solid State*, **47** (2) (2005), 217-219. (In Ukrainian)

[7] Golubkov A.V., Goncharova E.V., Kapustin V.A., Romanova M.V., Smirnov I.A. Specification of the electrotransport model in the semiconductor phase of SmS. *Jornal of Physics of Solid State*, (12) (1980), 3561-3567. (In Russian)

[8] Shevchuk M.O. Thermodynamics of the point defects of the samarium monosulphide. *Jornal of Physics and Chemistry of Solid State*, **12** (4) (2011), 970–973. (In Ukrainian)

[9] Shadrichev E.V., Parfenieva L.S., Tamarchenko V.I., Griaznov V.I., Sergeeva V.M., Smirnov. I.A. Phenomena of transport and conductivity zone of the semiconductor phase of SmS. *Jornal of Physics of Solid State,* **18** (8) (1976), 2380-2385. (In Russian)

[10] Prokopiv V.V., Fochuk P.M., Gorichok I.V., Verzhak Ye.V. Description of defect formation processes in pure crystals of cadmium telluride through the thermodynamic potential method. *Jornal of Physics and Chemistry of Solid State,* **8** (2) (2007), 380-387. (In Ukrainian)

[11] Freik D.M., Gorichok I.V., Shevchuk M.O. Concentrantion dependence of electron effective mass in d-zone conductivity of samarium monosulphide. *Jornal of Physics and Chemistry of Solid State*, **13** (1) (2012), 27–30. (In Ukrainian)

Address: I.V. Gorichok, M.O. Shevchuk, V.M. Boychuk, Vasyl Stefanyk Precarpathian National University, 57, Shevchenko Str., Ivano – Frankivsk, 76018, Ukraine;

E-mail: HorichokIhor@gmail.com; rezervportal@gmail.com; volodymyra.boichuk@pu.if.ua.

Received: 01.03.2016; **revised:** 05.05.2016.

Горічок І.В., Шевчук М.О., Бойчук В.М. Термодинаміка точкових дефектів у металічній фазі моносульфіду самарію. *Журнал Прикарпатського університету імені Василя Стефаника*, **3** (1) (2016), 65–70.

Мінімізацією термодинамічного потенціалу кристала визначено рівноважні значення концентрацій вакансій сульфуру та антиструктурних атомів самарію у металічній фазі моносульфіду самарію SmS. Встановлено, що при вмісті атомів металу у сполуці 50,5-54 at. % за температур 300-400 K домінуючими дефектами є однократно позитивно іонізовані антиструктурні дефекти Sm_s^+, а концентрація негативно заряджених вакансій сульфуру V_s^- є на 1-2 порядки нижчою. На основі запропонованої моделі дефектної підсистеми пояснено монотонну залежність густини самарій моносульфіду від вмісту самарію.

Ключові слова: моносульфід самарію, точкові дефекти.

Journal of Vasyl Stefanyk Precarpathian National University
http://jpnu.pu.if.ua
Vol. 3, No. 1 (2016), 71-74

UDC 620.18:542.057:538,911
PACS numbers: 68.47.Gh, 64.70.Nd
doi: 10.15330/jpnu.3.1.71-74

THERMODYNAMIC PARAMETERS OF THE INTERCALATION REACTION IN THERMAL AND LASER MODIFIED NANODISPERSED ANATASE

M.YA. SEHIN, I.M. BUDZULYAK, O.V. MORUSHKO, L.S. YABLON

Abstract. It is modified matrix of anatase in turn of the thermal and laser treatments. The dependence of Gibbs energy change of the intercalation reaction of lithium with the guest load degree change was analyzed. Laser irradiation turned out to increase twice the value of maximum lithium "guest" loading, constricting heterophase area and changing contrarily concentration genesis of temperature dependence of entropy of lithium dilution. The optimal conditions of laser irradiation nanodispersive anatase (pulse energy E = 0,02 J, pulse duration τ = 15 ns repetition frequency f = 28 Hz, duration of exposure to 5 min.), at which specific energy characteristics of LPS, formed on its basis, increased by 55% is set.

Keywords: degree of intercalation, anatase, laser irradiation, specific capacitance.

1. INTRODUCTION

Transition metal oxides are promising electrode materials in advanced high-energy density batteries. The performance of an electrode depends on its ability to intercalate lithium reversibly into the host lattice. The transition metal oxides have open structures capable of accommodating guest ions and a flexible electronic structure which can accommodate donated electrons and provide sufficient ionic and electronic conductivity. One material which promises excellent properties for technological use as an electrode material in lithium batteries is anatase.

Nowadays, the problem of increasing power generation per unit mass and unit volume of a power source active substance is of paramount importance. The transition to nanosize of particles of cathode active material, which participate in Li+–intercalation current generating reaction, is one of the most effective methods to solve this problem [1, 2]. However, the problem of the possibility of ensuring essential increase of specific capacity in cathode process remains unsolved yet. Therefore, the aim of this work is an attempt to solve this problem.

2. EXPERIMENTAL SETUP

The solution of the set problem with taking into account the necessity of ensuring a high concentration of guest positions should be searched in the choice of such technique of modifications

which could enable us to control defects caused by growth (they can become additional guest positions as well) and impurity subsystem, with the necessary topology of energy levels in the gap.

Anatase was modified in vacuum 10^{-6} Pa at temperature 500 and 700°C during 1 h. Laser modification of nanodispersed anatase caused by action of laser irradiation (τ_i = 15 ns λ = 1.06 μm) with pulse energy 0.02, 0.03 and 0.04 J (duration of exposure to 5 min). For electrochemical investigations, electrodes with the area of 0.5 cm^2 on Ni substrate were formed. The electrode consisted of titanium dioxide powder, acetylene black as a conductive admixture and the binding agent, in the mass proportion of 85%: 10% : 5%. The mass of nanodispersed titanium dioxide did not exceed 3 mg. Thermodynamic electrochemical laws of lithium intercalation have been investigated in a three-electrode cell with one-mole solution of $LiBF_4$ in γ°-butyrolactone, a lithium electrode, and a lithium reference electrode.

3. EXPERIMENTAL RESULTS

The "guest" load degree and specific capacity is given in Table 1. In order to ascertain the degree of correlation between energy topology of impurity subsystem and the process of Li^+–intercalation current generation, thermodynamical investigations according to EMF technique [3] were carried out. The results of the analysis of the behavior of Gibbs' energy change ΔG(x) as function of the guest load degree for both materials are given in Fig. 1. It can be seen that the magnitude of the degree of guest load increases for modified anatase under discharge down to the voltage of 1.5 V, as compared to original anatase.

Temperature of thermal modification t,°C.	Pulse energy E, J	"Guest" load degree of Li^+	Specific capacity, A·h/kg
Original anatase	0	1,8	620
	0,02	2,7	887
	0,03	2,3	776
	0,04	1,5	492
500	0	2,9	971
	0,02	3,3	1115
	0,03	3,5	1182
	0,04	2,7	901
700	0	2,4	802
	0,02	4,4	1378
	0,03	3	998
	0,04	2,1	705

Tab. 1. The "guest" load degree and specific capacity of modified anatase.

The following equation can help to understand the process [4, 5]:

$$\Delta G(x) = eE(x) = \mu_i(x) - \mu_0, \quad (1)$$

where $\Delta G(x)$ is the change of the Gibbs energy of the reaction, e is the charge of electron, E is the electromotive force of the reaction, $\mu_i(x)$ is the chemical potential of the lithium insertion into the host structure, μ_0 is the chemical potential of lithium in the metallic lithium anode, x is the number of lithium atoms per unit of the host material according to the formula.

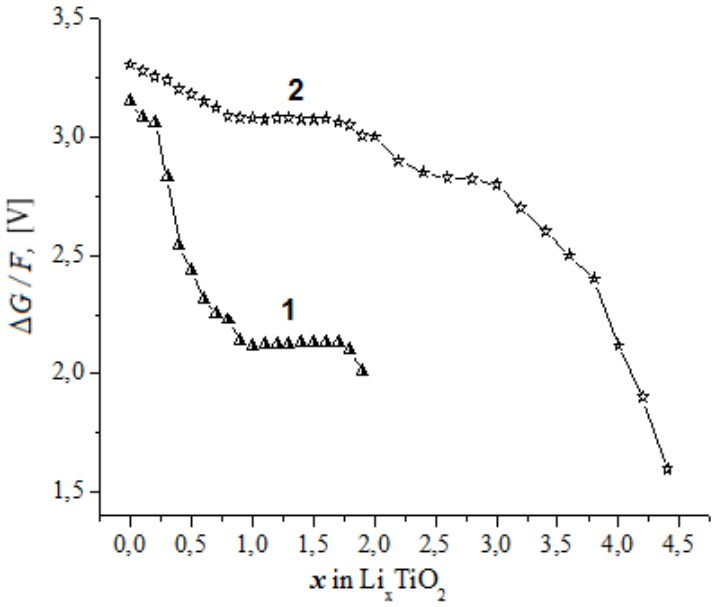

Fig. 1. Dependence of the Gibbs energy on guest load degree in original anatase (1) and modified anatase (2).

From the point of view of the thermodynamics of the Li+-intercalation current generation and according to Eq. (1), such transition means a change in the behaviour of $\mu_i(x)$. Its dependence on the degree of guest load x can be represented by the equation [6]:

$$\mu_i(x) = kT \ln\left|\frac{x}{1-x}\right| + N\omega x + [E_F(x) - E_F(0)] + L\frac{\partial c}{\partial x} + E_0. \qquad (2)$$

Here k is the Boltzmann constant, N is the number of the nearest neighbouring places, ω is the energy of interaction of inserted guest components, E_F is the position of the Fermi level, C is the distance between the layers, L is the coefficient which is determined by the Lennard–Jones potential function, E_0 is the bonding energy between intercalated atoms and matrix layers. It is evident that the change in $\mu_i(x)$ causes a change in the structure of the discharge curve.

4. CONCLUSIONS

Carried out investigations unambiguously indicate that the thermal and laser modification of structure of particles generating energy in Li^+-intercalation leads to pronounced increase in specific energy and power. However, just this modification does not ensure essential approaching of practically implemented specific capacity to the theoretically possible maximal value of corresponding cathode process. It ensures a magnitude at a level which does not exceed 1/3 of the theoretically possible one, relatively to the electrochemical equivalent of lithium. We have proved that the solution of the problem of further increase in specific capacity for nanodispersed anatase can be attained through forming structure defects; these defects form a certain energetic topology of electron states. And through this topology the defects formation ensures the needed dependence in the form of a function of lithium chemical potential of guest load degree.

According to the aforesaid approach, the physical mechanism of essential increase in energy and specific capacity consists in such a change of the energetic topology of a defects subsystem when:

- the density of states at Fermi level increases;
- deep levels in gap emerge.

REFERENCES

[1] Shao-Horn Y., Osmialowski S., Horn Q.C. Nano-FeS_2 for commercial Li / FeS_2 primary batteries. *J. Electrochem. Soc.*, **149** (11) (2002), A1499-A1502.

[2] Quintin M., Devos O., Delville M.H., Campet G. Study of the lithium insertion-deinsertion mechanism in nanocrystalline γ-Fe_2O_3 electrodes by means of electrochemical impedance spectroscopy. *Electrochimica Acta*, **51** (28) (2006), 6426-6434.

[3] Thompson A.G. Electrochemical studies of lithium intercalation in titanium and tantalum dichalcogenides. *Phys. B + C*, **99B** (1-4) (1980), 100-105.

[4] McKinnon W.R., Haering R.R. *Physical mechanisms of intercalation*. In: Modern Aspects of Electrochemistry, 15. New York, 1983, 235-261.

[5] Johnson D.A. *Some Thermodynamic Aspects of Inorganic Chemistry*, *2nd ed*. Cambridge University Press, Cambridge, 1982.

Address: M.Ya. Sehin, I.M. Budzulyak, O.V. Morushko, L.S. Yablon, Vasyl Stefanyk Precarpathian National University, 57, Shevchenko Str., Ivano- Frankivsk, 76018, Ukraine.
E-mail: ivan-budzulyak@ukr.net; yablon_lyubov@ukr.net; morushko@rambler.ru.
Received: 01.03.2016; **revised:** 28.04.2016.

Сегін М.Я., Будзуляк І.М., Морушко О.В., Яблонь Л.С. Термодинамічні параметри інтеркаляції в термічно та лазерно модифікований нанодисперсний анатаз. *Журнал Прикарпатського університету імені Василя Стефаника*, **3** (1) (2016), 71–74.

Проаналізовано залежність зміни енергії Гібса реакції від ступеня інтеркаляції іонів літію в модифікований термічним та лазерним відпалом анатаз. Лазерне опромінення викликає двократний ріст максимального гостьового навантаження іонів літію та зміни температурної залежності ентропії розчинення літію в матриці анатазу. Встановлено оптимальні умови лазерного опромінення (енергія імпульсу E = 0,02 Дж, тривалість імпульсу τ = 15 нс, частота f = 28 Гц, витримка 5 хв), при яких питома ємність літієвого джерела струму зростає на 55 %.

Ключові слова: ступінь інтеркаляції, анатаз, лазерне опромінення, питома ємність.

Journal of Vasyl Stefanyk Precarpathian National University
http://jpnu.pu.if.ua
Vol. 3, No. 1 (2016), 75-79

UDC 541.1, 5367, 621.794
PACS numbers: 52.70.La,61.05.cc,61.72.dd
doi: 10.15330/jpnu.3.1.75-79

NUMERICAL CALCULATION OF EXTINCTION COEFFICIENT FOR DISLOCATION LOOPS WITH A CERTAIN ORIENTATION

I.P. YAREMIY, U.O. TOMYN, S.I. YAREMIY, M.M. LUKANYUK, H.M. HODOVSKA,

YU.I. KATRYCH

Abstract. Approximation formulas for the calculation of extinction coefficients in a wide range of radii and concentrations of dislocation loops oriented in certain directions were obtained. It was shown that received expressions make it possible to quickly calculate with satisfactory accuracy the angular dependence of extinction coefficient and speed up the calculation of theoretical rocking curves.

Keywords: X-ray diffractometry, defects, extinction coefficient, dislocation loops.

1. INTRODUCTION

One of the methods of purposeful changing the properties of surface layers of materials used in electronic equipment is ion implantation. Ion implantation leads to the creation of point defects, which can associate into more complex defects, such as dislocation loops. These results in the formation of the crystal subsurface layer with a modified structure, characteristics of which depend on the distribution of stress fields, which parameters, in turn, are determined by shape, size, concentration of defects and in the case of dislocation loops, even their spatial orientation.

A common and express method to determine the numerical characteristics of radiation defects is the X-ray diffractometry. The reliability of the results is determined by the validity of the physical model of defects system used in estimating the angular distribution of intensity of X-rays diffracted by a real crystal with disturbed subsurface layer. In our studies, we used a statistical dynamical theory in the form of [1, 2], which makes it possible to take into account the types of defects and applicable to defects with any size. Nowadays for calculations of such structural sensitive to defects parameter as coefficient of absorption due to diffuse scattering μ_ds (extinction coefficient) correct in many instances assumption that dislocation loops can occur in all equivalent crystallographic planes with equal probability is used [3 - 5]. However, for example in the case of ion implantation, this assumption may be incorrect, and therefore a model in which dislocation loops are located only in certain crystallographic planes should be considered. Theoretical calculations in such cases are very

cumbersome and complex, so the aim of this article was to get the approximation formula for calculating the angular dependence of coefficient of absorption due to diffuse scattering.

2. Calculation of Coefficients in Approximation Formulas

In statistical dynamical theory of X-ray scattering coefficient of reflection from single crystals with uniformly distributed defects consists of coherent and diffuse components:

$$R(\Delta\theta) = R_{coh.}(\Delta\theta) + R_{diff.}(\Delta\theta)$$

Coherent component corresponds to the scattering by the "quasi-ideal" part of the single crystal, and diffuse component corresponds to the scattering by defects of various types. Existing in the crystal defects influence on the formation of both components. One of the parameters through which information about the characteristics of defects is included into the coherent and diffuse components of reflection coefficient of X-rays is the coefficient of absorption due to diffuse scattering $\mu_{ds}(\Delta\theta)$ [2]. It depends on such dislocation loops parameters as Burgers vector, radius and the concentration of dislocation loops.

For calculating the extinction coefficient taking into account the effects of anisotropy for each of them, just as in the work [2], the incident beam deviation from the exact Wolf-Bragg condition, the complex nature of momentum $\vec{q}$ transferred at diffuse scattering and different nature of the diffuse scattering in the Huang and Stokes-Wilson regions are taken into account. Values of coefficient $\mu_{ds}(\Delta\theta)$ for different reflections were calculated using mathematical package Maple 13, however, such calculations are very cumbersome, so the approximation was made and the approximation formula of the coefficient of absorption due to diffuse scattering was derived.

Materials with garnet structure are some of the common materials for which the ion implantation is used to modify their properties. Analysis of deformations that occur in the surface layers of the materials held by us in [6, 7], but taking into account the orientation of defects at X-ray analysis it was not implemented. In order to obtain the approximating functional dependence of the extinction coefficient on radius R and concentration c of dislocation loops and on the angular deviation of the incident beam from the exact Bragg position ($\Delta\theta$), analytical expressions obtained in [8] were used. Calculations were carried out for loops with Burgers vectors parallel to the [111] direction because the existence of such loops are the most likely in the investigated gadolinium gallium garnet (GGG) single crystals and ferrite-garnet films. As a result, arrays for a set of values of the angular deviation from the exact Bragg position ($\Delta\theta$) and radius R and concentration c of dislocation loops for (444), (888) and (880) reflections were received. Radius of dislocation loops ranged from 10 to 300 Å in increments of 2 Å, concentration ranged from $1\cdot10^{10}$ to $1\cdot10^{15}$ cm^{-3}.

Search of function that would satisfactorily approximate calculated data was carried out using Origin application. The approximation was implemented in an environment of written in C++ Builder program that used a combination of a number of approximation methods.

Dependence of the extinction coefficient on ($\Delta\theta$) for all values of R and c looked like two branches of exponential function – increasing and decreasing – that mirror reflected one another. The functional dependence for the descending branch at the relative strain $\Delta d/d = 0$:

$$\mu_{ds}(\Delta\theta, R, c) = y_0(R, c) + A(R, c)\left(e^{-\frac{\Delta\theta}{t_1(R,c)}} + e^{-\frac{\Delta\theta}{t_2(R,c)}}\right) \quad (1)$$

Dependencies at other values of relative strain can be found by shifting this function along angular variable.

The coefficients $A(R, c)$, and $y_0(R, c)$ were approximated by functions of the form:

$$A(R, c) = a_1(c)R^{b_1(c)}, \qquad y_0(R, c) = a_2(c)R^{b_2(c)};$$

coefficients $t_1(R, c)$ and $t_2(R, c)$ – by pseudo-Voigt:

$$t_{1,2} = \eta_{1,2}(R,c)\, G_{1,2}(R,c) + \left(1 - \eta_{1,2}(R,c)\right) L_{1,2}(R,c),$$

where:

$$L_{1,2}(R,c) = y_{01,2}(c) + \frac{2A_{1,2}(c)}{\pi} \frac{w_{1,2}(c)}{4(R - x_{c\,1,2}(c))^2 + w_{1,2}(c)^2},$$

$$G_{1,2}(R,c) = y_{01,2}(c) + \frac{A_{1,2}(c)}{w_{1,2}(c)} \sqrt{\frac{2\ln(4)}{\pi}}\, e^{-\frac{2(R - x_{c\,1,2}(c))^2 \ln 4}{w^2{}_{1,2}(c)}}.$$

	$A(R,c) = a_1(c) R^{b_1(c)}$					$y_0(R,c) = a_2(c) R^{b_2(c)}$				
	$a_1(c) = a_{11}c^2 + b_{11}c + d_{11}$			$b_1(c) = a_{12}c + b_{12}$		$a_2(c) = a_{21}c^2 + b_{21}c + d_{21}$			$b_2(c) = a_{22}c + b_{22}$	
	a_{11}	b_{11}	d_{11}	a_{12}	b_{12}	a_{21}	b_{21}	d_{21}	a_{22}	b_{22}
(444)	$-1\cdot10^{-4}$	$1\cdot10^{10}$	$2\cdot10^{21}$	$-1\cdot10^{-15}$	3,89	$-7\cdot10^{-13}$	201,94	$2\cdot10^{14}$	$-4\cdot10^{-16}$	2,84
(888)	$-9\cdot10^{-6}$	$3\cdot10^{8}$	$3\cdot10^{18}$	$-3\cdot10^{-15}$	3,51	0	$1\cdot10^{-4}$	$-1\cdot10^{8}$	$-5\cdot10^{-19}$	1,73
(880)	$-8\cdot10^{-5}$	$5\cdot10^{9}$	$1\cdot10^{21}$	$-2\cdot10^{-15}$	3,79	$-8\cdot10^{-12}$	960,75	$3\cdot10^{14}$	$-8\cdot10^{-16}$	2,97
	$t_1(R,c) = \eta_1(R,c) G_1(R,c) + \left(1 - \eta_1(R,c)\right) L_1(R,c)$									
	$A_1(c) = a_{31}c + b_{31}$		$w_1(c) = a_{32}c + b_{32}$		$\eta_1(c) = a_{33}c + b_{33}$	$y_{01}(c) = a_{34}c + b_{34}$			$x_{c1}(c) = a_{35}c + b_{35}$	
	a_{31}	b_{31}	a_{32}	b_{32}	a_{33}	b_{33}	a_{34}	b_{34}	a_{35}	b_{35}
(444)	$-5\cdot10^{-24}$	$1\cdot10^{-8}$	$-5\cdot10^{-22}$	$2\cdot10^{-6}$	$9\cdot10^{-26}$	$1\cdot10^{-6}$	$7\cdot10^{-19}$	$9\cdot10^{-4}$	$2\cdot10^{-22}$	$2\cdot10^{-7}$
(888)	$-5\cdot10^{-22}$	$7\cdot10^{-8}$	$-3\cdot10^{-21}$	$2\cdot10^{-6}$	$-9\cdot10^{-16}$	0,28	$3\cdot10^{-18}$	$3\cdot10^{-4}$	$5\cdot10^{-21}$	$-2\cdot10^{-6}$
(880)	$-4\cdot10^{24}$	$1\cdot10^{-8}$	$-3\cdot10^{22}$	$1\cdot10^{-6}$	$2\cdot10^{-24}$	$1\cdot10^{-6}$	$5\cdot10^{-19}$	$8\cdot10^{-4}$	$1\cdot10^{-22}$	$-1\cdot10^{-8}$
	$t_2(R,c) = \eta_2(R,c) G_2(R,c) + \left(1 - \eta_2(R,c)\right) L_2(R,c)$									
	$A_2(c) = a_{41}c + b_{41}$		$w_2(c) = a_{42}c + b_{42}$		$\eta_2(c) = a_{43}c + b_{43}$	$y_{02}(c) = a_{44}c + b_{44}$			$x_{c2}(c) = a_{45}c + b_{45}$	
	a_{41}	b_{41}	a_{42}	b_{42}	a_{43}	b_{43}	a_{44}	b_{44}	a_{45}	b_{45}
(444)	$-1\cdot10^{-25}$	$5\cdot10^{-10}$	$-2\cdot10^{-22}$	$2\cdot10^{-6}$	$4\cdot10^{-24}$	$1\cdot10^{-6}$	$2\cdot10^{-20}$	$9\cdot10^{-5}$	$5\cdot10^{-23}$	$3\cdot10^{-7}$
(888)	$-4\cdot10^{-23}$	$9\cdot10^{-9}$	$-9\cdot10^{-22}$	$1\cdot10^{-6}$	$-4\cdot10^{-16}$	0,78	$4\cdot10^{-20}$	$3\cdot10^{-5}$	$2\cdot10^{-21}$	$-2\cdot10^{-6}$
(880)	$-6\cdot10^{-26}$	$6\cdot10^{-10}$	$4\cdot10^{-24}$	$1\cdot10^{-6}$	$1\cdot10^{-23}$	$1\cdot10^{-6}$	$4\cdot10^{-21}$	$2\cdot10^{-4}$	$5\cdot10^{-23}$	$-8\cdot10^{8}$

Tab. 1 The coefficients of the approximating functions for (444) (888) and (880) reflections from GGG single crystals.

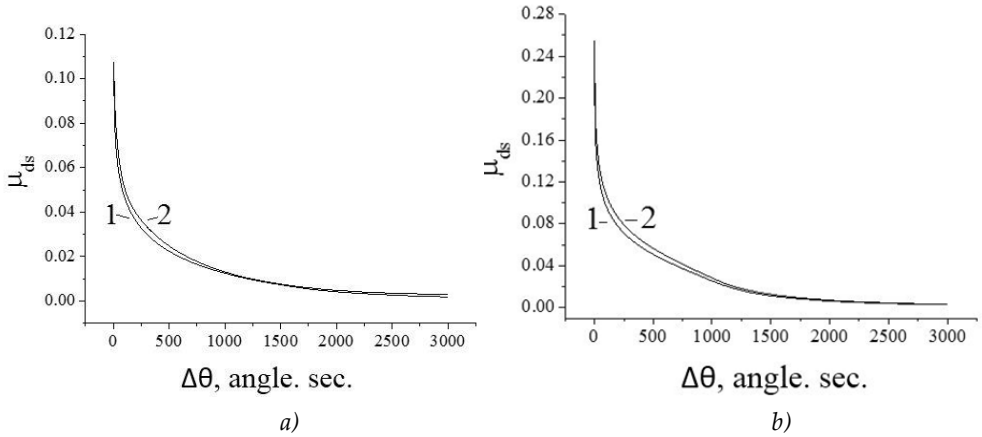

a) *b)*

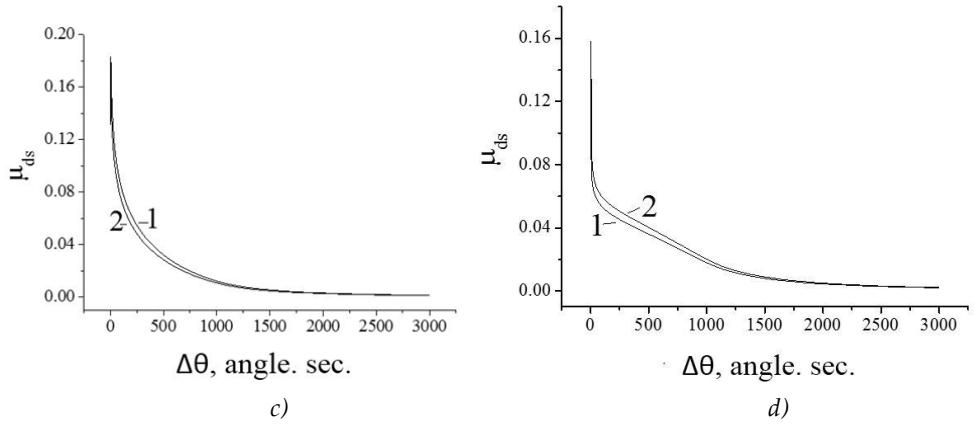

Fig. 1. Angular dependencies of $\mu_{ds}(\Delta\theta)$ for GGG single crystals in assumption of the presence of dislocation loops of radius R = 100 Å (1 – calculated by statistical dynamical theory considering anisotropy, 2 – calculated by approximation formula), a – reflection (444), b – reflection (888), c – reflection (880) (strongly absorbed wave fields), d – reflections (880) (weakly absorbed wave fields).

Dependence of the most coefficients of Pseudo-Voigt and exponential function on concentration is linear and others – parabolic. Analytical dependences of coefficients of approximation function on the radius and concentration of prismatic dislocation loops with Burgers vector parallel to the [111] direction, and the values of the numerical coefficients for reflections (444), (888) and (880) from the GGG single crystals are shown in the Table 1.

Approximation formula (1) gives a satisfactory approximation of the function $\mu_{ds}(\Delta\theta)$ at the concentrations ≤ $1 \cdot 10^{12}$ cm^{-3} (Fig. 1), but slightly worse – at large values of concentration. Obviously, this is related to the total error resulting from the multiple approximations.

3. CONCLUSION

Functional relationships were derived and coefficients by means of which it is possible to calculate the extinction coefficient μds, which takes into account the effects of anisotropy in the orientation of the dislocation loops in the crystal were calculated. Obtained approximation formula within the statistical dynamical theory enables to calculate with a satisfactory accuracy the theoretical rockin curves, which takes into account the effects of anisotropy in the orientation of dislocation loops.

REFERENCES

[1] Molodkin V. B., Olikhovskii S. I., Kislovskii E. N., et al. Bragg diffraction of X-rays by single crystals with large microdefects. I. Generalized dynamical theory. *Phys. Status Solidi B.,* **227** (2) (2001), 429-447. doi: 10.1002/1521-3951(200110)227:2<429::AID-PSSB429>3.0.CO;2-C

[2] Olikhovskii S. I., Molodkin V. B., Kislovskii E. N., et al. Phys. Bragg diffraction of X-rays by single crystals with large microdefects. II. Dynamical Diffuse Scattering Amplitude and Intensity. *Phys. Status Solidi B.*, **231** (1) (2002), 199-2012. doi: 10.1002/1521-3951(200205)231:1<199::AID-PSSB199>3.0.CO;2-Y

[3] Krivoglaz M. A. *X-Ray and Neutron Diffraction in Nonideal Crystals.* Springer, Berlin-Heidelberg, 1992. doi: 10.1007/978-3-642-74291-0

[4] Dederics P.H. Effect of defect clustering on anomalous x-ray transmission. *Physical review B*, **1** (4) (1970), 1306-1317.

[5] Molodkin V.B., Shpak A.P., et al. Multiparametric crystallography using the diversity of multiple scattering patterns for Bragg and diffuse waves. Method of standing diffuse waves. *Phys. Usp.*, **54** (7) (2011), 661-689. doi: 10.3367/UFNe.0181.201107a.0681

[6] Ostafiychuk B.K., Fedoriv V.D., Yaremiy I.P, et al. Implantation of single crystalline iron garnet thin films with He+, B+ and Si+ ions. *Physica Status Solidi A.*, **208** (9) (2011), 2108-2114. doi: 10.1002/pssa.201026749

[7] Ostafiychuk B.K., Yaremiy I.P., Yaremiy S.I., et al. Modification of the Crystal Structure of Gadolinium Gallium Garnet by Helium Ion Irradiation. *Crystallography Reports*, **58** (7) (2013), 1017-1022. doi: 10.1134/S1063774513070122

[8] Ostafiychuk B.K., Yaremiy I.P, Tomyn U.O. et al. The impact of implantation-induced defects on the structural, magnetic and morphological characteristics of the surface layers FHP subject to consideration of the effects of anisotropy. *Chernivtsi University Scientific Herald*. *Physics. Electronics*., **3** (1) (2013), 37-49.(in Ukrainian)

Address: I.P. Yaremiy, U.O. Tomyn, S.I. Yaremiy, M.M. Lukanyuk, H.M. Hodovska, Yu.I. Katrych, Vasyl Stefanyk Precarpathian National University, 57, Shevchenko Str., Ivano-Frankivsk, 76018, Ukraine.
E-mail: yaremiyip@pnu.edu.ua.
Received: 20.02.2016; **revised:** 19.04.2016.

Яремій І.П., Томин У.О., Яремій С.І., Луканюк М.М., Годовська Г.М., Катрич Ю.І. Чисельний розрахунок коефіцієнта екстинкції для дислокаційних петель з певною орієнтацією. *Журнал Прикарпатського університету імені Василя Стефаника*, **3** (1) (2016), 75–79.

Отримано апроксимаційні формули для розрахунку коефіцієнтів екстинкції у широкому діапазоні радіусів і концентрацій дислокаційних петель, при їх орієнтації в певних напрямках. Показано, що дані залежності із задовільною точністю дають можливість швидко розрахувати кутову залежність коефіцієнта екстинкції та пришвидшити розрахунок теоретичних кривих дифракційного відбивання.

Ключові слова: Х-променева дифрактометрія, дефекти, коефіцієнт екстинкції, дислокаційні петлі.

Journal of Vasyl Stefanyk Precarpathian National University
http://jpnu.pu.if.ua
Vol. 3, No. 1 (2016), 80-87

UDC 544.018/544.6.018.2/544.636
PACS numbers: 61.43.Gt, 81.07.Wx, 88.80.F, 82.47.Uv
doi: 10.15330/jpnu.3.1.80-85

THE INFLUENCE OF MODIFICATION OF THE SURFACE OF NANOPOROUS CARBON MATERIAL BY THE OXIDES OF METALS

B.I. RACHIY, M.M. KUZYSHYN, M.O. NYKOLIUK, R.I. MERENA, R.P. LISOVSKY

Abstract. Nitrogen containing carbon materials with metal of oxides (Fe, Ni, Co) prepared by the chemical precipitation method have been shown to be outstanding novel materials for electrochemical capacitors. The electrochemical properties of the electrodes have been studied by considering the effect of the mole ratio of metals. Cyclic voltammetric measurements indicate that nickel, cobalt and iron oxides increase specific capacity of electrochemical capacitors up to 260 F/g in 30% KOH electrolyte. Impedance studies show that the enhanced electrical properties and high frequency response are attributed to the presence of Fe oxides.

Keywords: electrochemical capacitor, pseudocapacitance, oxide of metal, nanoporous carbon material, surface modification.

1. INTRODUCTION

It is known that the energy storage in the electrochemical capacitors can be carried out by the electrostatic charge-discharge of the electric double layer realized in electrodes of the nanoporous carbon; or as the result of fast reversible faraday reactions which tend to occur when using oxides of ruthenium and iridium. However, the carbon materials with the large specific area of surface do not yield the high values of specific power and capacity. So promising is the combination of modification of the available electrode materials by heat treatment and chemical treatment with the implementation of metals and their oxides on the surface of the porous carbon to improve its electrochemical properties [1, 2].

2. MATERIALS AND METHODS

The combination of modifications by the heat treatment and chemical treatment with the introduction of oxides of metals on the surface of nanoporous carbon material (NCM) can increase the pseudocapacitance properties of the electrodes of electrochemical capacitors (EC). For this purpose, 3 g of N-containing NCM [3] is mixed with the aqueous metal nitrate 0.005 M and ammonia water 0.01 M. The mixture is moved for 3 hours at 333±5 K, then washed with distilled water to obtain a neutral pH. As a result of chemical reactions on the surface of NCM the metal hydroxides were formed. Prepared

material was dried at 353 K for 12 hours, then it was subjected to thermal treatment at T = 673±10 K in air for forming the metal oxides. As a result, there were received the samples of NCM with the metal content of 0.5; 1; 2 and 5 (in % of weight). Doped metals were iron, nickel and cobalt.

Electrochemical studies of behavior electrode materials in an aqueous electrolyte solution with the three-electrode cell. The basic composition for the working electrodes served mix included N-containing NCM precipitated with oxides of nickel, iron and cobalt and thermal expanded graphite. The resulting mixture was pressed into the nickel mesh with the size 5x5 mm^2. After the drying the shaped electrodes were soaked in an electrolyte solution. As subsidiary served platinum electrode and exemplary served chloride-silver electrode (Ag/AgCl), which is placed into the aqueous solution of KCl 3.5 M and combined with the working chamber via Agar-agar salt bridge. As the electrolyte was used the 33% aqueous KOH. Electrochemical studies are conducted using spectrometer Autolab PGSTAT100 with the cyclic voltammetry and chronopotentiometry, electrochemical impedance spectroscopy method in the frequency range of 10^{-2}...10^5 Hz and the following modulation of the equivalent electrical circuit (EEC). The calculation of parameters was made with the way of minimizing the standard deviation of measured impedance modulus and impedance modulus, automatically calculated for present EEC, using the installed software ZView-2 (Kramers-Kroning coefficient not more than 10^{-4}, difference between experimental and model curves is not more than 10%).

3. Results and Discussion

For the detailed analyze of physic-chemical processes on the border between the carbon electrode and electrolyte the Nyquist Plot were made (Fig. 1). All the impedance hodographs are the same far from the origin, that is modeled by frequency-independent resistance.

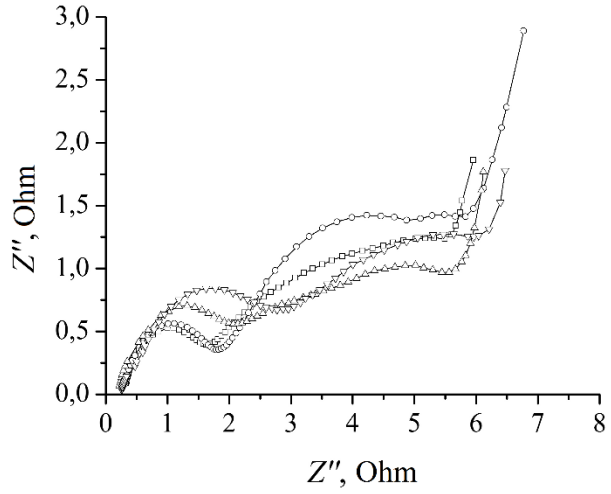

Fig. 1. Nyquist Plot for carbon electrodes with different consistence of iron: –□– 0,5; –○– 1; –Δ– 2 and – ∇ – 5 % of weight.

Impedance spectrum in the high frequency range is an arch which probably accords to a barrier created during transfer of the charge from the wire way to nanosponge carbon [4]. In the middle-frequency range there is an arch that indicates the pseudocapacitance accumulation of charge. The quick reversible Faraday reactions which are going together with the capacitance charge storage demands additional energy for chemical connections creation. In the low frequency range in all cases there is a linear part which has different angles and associated with the accumulation of the charge by the dual electric layer. The angle of the curve increases according to the iron content, that indicates the dominance of diffusion limitations over the kinetic ones.

Based on the arguments above to approach experimental curves (Fig. 1), that describe pseudocapacitance accumulation of the electric energy process, there is EEC on the Fig. 2.

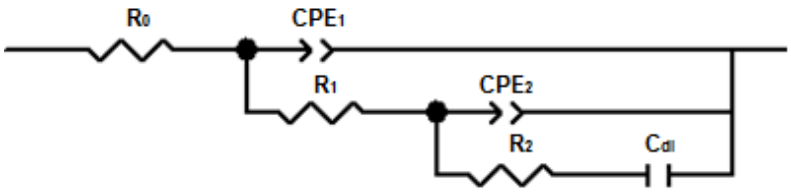

Fig. 2. EEC to make model Nyquist Plot, which we got for carbon electrodes doped with iron oxide.

At this scheme R_0 considers resistance of electrolyte, contacts and wire ways. The following elements indicate diffusion processes of the accumulation of electric charges in the sponges of carbon material on the border between electrode and electrolyte. So the link $CPE_1 \| R_1$ describes the forwarding of the charge through the border of electrolyte and electrode, which are caused by electrode material fractal structure. The link $CPE_2 \| R_2$-C_{dl} is responsible for diffusion processes that are caused by faraday reactions in transport ports and for kinetic processes of the double layer formation in micro ports, where R_1 and R_2 are the faraday resistance and polarize resistance, C_{dl} is the capacity of charge on the border (in this case it could be regarded as the capacity of double layer). This model of EEC gave us the possibility to approach the experimental spectrum to the calculated one and to get the parameters values for the scheme above (Tab. 1).

Sample	R_0, **Ohm**	CPE_1-T, **mF**	CPE_1-P	R_1, **Ohm**	CPE_2-T, **Ohm**	CPE_2-P	R_2, **Ohm**	C_{dl}, **F**
CFe-0.5	0.329	0.454	0.929	1.092	0.164	0.458	5.896	8.866
CFe-1	0.314	0.590	0.895	1.287	0.209	0.580	5.253	8.256
CFe-2	0.265	0.511	0.873	1.845	0.119	0.324	7.885	7.694
CFe-5	0.272	0.411	0.732	2.226	0.203	0.458	8.147	5.031

Tab. 1. EEC parameters in disconnected circuit potential.

In the model Nyquist Plots for EEC there were included elements of the constant phase *CPE*. Their impedance is determined with the formula: $Z_{CPE} = CPE_T(j\omega)^{-CPE_P}$, where the CPE_P parameter considers the phase deviation and, accordingly type modeled process. When the CPE_P value approaches to 1, this element defines the capacitance behavior of the system; but when CPE_P ~ 0,5 it defines diffusion behavior of the system. It should be noted, that the physical content of item CPE is not finally determined yet. In general it is considered as the result of the diffusion to uneven available surface, which formally attributed fractional dimension, or as accumulation of charge directly on this surface. In this case there is unevenly distributed capacitance, that is often associated with the surface roughness of the material [5].

Based on the above and data modeling analysis (Tab. 1) could argue that CPE_1 is the element of constant phase capacitive, which describes the spatially distributed capacitance carbon matrix ($CPE_1 - P$ approaches to 1). The volume of R_1 increases with increasing iron content and, the volume of $CPE_1 - P$ decreases from 0.9 to 0.7 with its increase. This fact is probably caused by decrease of active surface area, which is involved in the formation of double layer and by decrease in electrical conductivity of the carbon electrode. Significant changes characterize the CPE_2. According to table 1 it can be attributed as the steady phase diffusion type element. It is responsible for the diffusion of charge carriers, which is caused by quick reversible Faraday reactions.

Features and morphology of carbon electrodes which we have got are reflected in a kind of changes of EEC parameters during varying the electrode potential. For example for sample CFe-1 there are Nyquist Plots with different potentials of electrodes (Fig. 3).

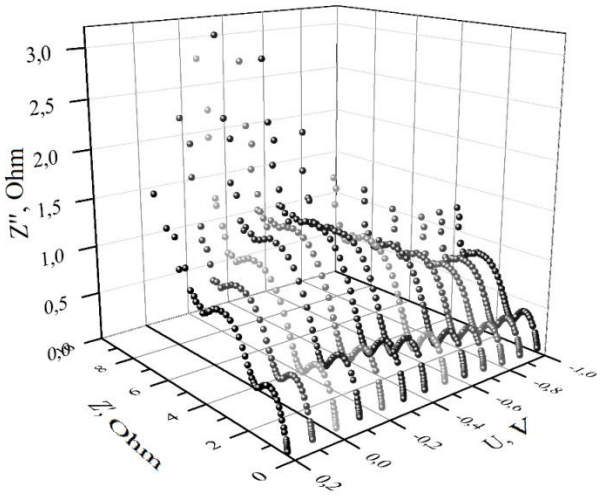

Fig. 3. Nyquist Plots with different potentials of electrodes for CFe-1.

Hodographs of impedance of electrodes have two well defined semicircle arches in ranges of high-frequency and middle-frequency, which can register under processes, accordingly, of transport of ions to the border of two phases and of pseudocapacitance accumulation of electric charge. After analysis of the data (Tab. 2) which we have got by modeling EEC (Fig. 2) it is possible to notice that resistances R_0 and R_1 are almost independent of the applied potential. The behavior of the element *C* is similar to changing of the electrode potential whereby its value increases sharply at potentials -0.4 V and -0.8 V. When the potential is -0.3 V is seen an increase in midrange arc, that is caused by faraday reaction: Fe_3O_4 goes into FeOOH [6]. With further growth of potential, as the result, carriers, which are formed in the charge trying to get the border of two phases. The same way when the potential is -0.7 V there is another reaction: FeOOH goes into FeO_2, and it caused the electrons released [6]. This in turn increases the electronegativity of the material, thus improving the availability of ions of K^+ to surface of the electrode. With the next potential growth the capacity reaches its maximum value.

So, potential dependence of parameters of EEC, which defines the behavior of the carbon electrode that is modified with the iron oxide depends on its content and on the area of the material which is involved to electrostatic accumulation of the electric power.

Fig. 4 demonstrates cyclic voltammogramms for the N-containing NCM with different content of iron (scan rate 1 mV/s), received by three-electrode cell regarding chlorine-silver comparing electrode.

***E*, V**	***R*₀, Ohm**	***CPE*₁-*T*, mF**	***CPE*₁-*P***	***R*₁, Ohm**	***CPE*₂-*T*, Ohm**	***CPE*₂-*P***	***R*₂, Ohm**	***C*dl, F**
0.2	0.302	2.608	0.859	1.057	0.215	0.462	5.848	11.570
0.1	0.305	1.794	0.856	1.229	0.173	0.534	5.194	5.612
0	0.309	1.072	0.875	1.331	0.149	0.572	5.367	4.723
-0.1	0.313	0.704	0.894	1.365	0.149	0.577	5.739	4.837
-0.2	0.314	0.598	0.896	1.375	0.160	0.583	5.828	5.611
-0.3	0.314	0.598	0.896	1.375	0.160	0.583	5.828	5.611
-0.4	0.314	0.590	0.895	1.287	0.209	0.580	5.253	8.256
-0.5	0.313	0.703	0.885	1.227	0.236	0.585	4.718	10.19
-0.6	0.313	0.881	0.878	1.160	0.266	0.593	4.208	11.30
-0.7	0.311	1.234	0.863	1.088	0.298	0.600	3.666	12.87
-0.8	0.308	1.933	0.846	1.017	0.329	0.607	3.112	13.22
-0.9	0.308	1.933	0.846	1.017	0.329	0.607	3.112	13.22
-1	0.308	1.933	0.846	1.017	0.329	0.607	3.112	13.22

Tab. 2. Parameters of EEC, which have been received by modeling of hodographs of impedance for the sample CFe-1 with different potentials of electrodes.

Getting cyclic voltammograms for carbon electrodes makes possible to calculate their specific capacitance relative to the chlorine-silver electrode compared by the formula: $C_{sp} = I/(2 \cdot s \cdot m)$, where I – is the current of anodic or cathodic branches in voltammogramms; s – is the scanning rate; m – the active weight of the electrode.

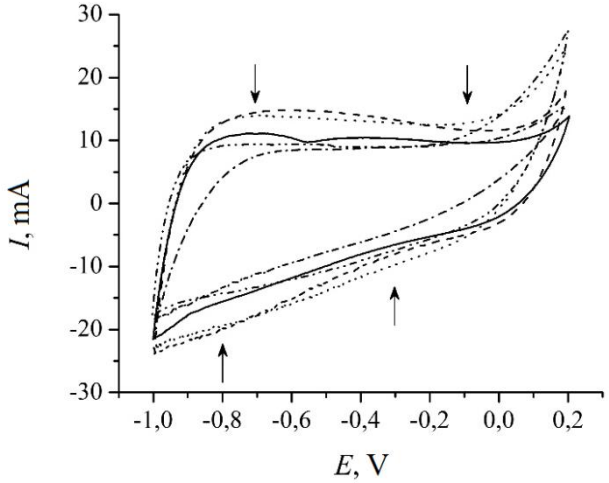

Fig. 4. Cyclic voltammogramms for the N-containing NCM with different content of iron (scan rate 1mV/s): ––– 0.5; - - - 1, -·-·- 2, ·····5 (in % of mass).

The calculated values of the specific capacity are shown in table 3. The cyclic voltammogramms are symmetric that evidence of reversible electrochemical behavior of existing cells. Additionally, the potential-dynamic curves demonstrate peaks, caused by the occurrence of the fast redox reactions.

Sample	Specific capacity, F/g		Effectiveness, %
	charging	discharging	
CKN-4	196.3	165.6	84.4
CFe-0,5	170.8	169.9	99.5
CFe-1	273.3	259.4	94.9
CFe-2	210.8	197.4	93.7
CFe-5	134.4	129.6	96.5

Tab. 3. Capacitance characteristics of iron-containing samples.

As shown in the (Tab. 3) with an increase in the percentage of iron, the capacity of the iron-modified NCM increases up to a maximum of 260 F/g with the iron content of 1%, that is caused by the combination of the capacity double layer on the border between carbon electrode and electrolyte with the pseudocapacitance, caused by iron oxide. Further increase of the share doped reduces the value of specific capacity by excess coating of surface of nanoporous carbon by the iron oxide. Thus, reducing the capacity of double layer is caused by the limiting of surface of NCM by iron oxide [2].

At fig. 4 for the sample CFe-0.5 it is possible to notice two anode peaks and two cathode peaks, which are caused by redox reactions. First Fe_3O_4 converts to FeOOH, then FeOOH goes to $FeO_2 \cdot FeOOH$ and FeO_2, which transform back to Fe_3O_4 and FeOOH accordingly [6]. As shown in the tab. 4, deposition of iron increases the capacity of nanoporous carbon electrode, and iron content of 1% provides the maximum specific capacity (260 F/g). It should be noted that with increasing of the iron oxide content, the intensity peaks at potentials -0.3 V and -0.7 V decrease. This shows the dominance of process of electrostatic accumulation of electrical energy.

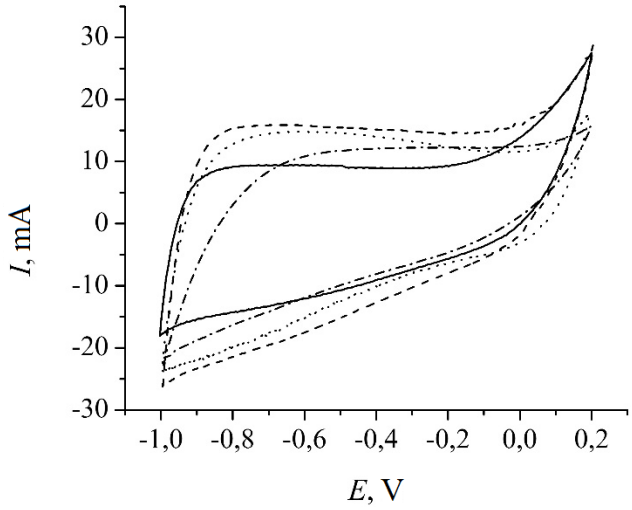

Fig. 5. Cyclic voltammogramms for metal-containing NCM: —— CNi-1; - - - CFe-1, ····· CCo-1, -·-·- NCM.

Based on the results of studies were received voltammogramms of samples with the deposited metals of nickel, iron and cobalt with the mass content of 1%, scanning speed was 1 mV/s (fig. 5). Find the peaks of redox reactions at voltammogramms of the samples with the oxide nickel and oxide cobalt is impossible, that is caused by large values of capacitance double layer [7].

Galvanostatic measuring of the cells, whose electrodes were formed based on NCM with the different oxides of metals showed almost symmetrical behavior of the charge/discharge processes (fig. 6). Slight deviations asymmetry of the curves of charge/discharge observed for the sample CFe-1, which showed the highest value of specific capacitance of 260 F/g.

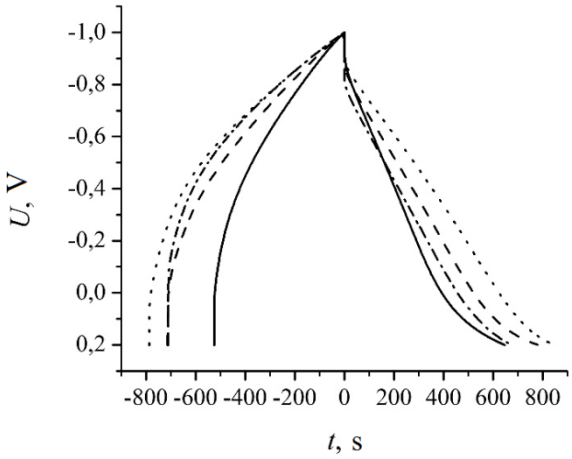

Fig. 6. Chronopotentiogramms for the samples —— CKN-4; - - - CNi-1, -·-·- CFe-1, ····· CCo-1.

The result is absolutely consistent with the data of the cyclic voltammetry (Tab. 3). It should be noted that such carbon electrodes exhibit greater capacitance value than N-containing NCM (Tab. 4).

Sample	**CKN-4**	**CCo-1**	**CFe-1**	**CNi-1**
C_{sp}, F/g	165.6	195.6	259.4	201.5

Tab. 4. Specific capacity of metal-containing NCM.

In addition, at the curves of charge/discharge of investigated materials it is possible to mark two areas with different slope: from -1 V to -0.3 V and from -0.3 V to 0.2 V (Fig. 6). According to [8, 9], some surfactants can promote the adsorption of anions or of cations or of both by the electrostatic forces and specific chemical absorption. In the first area dominates the process of electrostatic charge/discharge of

double layer; in the second area there is an influence of the quick reversible Faraday processes to the accumulation of the electric power.

4. CONCLUSIONS

Developed the method for the deposition of metal oxides on the surface of the nitrogenous NCM. Found that if the content of a metal is 1%, so nickel, cobalt and iron oxides increase specific capacity of EC up to 260 F/g with the current discharge 0.3 A/g.

The contribution of the pseudocapacitance to overall capacity of EC which include nitrogenous NCM makes 30%. The deposition of the oxides of nickel, cobalt and iron on the surface of the N-containing NCM further increase this contribution respectively by 18, 22 and 60%, that is caused by the occurrence of redox reactions on the surface of NCM with the participation of the surface functional groups, OH^- ions and metal oxides.

REFERENCES

[1] Lee Y.J., Jung J.C., Park S., Seo J.G., Baeck S.-H., Yoon J.R., Yi J., Song I.K. Preparation and characterization of metal-doped carbon aerogel for supercapacitor. *Current Applied Physics*, **10** (2010), 947-951.

[2] Lee Y.J., Park S., Seo J.G., Yoon J.R., Yi J., Song I.K. Nano-sized metal-doped carbon aerogel for pseudo-capacitive supercapacitor. *Current Applied Physics*, **11** (2011), 631-635.

[3] Ostafiychuk B.K., Budzulyak I.M., Rachiy B.I., Kuzyshyn M.M., Shyyko L.O. Nanoporous nitrogen-containing coal for electrodes of supercapacitors. *Nanoscience and nanotechnology research*, **1** (2) (2013), 17-22.

[4] Macdonald J.R., Cook G.B. Reply to comments by almond and west on Na β-alumina immittance data analysis. *Journal of Electroanalytical Chemistry and Interfacial Electrochemistry*, **193** (1-2) (1985), 57-74.

[5] Pajkossy T., Nyikos L. Diffusion to fractal surfaces – II. Verification of theory. *Electrochimica Acta*, **34** (2) (1989), 171-179.

[6] Liu X.M., Zhang Y.H., Zhang X.G., Fu S.H. Studies on Me/Al-layered double hydroxides (Me = Ni and Co) as electrode materials for electrochemical capacitors. *Electrochimica Acta*, **49** (19) (2004), 3137-3141.

[7] Lang J.W., Yan X.B., Liu W.W., Wang R.T., Xue Q.J. Influence of nitric acid modification of ordered mesoporous carbon materials on their capacitive performances in different aqueous electrolytes. *Journal of Power Sources*, **204** (2014), 220-229.

[8] Qu D. Studies of activated carbons used in double layer supercapacitors. *Journal of Power Sources*, **109** (2002), 403-411.

[9] Cottineau T., Toupin M., Delahaye T., Brousse T. Nanostructured transition metal oxides for aqueous hybrid electrochemical supercapacitors. *Applied Physics A*, **82** (2006), 599-606.

Address: B.I. Rachiy, M.O. Nykoliuk, R.P. Lisovsky, Vasyl Stefanyk Precarpathian National University, 57, Shevchenko Str., Ivano-Frankivsk, 76018, Ukraine;
M.M. Kuzyshyn, R.I. Merena, Ivano-Frankivsk National Medical University, 2, Halytska Str., Ivano-Frankivsk, 76018, Ukraine.

E-mail: bogdan_rachiy@ukr.net.

Received: 18.04.2016; **revised:** 20.05.2016.

Рачій Б.І., Кузишин М.М., Николюк М.О., Мерена Р.І., Лісовський Р.П. Вплив модифікації поверхні нанопористого вуглецевого матеріалу оксидами металів. *Журнал Прикарпатського університету імені Василя Стефаника*, **3** (1) (2016), 80–87.

Азотовмісні нанопористі вуглецеві матеріали з оксидами металів (Fe, Ni, Co), що осаджені хімічним методом є перспективним електродним матеріалом для електрохімічних конденсаторів. В залежності від вмісту металів вивчено електрохімічні властивості електродів. Методом циклічної вольтамперометрії встановлено, що осаджені оксиди нікелю, кобальту та заліза сприяють зростанню питомої ємності електрохімічних конденсаторів до 260 Ф/г у 30% водному розчині КОН. Імпедансні дослідження показують, що покращені електричні властивості і високий частотний відгук зумовлені наявністю оксиду заліза.

Ключові слова: електрохімічний конденсатор, псевдоємність, оксид металу, нанопористий вуглецевий матеріал, модифікація поверхні.

«Journal of Vasyl Stefanyk Precarpathian National University» is an academic periodical journal of Precarpathian National University, the main task of which is a publication of new original scientific matters, survey and problem articles in natural, mathematical, economic, medical, human and social sciences.

Every issue of journal refers to such series: "*Series of Natural and Mathematical Sciences*" and "*Series of Social and Human Sciences*".

Journal is issued since 2014 with regularity 4 issues per year.

Author Guidelines

The article should include: the title of the article, the authors and the main information about them (institutional name, email address and contact details), an abstract and keywords in English and Ukrainian languages. All articles are published in English only. The article submitted on the provided UDC, PACS numbers or 2010 Mathematics Subject Classification.

List of references is made as follows:

-BOOK (original in English)
[1] Author1 A.A., Author2 B.B., Author3 C.C. *Title of the book*. PublishingHouse, City, Year.

-BOOK as part of a series of publications (original in English)
[2] Author1 A.A., Author2 B.B., Author3 C.C. *Title of the book*. In: Editor1 A.A., Editor2 B.B. (Eds.) SeriesTitle, Number. PublishingHouse, City, Year.

-BOOK (original Ukrainian or Russian)
[3] Author1 A.A., Author2 B.B., Author3 C.C. *English translation of title of the book*. PublishingHouse, City, Year. (in Ukrainian) or (in Russian)

-ARTICLE (original English) (required indicate doi, if available)
[4] Author1 A.A., Author2 B.B., Author3 C.C. Title of the article. *Title of the Journal,* **Volume** (Number) (Year), PageF-PageL. doi:xxxxxxx

-ARTICLE (original Ukrainian or Russian) (required indicate doi, if available)
[5] Author1 A.A., Author2 B.B., Author3 C.C. English translation of title of the article. *Title of the Journal*, **Volume** (Number) (Year), PageF-PageL. doi: xxxxxxx (in Ukrainian) or (in Russian)

-CONFERENCE ABSTRACT
[6] Author1 A.A., Author2 B.B. Title of abstract. In: Editor1 A.A., Editor2 B.B. (Eds.) Proc. of the Intern. Conf. "Title of the Conference", City, Country, Month DateF-DateL, Year, PublishingHouse, City, Year, PageF-PageL.

The submission file should be in MS Word or TeX.

The text is single-spaced; uses a 10,5-point font Palatino Linotype; and all illustrations, figures, and tables are placed within the text at the appropriate points, rather than at the end.

SCIENTIFIC EDITION

Journal of Vasyl Stefanyk Precarpathian National University

Vol. 3, No. 1, 2016

Series of Natural and Mathematical Sciences

PHYSICS

Computer Editing, Layout and Design by **Svitlana Kliashtorna**
(*e-mail*: svimage@gmail.com)

«Terytoriya druku»,
128, Galytska Str., Ivano-Frankivsk, Ukraine.
Tel.: +38(0342) 58 04 32, *e-mail*: gsm1502@ukr.net.